Πανεπιστήμιο Κύπρου
University of Cyprus

Department of Civil and Environmental Engineering

UNDERSTANDING AND MODELLING OF MULTISCALE PHENOMENA IN THE URBAN ATMOSPHERE

PETROS MOUZOURIDES

A Dissertation Submitted to the University of Cyprus in Partial Fulfillment

of the Requirements for the Degree of Doctor of Philosophy

October, 2017

2017

APPROVAL PAGE

PETROS MOUZOURIDES

UNDERSTANDING AND MODELLING OF MULTISCALE PHENOMENA IN THE URBAN ATMOSPHERE

The present Doctorate Dissertation was submitted in partial fulfillment of the requirements for the Degree of Doctor of Philosophy in the Department of Civil and Environmental Engineering, and was approved on October, 2017 by the members of the Examination Committee.

Committee Chair _____
Prof. Panos Papanastasiou

Committee Member _____
Prof. Marie Farge

Committee Member _____
Prof. Georgios Georgiou

Committee Member _____
Assoc. Prof. Dimos Charmpis

Secondary Research Co-Advisor _____
Assoc. Prof. Andreas Kyprianou

Primary Research Advisor _____
Assoc. Prof. Marina Neophytou

DECLARATION OF DOCTORAL CANDIDATE

The present doctoral dissertation was submitted in partial fulfillment of the requirements for the degree of Doctor of Philosophy of the University of Cyprus. It is a product of original work of my own, unless otherwise mentioned through references, notes, or any other statements.

.....

.....

Abstract

The intense urbanization and the associated anthropogenic activities place numerous challenges to urban air quality modeling. However before we get to the point to predict the urban air quality, it is important to study and understand the physiochemical processes that occur in the urban atmosphere. The motivation of this thesis is to investigate the interactions between different atmospheric processes by addressing their multi-scale nature. Therefore, this thesis suggests novel methods in order to understand, provide insight and contribute in multi-scale modeling of multi-scale problems.

Specifically, Multi-Resolution Analysis (MRA), based on Discrete Wavelet Analysis, is proposed as a formal framework to represent two-dimensional (2D) urban morphology data (e.g building height, planar packing density) and building-related attributes (e.g. energy demands), for the derivation of associated boundary layer parametrization in atmospheric modeling. The objective of this study is to highlight the sensitivity of the various prognostic models (meteorological models, pollutant dispersion models) depending on how the morphological attributes of an area are configured, to propose a rigorous method of calculating and using these building-related attributes in various prognostic models at different study scales and to provide quantitative results that will help to the modeling of flow and dispersion field of different urban areas. The MRA results, confirm that the method is able to represent the morphological parameters of an urban area in a coherent way and has the ability to take into account the uniqueness of each area.

Besides the scale-adaptive and spatially-varying parametrization and representation of urban-related attributes, this thesis proposes the application of Wavelet Transform Modulus Maxima (WTMM), as a scheme of Continuous Wavelet Transform (CWT), in the analysis of long-term atmospheric measurements. Monitored meteorological and air-quality data were collected from a sub-urban station in the

form of time-series and they were analysed using WTMM analysis to gain insight into the multi-scale behavior of the sub-urban atmosphere. For a better understanding of the aforementioned times-series dataset a statistical analysis was conducted in order to investigate in more detail what lessons we can learn from monitoring measurements with regard to dispersion modeling of air pollutants as well as about the various related anthropogenic activities associated with them or to unveil a possible impact of phenomena occurring at larger scales (e.g dust events from Sahara Desert). The results of this study show that both the behavior of the atmosphere and the concentrations of pollutants are part of a multi-scale system. Therefore, the use of the multi-scale analysis through Wavelet Transform (WT) on the above-mentioned database, is necessary in order to extract quantitative results that will help to the modeling of flow and dispersion field. The derived scaling laws are determined by calculating the singularity spectrum $D(h)$, where a range of self-similar indices (h) measure the amount of repeating structures in their time-series. The analysis shows that the wind speed obeys the $-5/3$ law suggested by Kolmogorov only when the atmosphere lies within stable regime as defined by Monin-Obukhov theory. On the contrary under unstable regimes in the atmosphere, where the isotropy is perturbed, different laws are deduced. In addition, the results of the WTMM analysis suggest that the stability of the atmosphere plays a significant role in the behavior of the atmospheric flow and determines the observed scaling laws in the data.

Acknowledgments

First and foremost, I wish to express my sincere gratitude to my advisor Dr. Marina Neophytou and co-advisor Dr. Andrea Kyprianou for their guidance and their genuine concern and support for my progress in both my career and personal life. Their knowledge, patience, understanding and the interest for their student, set an example for me which I will do my best to follow.

Also, I would especially like to thank Dr. Prashant Kumar and his research group for their hospitality during my participation in Erasmus Exchange Program at the University of Surrey (UK). Under Dr Kumar's supervision I gained important experiences in both the research and the personal level. Also I would like to thank Dr. Ruchi Choudhary, Dr. Bertrand Carissimo, Dr. Michael J. Brown and their research groups for making valuable datasets available for the purposes of my PhD thesis. Moreover, special thanks go to Dr. Jason Ching, who believed right from the beginning in the merits and benefits of the Multi-Resolution Analysis for the meso-scale numerical modeling. I am grateful for his efforts to disseminate the method to the community of the atmospheric modeling. I'm also grateful to all the people who have helped or have inspired me through our scientific discussions during various conferences, schools, seminars and workshops.

Furthermore, I gratefully acknowledge all the staff of the Civil and Environmental Engineering Department of the University of Cyprus, both academic, technical and administrative for all their efforts to give me every possible support during my research activities.

Finally, I would like to dedicate this thesis to my family, and especially to my parents for their patience and their support all these years, in order to be able to complete my studies.

Short Biography

I received my undergraduate degree in Applied Mathematics and Physical Sciences from National Technical University of Athens in 2009. In 2010, I was enrolled in the postgraduate MSc Environmental Engineering program and since 2012 I have been transferred to the PhD program of Environmental Engineering of the Department of Civil and Environmental Engineering of the University of Cyprus (CEE-UCy).

Since 2010 I am a member of the Environmental Fluid Mechanics of CEE-UCy Laboratory. During Spring Semester 2014 I have been a visiting PhD student at the University of Surrey (UK) under an ERASMUS placement program. Currently I am a researcher at KIOS Research and Innovation Center of Excellence. I have attended a number of international workshops and conferences. I have initially served as a teaching assistant in Fluid Mechanics courses in the CEE Department and then as instructor of different Fluid Mechanics-related undergraduate courses. I am co-author of 4 journal papers, 7 conference papers and 3 more papers which are under review or submission.

Publications

Journal publications

1. P. Mouzourides, A. Kyprianou, R. Choudhary, J. Ching and M.K.-A. Neophytou, 2017. How can a Multi-scale Analysis Guide Smart Urban Energy Demand Management? An Example from London City Westminster Borough. Procedia Engineering, 180, pp.433-442.

2. P. Mouzourides, P. Kumar, and M. K.-A. Neophytou, "Assessment of long-term measurements of particulate matter and gaseous pollutants in South-East Mediterranean," Atmospheric Environment, vol. 107, pp. 148165, 2015.

3. P. Mouzourides, A. Kyprianou, M. J. Brown, B. Carissimo, R. Choudhary, and M. K.-A. Neophytou, "Searching for the distinctive signature of a city in atmospheric modelling: Could the Multi-Resolution Analysis (MRA) provide the DNA of a city?" Urban Climate, vol. 10, pp. 447475, 2014.

4. P. Mouzourides, A. Kyprianou, and M.K.A. Neophytou, "A scale-adaptive approach for spatially-varying urban morphology characterization in boundary layer parametrization using multi-resolution analysis," Boundary-layer meteorology, vol. 149, no. 3, pp. 455481, 2013.

Conference proceedings

1. P. Mouzourides, C. Marakkos, M.K.-A. Neophytou, "An experimental investigation of thermal circulation in urban street canyons", in Proceedings of International Workshop on Physical Modelling of flow and dispersion phenomena, Physmod 2017, Nantes, France, 23-25 August 2017.

2. P. Mouzourides, A. Kyprianou, R. Choudhary, J. Ching, M.K.-A. Neophytou, "How can a multiscale analysis guide smart urban energy demand management? An example from London City Westminster Borough", in Proceedings of International High Performance Built Environment Conference - A Sustainable Built Environment Conference 2016 Series (SBE16), iHBE, Sydney, Australia, 2016.

3. M.K.-A. Neophytou, P. Mouzourides, A. Kyprianou, R. Choudhary, J. Ching, "Sensitivity of mesoscale models to scale dependent UCP inputs: an example from urban energy demand" in Proceedings of 9^{th} International Conference on Urban Climate (ICUC9), Toulouse, France, 2015.

4. P. Mouzourides, A. Kyprianou, M. Brown, M.K.-A. Neophytou, "Exploring scale-adaptive representations and distinctive signatures of cities using the Multi-Resolution Analysis", Joint 11^{th} Symposium on the Urban Environment & Application of Air Pollution Meteorology, 94^{th} AMS Conference, Atlanta (GA), USA, 2014.

5. P. Mouzourides, A. Kyprianou, M.K.-A. Neophytou, "Multi-scale analysis for air quality data" in Proceedings of European Turbulence Conference, Lyon, France, 2013.

6. P. Mouzourides, A. Kyprianou, and M. Neophytou, Searching for the distinctive signature of a city: could the MRA be the DNA of a city, in Proceedings of the 8^{th} International Conference on Urban Climate, pp. 610, Dublin, Ireland, 2012.

7. P. Mouzourides, A. Kyprianou, and M. Neophytou, Wavelets and Multiscale analysis for urban air quality data: new insights, in Proceedings of the 7^{th} International Conference on Air Quality. Athens, Greece, 2012.

Under Review

1. P. Mouzourides, A. Kyprianou, R. Choudhary, J. Ching, M.K.-A. Neophytou, " Multi-scale analysis of urban building energy demands for smart energy management". (Energy Journal, Elsevier)

2. J. Ching, G. Mills, L. See, B. Bechtel, J. Feddema, I. Stewart, A. Hanna, X. Wang, E. Ng, C. Ren, O. Brousse, A. Martilli, M. Neophytou, G. Milcinski, M. Foley, P. Alexander, J. Hidalgo, V. Masson, D. Aliaga, M. Andrade, A. Sreevestava, A. Baklanov, P. Mouzourides, P. Bhalachandran, J. Dai,W. Dai, K. Hammerberg, D. Niyogi, "World Urban Database and Access Portal Tools (WUDAPT), an urban weather, climate and environmental modelling infrastructure for the Anthropocene". (Bulletin of the American Meteorological Society, AMS)

Under Submission

1. P. Mouzourides, A. Kyprianou, M.K.-A. Neophytou, "Exploring the multifractal behavior of the fluid dynamics and dispersion in a turbulent atmosphere" (to be submitted to Chaos: An Interdisciplinary Journal of Nonlinear Science, AIP).

Contents

List of Figures

List of Tables

Nomenclature

Acronyms

1*D*	One Dimensional
2*D*	Two Dimensional
3*D*	Three Dimensional
ADF	Augmented Dicky-Fuller test
AQMS	Air Quality Monitoring Station
AT	Ambient Temperature
BP	Barometric pressure
CWT	Continuous Wavelet Transform
DD	Diagonal Details
DoG	Derivatives of Gaussian function
FT	Fourier Transform
GUI	Graphical User Interface
HD	Horizontal Details
KPSS	Kwiatkowski-Phillips-Schmidt-Shin test
MCR	MATLAB Compiler Runtime
$Mf - DFA$	Multi-fractal Detrended Fluctuation Analysis
MRA	Multi-Resolution Analysis
NE	North East
NW	North West
$OKC - CBD$	Oklahoma City central business district
OWT	Orthogonal Wavelet Transform
RF	Rain fall
RH	Relative humidity
SE	South East

SR	Solar radiation
STFT	Short-Time Fourier Transform
SW	South West
TD	Total Details
TEOM	Tapered Element Oscillating Microbalance
TKE	Turbulent Kinetic Energy
UCP	Urban Canopy Parameters
UCY	University of Cyprus
VD	Vertical Details
WD	Wind direction
WS	Wind speed
WT	Wavelet Transform
WTMM	Wavelet Transform Modulus Maxima
WUDAPT	World Urban Database and Access Portal Tools
VOC	Volatile Organic Compounds

Symbols

β	Decay law of Power spectrum
$\delta(t)$	Dirac impulse or delta function
$\epsilon(t)$	Approximation error
κ	von Karman constant
λ_f	Frontal packing density
λ_p	Planar packing density
ν	Kinematic viscosity
ϕ	Scaling function
ψ	Mother wavelet function
σ	Standard deviation of building height
τ	Sampling period
$\tau(q)$	Scaling exponent spectrum

$\varepsilon(x)$	Energy dissipation rate
$\bar{H}$	Mean building height
$\bar{H}_{AW}$	Area weighted mean building height
$\langle f, \phi \rangle$	Inner product
$\mathbb{R}$	Set of Real numbers
A_T	Total planar area
CO	Carbon monoxide
$D(h)$	Singularity spectrum
d	Zero-plane displacement
f	Function
h	Hurst exponent or singularity index
H_a	Atmospheric Boundary Layer height
L	Characteristic size of large scale of turbulence
l_k	Characteristic size of small scale of turbulence - Kolmogorov length scale
L_{MO}	Monin-Obukhov length
NO	Nitrogen Monoxide
NO_2	Nitrogen Dioxide
NO_x	Nitrogen Oxides
$p(t)$	Polynomial expansion of function $f(t)$
PM_{10}	Particulate matter with diameter of 10 μm or less
q	Exponential parameter of WTMM
Re	Reynolds number
SO_2	Sulfur dioxide
U	Wind velocity
u_*	Friction velocity
V_j	Approximation Vector spaces
W_j	Details Vector spaces
Z	Partition function
z_0	Aerodynamic roughness length
z_o	Height above ground of the wind measurements

Chapter 1

Introduction

Atmosphere is dominated by a wide range of spatial and temporal scales, with continuous interactions taking place between the atmosphere itself and the earth's surface. Moreover, the impact of urbanization has been realized in a variety of aspects of life, ranging from the urban micro-climate and more broadly atmospheric research, to the energy demands for heating and cooling for indoor thermal comfort. Before we get to the point to predict reliably urban air quality, it is important to understand the physicochemical processes that occur in the urban atmosphere. This Chapter introduces the motivation and background as well as the objectives and contribution of this thesis. Finally, the structure and the overall outline of the thesis is provided.

1.1 Spatio-temporal scales in the urban atmosphere

1.1.1 Turbulence in the atmospheric boundary layer

Turbulent flows always occur at high Reynolds numbers and over a wide range of length and time scales. The Reynolds number is a non-dimensional number which shows the ratio between the inertial and viscous forces. For turbulence to develop, the inertial forces must be much larger than the viscous forces according to equation:

$$Re = \frac{UL}{\nu} \tag{1.1}$$

where U is the mean velocity of the flow, L is the characteristic length scale and ν is the fluid viscosity.

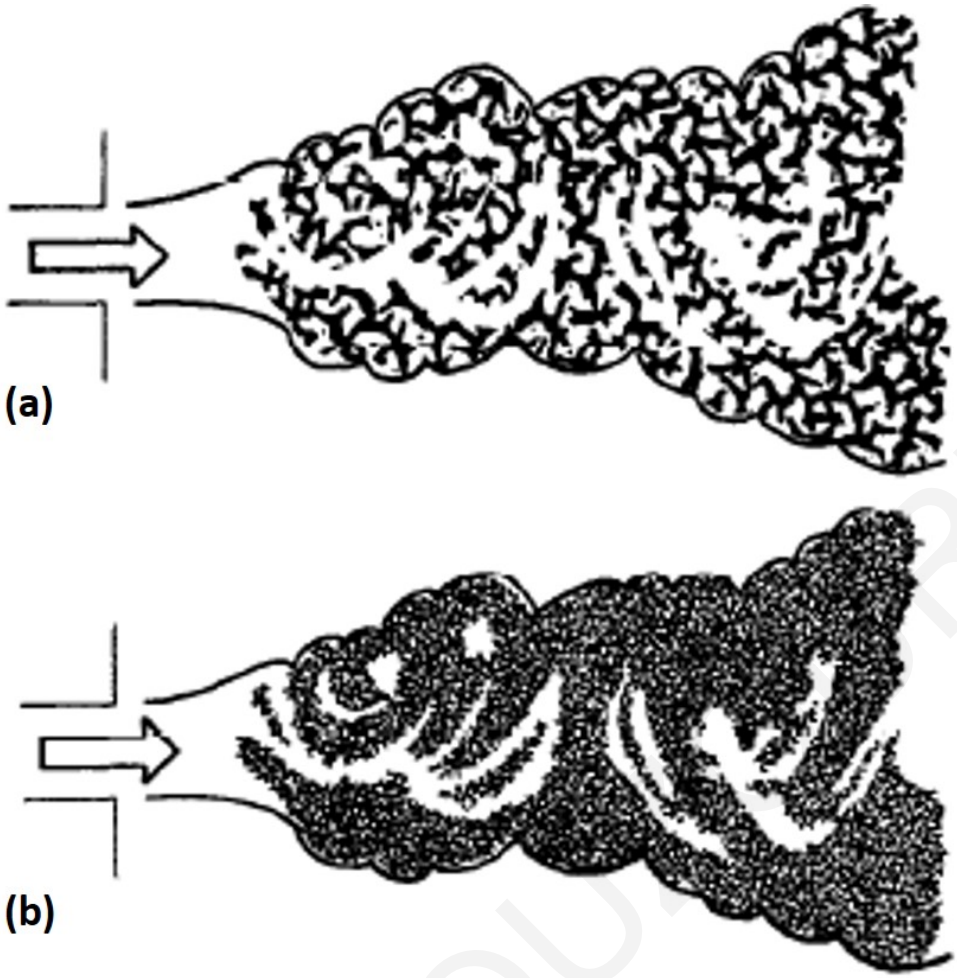

Figure 1.1: Turbulent jets at different Reynolds numbers (a) relatively low Reynolds number (b) relatively high Reynolds number (adopted from [105])

The range of scales that are encountered in a turbulent flow span from integral scale to Kolmogorov scale. Integral scale is called the larger scale that is determined by the physical boundaries of the flow and contains the full energy of the flow. The smallest length scale is called Kolmogorov length scale and is determined by viscosity. Fig. 1.1 illustrates a simple multi-scale problem where two different turbulent jet flows with different Reynolds number present the same integral scale. Thus, the two flows in integral scale seem identical. However, the two flows are entirely different. The main difference between the two turbulent flows is the size of the smallest eddies: a turbulent flow at a relatively low Reynolds number has a relatively *coarse* small-scale structure. Thus for the purpose of accurate prediction of the behavior of a multi-scale flow, there is a need for careful consideration of the scales to be modeled and their role.

The usual practice in multi-scale modeling of a physical flow phenomenon is done by parameterizing the effect of smaller scales and by considering the influence

of larger scales as the boundary conditions of the flow problem. The ultimate aim of multi-scale modeling is to arrive at an approach that shares the efficiency of the macroscopic models as well as the accuracy of the microscopic models. Therefore, there is a need to use techniques that are rigorous in extracting conclusions and deductions across the scales for any multi-scale problem, such as dynamic problems in the atmosphere.

An approach to study a turbulent flow (among other approaches [31]), is done by observing the long term timeseries of the flow velocity in the time (temporal variation of velocity at a single point) or in the space domain (spatial variation of velocity at multiple points). In order to study the correlation of velocity increments in a turbulent flow, Taylor [104] in 1935 proposed the use of Fourier Transform (FT) as a tool which can describe the complete behavior of turbulence. In the power spectrum three major (Fig. 1.2) spectral regions can generally be identified. The energy-containing range, where energy is produced by buoyancy and shear and this region appears in low frequency area of the spectrum. The second region is the inertial sub-range, where according to Kolmogorov's second hypothesis there exists an intermediate range of frequencies, for which energy cascades from larger to smaller scales with a power exponent law equals to $\beta = -5/3$. Finally, at the high frequency end of the spectrum, there is the dissipation range where viscosity dominates and the turbulent kinetic energy (TKE) is dissipated into heat.

Power spectra, like those in Fig. 1.2, are derived in the wavenumber (k) domain but the issue is that most of the times the data are obtained using time-resolved single-point measurements. In order to address this issue Taylor's frozen-in flow hypothesis [33], states that when the turbulent fluctuations evolve slowly compared to the mean velocity (i.e low turbulence intensities), temporal and spatial variations of flow velocities behave in the same way. In 1962, Kolmogorov modified the homogeneity assumption of the flow field by introducing an energy dissipation rate $\varepsilon(x)$ that varies with the spatial location x. Introducing a spatially-varying energy dissipation rate implies a multi-fractal behavior of the flow field [69].

This thesis studies the fully developed atmospheric turbulence, namely when inertial forces prevail over the viscous forces and very large turbulent scales occur in the flow. Flows in the atmosphere can easily fulfill essential criteria for the validity of Kolmogorov's theory at turbulent flows with inherent large Reynolds numbers. These criteria are that:

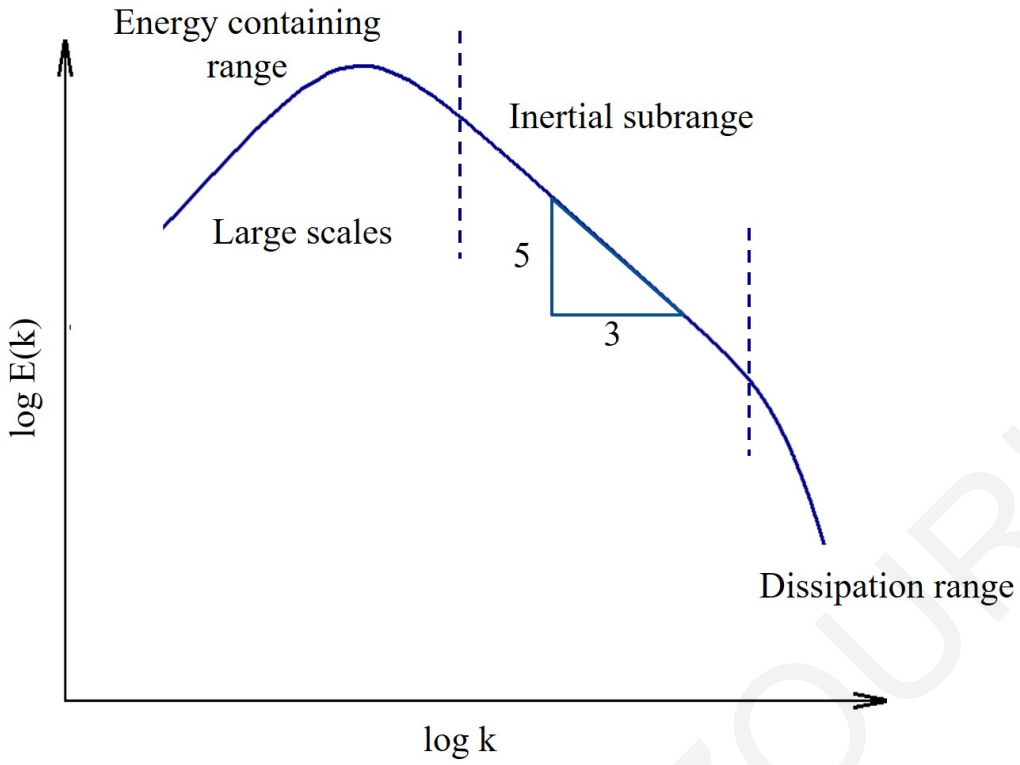

Figure 1.2: Three major spectral regions (i) energy-containing range, (ii) inertial subrange and (iii) dissipation range, in the power spectrum of spatial variation velocity of a flow

1. the ratio of the largest scale L of flow to the smallest Kolmogorov length scale l_k of flow is very large, i.e. $L/l_k \gg 1$, and

2. for the dissipation to be confined to the smallest scales, the ratio of the spectrum of the strain rate at the smallest scales to the strain rate at the largest scales must be larger than 1, i.e. $\varepsilon(\nu\varepsilon)^{(-1/3)}/(U^2/L)$, where kinematic viscosity, ν, and large-scale motions of the flow, U, were also necessary to be introduced in order to define a length scales.

When $Re^{0.75} \gg 1$ and $Re^{0.25} \gg 1$, criterion (1) and (2) are satisfied respectively.

Despite the significant and important steps that have been taken by scientists to understand the nature of turbulence, nevertheless there are still areas of application of turbulence that need to be studied more. For example the progress in our understanding of turbulence in the urban atmosphere has been slow mostly because of lack of availability of appropriate field datasets, that is associated with practical difficulties due to the inhomogeneity and specificities of the urban morphology. This thesis among other things, attempts to provide some insight about the behaviour of turbulence in the urban atmosphere.

1.1.2 Urban texture characterization

The boundary layer over an urban area is of particular interest as it is in this layer of the atmosphere that the majority of observations in urban areas are made [102]. It is the lowest part of the atmosphere and is influenced by the land use and the anthropogenic processes. It is therefore important to know what these observations represent.

Urban morphology characterization is crucial for the parametrization of boundary layer development over urban areas; one of the main complications is the three-dimensional (3D) variation of the urban canopies and textures, which are often reduced to and represented by a one-dimensional (1D) varying parametrization. For example, for the atmospheric boundary layer, we know that based on the Monin-Obukhov similarity theory [73], the vertical profile (Fig. 1.3) of the mean horizontal wind speed can be described by:

$$U(z) = \frac{u_*}{\kappa} \ln \frac{z-d}{z_0} \tag{1.2}$$

where $\kappa = 0.4$ is the von Karman constant, u_* is the friction velocity, and z_0 and d are the aerodynamic roughness length and the zero-plane displacement, respectively. It is important to note that Eq. 1.2 is valid within inertial sub-layer (constant-stress layer) and in conditions of neutral stability. In addition, it is noted that the aerodynamic parameters z_0 and d are physically realistic only if Eq. 1.2 is applied over a statistically homogeneous fetch [39].

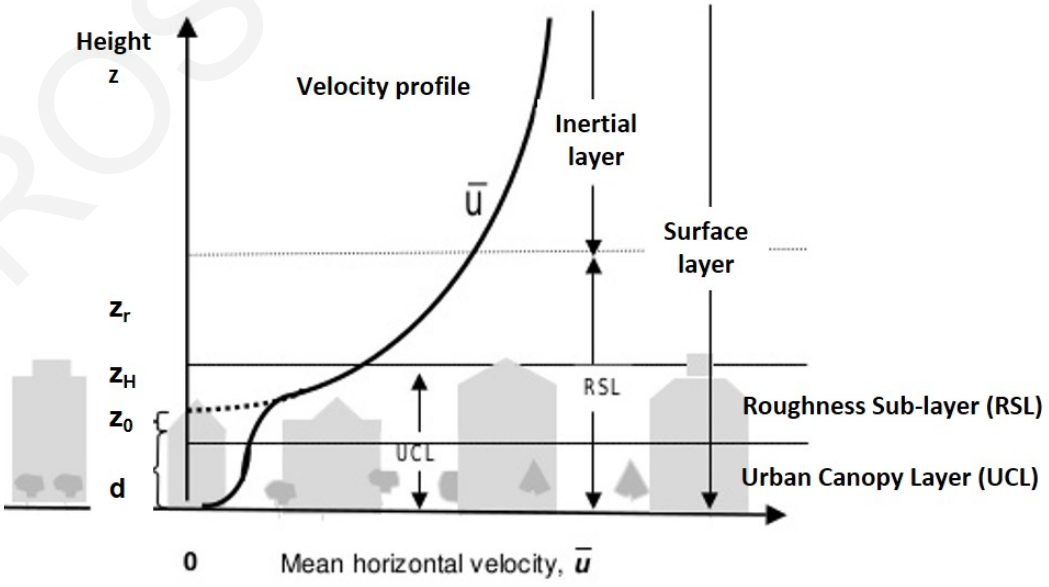

Figure 1.3: Schematic diagram showing the typical vertical profile of the mean horizontal wind velocity and scale lengths within an urban boundary layer, UBL.

1.1.3 Stochastic versus deterministic processes

In a broad range of disciplines, we find as main objective of the studies the understanding of the generating mechanisms that govern a process, for the purpose of modeling the process and forecasting its future values. For this purpose, the main form that is commonly used is timeseries data [112]. The ordering set of samples prescribed by the time (or space) index (e.g. minutes/hours/days/years or meter/kilometers etc.) is important, because usually enables us to unveil possible temporal (or spatial) correlation between the random variables of the stochastic process. Many of the processes occuring in the real world are stochastic, which means that these processes are not described by a deterministic law which controls the outcome. For example, turbulence in fluid dynamics, heart beat in cardiology, exchange rates in economic sciences and so forth, are stochastic processes of which it is not possible to predict their future values accurately [60]. Within the framework of this thesis, monitored meteorological and air-quality data are collected from a sub-urban station in the form of timeseries and they are analysed using WT analysis to gain insight into the multi-scale behavior of the sub-urban atmosphere.

A stochastic timeseries is described completely by all the joint probability distributions of its values. If the joint distributions remain invariant with respect to time the stochastic time series is said to be stationary; otherwise is non-stationary. The mathematical description of stationary stochastic time series is relatively simpler than that of non-stationary and it is well developed and documented. An important type of non-stationary time series, $X(t)$, that appears across a wide range of disciplines, is that whose joint distributions of their scaled -in-time versions, $P(X(\sigma t_1), X(\sigma t_2))$, are the same with the joint distributions of their scaled-in-values versions $P(\sigma^h X(t_1), \sigma^h X(t_2))$. In other words, a self similar system behaves in a similar way when viewed at different scales (scale-independent) on a dimension - space or time, either the system is stochastic or deterministic. If a non-stationary series can be made stationary by differencing d-times, this series is said to have d unit roots and the process $I(d)$ is called *difference stationary process of order d* [112]. For example, an $I(2)$ series contains two unit roots so the difference operation need to be applied twice to induce stationarity in the timeseries. The presence of unit roots means that the effects of an abrupt change to the system are not only persistent, but also they are propagated so that a given shock will have an increasingly large influence through

the time.

Thus, there is a need of using methods for optimization of modeling and forecasting of behavior stochastic processes like urban flow, turbulence and pollution dispersion in complex urban environments. These methods should be able to take into account the multi-scale nature of a process and be able to reveal scaling laws that may exist in atmospheric processes [74]. However, these processes often have the same behavior across different scales, exhibit the characteristic feature of self similarity and are governed by scaling laws. Multi-scale processes which present a scaling law or scaling laws, apart from self-similarity, can be characterized by the concepts of fractality or long-range correlation. Even though these notions are not equivalent, are connected and both posses a common characteristic, invariant relationship between different scales [97]. For example, fractals are repeating self-similar structures in a statistical sense, across all scales of the process.

It has been found that if a stochastic process is *difference stationary* process (i.e has stationary increments), the stationarity of the timeseries, and therefore the long-term correlation in timeseries fluctuations, is associated with a self-similarity index [1, 17, 27], the Hurst exponent (h), where h (among other things) measures how singular the process is in the neighborhood of a given observed value.

At this point, in order to highlight the usefulness of the Hurst exponent as a metric of characterizing a stochastic process, the notion of the singularity point should be introduced. In Complex Analysis, singularities are extremely important points that characterize the behaviour of analytic functions. Singularities are small-scale events which are scale invariant. A point at which the first derivative of $f(t)$ fails to exist, is called a singular point or singularity of the function. The Lipschitz exponent h (namely Hurst exponent for point or Hölder exponent for function) provides a uniform regularity measurement over time intervals or at any specific point v as well. If $h < 1$ at point v, then the function f is not differentiable at v, whereas h characterizes the singularity type.

In fluid dynamics problems wherein the stochastic approach is used to study turbulent flows, it was found that the asymptotic decay β of the power spectrum (see 1.1.1) is linearly related with the uniform irregularity index h of a process [75]. The limitation of power spectrum approach for determing the characteristic regularity (or singularity) of the analysing dataset is that the obtained characteristic regularity is global and it cannot describe the singularity at particular locations or points in the

timeseries. In 1974, to overcome this issue, Mandelbrot [66] introduced the notion of *singularity spectrum* $D(h)$ to study multi-fractal signals, which are signals with various singularities at different points.

Taylor's Eq. 1.3 relates differentiability of a signal with local polynomial approximations. If function $f(t)$ is m-times differentiable in $[v-\delta, v+\delta]$, Taylor's polynomial expansion in the neighbourhood of v is:

$$p(t) = \sum_{k=0}^{m-1} \frac{f^k(v)}{k!}(t-v)^k \tag{1.3}$$

and the approximation error $\epsilon(t)$ is calculated by

$$\epsilon(t) = f(t) - p(t) \tag{1.4}$$

If function $f(t)$ is $n = \lfloor h \rfloor$ times continuously differentiable at the point v and if there exists $M > 0$, the error $\epsilon_v(t)$ satisfies:

$$|\epsilon(t)| \leq M|t-v|^h, \forall t \in \mathbb{R} \tag{1.5}$$

and inserting Eq.1.4 in Eq.1.5

$$|f(t) - p(t)| \leq M|t-v|^h, \forall t \in \mathbb{R} \tag{1.6}$$

Eq. 1.5 implies that the Hurst exponent h determines the upper bound of $\epsilon_v(t)$. Thus $h_v > n$ measures how irregular the function f is at the point v. For example, a function f that is bounded but discontinuous at v $h_v = 0$, whilst if $h_v < 1$, then f is not differentiable at v and h characterizes the singularity type. More details about the Hurst exponent and its association with singular points and self-similarity in timeseries can be found in many textbooks, as for example in Mallat [64].

There are two different types of singular points: Isolated and non-isolated singular points. Isolated singularities are singularities where within a neighborhood of radius r, the function has no other singularities close to it. On the other hand non-isolated singularities are singularities where no such neighbourhood can be found and they appear in highly irregular signals such as multi-fractals signals. The two types of non-isolated singularities are: (i) Natural boundaries (i.e cusps) and (ii) Branch cuts (i.e ridge, edge, chirps).

As it has already been mentioned in the previous paragraph, the long-term correlation in timeseries fluctuations of a stochastic process, is associated with the

self-similarity index. Specifically, if a given stochastic process is *difference stationary* and exhibits exponents in the range $\frac{1}{2} < h \leq 1$, then the timeseries is said to have a long-term correlation behavior [3], which implies that a value of the timeseries is affected not only by its most recent values but also by its long-term history. For values of h in the range $0 \leq h < \frac{1}{2}$, the *difference stationary* process has short-term correlation and if $h = \frac{1}{2}$, the values of the timeseries are uncorrelated. Furthermore, if a given stochastic process is *difference stationary* and exhibits exponents in the range $\frac{1}{2} < h \leq 1$, then the timeseries has long-term correlation behavior [3], which implies that a value of the timeseries is affected not only by its most recent values but also by its long-term history. For $0 \leq h < \frac{1}{2}$ the *difference stationary* process has short-term correlation and if $h = \frac{1}{2}$, the values of the timeseries are uncorrelated.

1.2 Literature review

The literature review of this thesis will be divided into two parts. The first part deals with issues related to urban morphology description and modeling, while the second part concerns the description of atmospheric data as stochastic processes.

1.2.1 Urban morphology

A focus in atmospheric research has been the understanding and appropriate representation of the urban effects and particularly of their aerodynamic characteristics, used to describe the vertical variation of the mean horizontal wind velocity (U) in various numerical models. For example, meso-scale meteorological models rely on urban building datasets in order to determine several urban canopy parameters, such as the urban surface cover and morphological parameters, for accurate predictions of air quality and atmospheric pollution dispersion [9, 16, 93, 100]. Due to the multi-scale nature of air pollution dispersion, numerical modeling faces several challenges such as: (i) the spatial complexity of the underlying surfaces must be addressed, (ii) the spatial and temporal complexity of pollutant emissions must be addressed as well, (iii) applications require outputs at increasingly finer or adaptive grid resolutions in order to take into account the scale of observation.

The advantage of using Eq. 1.2 within numerical weather prediction models resides in the continuity with the surrounding rural areas, where a similar profile

to that depicted in Eq. 1.2 is adopted but with different z_0 and d parameters; in addition, the use of Eq. 1.2 has a negligible impact on the computational cost [67]. Unfortunately however, due to the inherent complexities of urban geometries there are great difficulties in correctly estimating the z_0 and d parameters for urban surfaces. Two classes of methods have been developed in order to estimate z_0 and d: (i) the morphometric methods that use the building elevation data to calculate the set of geometric input parameters that the forecasting model requires (e.g. [24, 89]) and (ii) the micro-meteorological methods that use field observations (e.g. [36, 38, 114]). However, in the absence of complete sets of wind-speed measurements, z_0 and d, frequently are estimated via the use of morphometric models, which relate these aerodynamic parameters to various geometric properties of the urban surface [37]. These models become increasingly attractive as substantial and detailed urban morphological data become available (e.g. Cities Revealed© The GeoInformation Group 2008). Moreover, it is well-established (e.g. [8]) that the airflow and associated dispersion processes within and above urban areas occur over a wide range of spatial scales. Specifically, four horizontal spatial scales have been introduced based on geophysical distinctions: (i) the regional scale, that is the larger surrounding area that is mutually influenced by the city area, extending up to several hundred km in the horizontal, (ii) the city scale, over which the urban area varies, i.e. up to 50 km, (iii) the neighborhood scale, which bridges the range of scales between street and city scales, i.e. from 0.2 to 10 km in the horizontal, and (iv) the street scale, up to 200 m in the horizontal [84]. Although these spatial scales can be unambiguously defined from the physical/geographical identification point of view, they are arbitrarily specified in terms of fluid dynamics, since the scale demarcation does not derive from the observing fluid dynamics but from the geographical identification perspective; this point becomes particularly important when model nesting and chemical reactions (and their corresponding time scales) need to be taken into account in association with the corresponding spatial and therefore time scale of mixing of pollutants to calculate the pollutant concentration field [78, 80].

Currently atmospheric numerical models addressing airflow and pollution dispersion are tailored to observe at a particular scale where the urban scale rather lies at one of the extremes of the range of scales present in the problem: large-scale weather models address regional- or global-scale variations, in which urban areas (and their associated effects) are represented as a parametrized effect, often occurring

at a sub-grid scale of the model; on the other hand, engineers most often addressing local-scale models (often of the building/street scale or neighborhood scale) acknowledge the need to use appropriate boundary conditions to reflect the city or the surrounding urban area that the buildings or neighborhood comprise, which in turn derive from a more macroscopic characterization of the city (e.g. [76, 86]).

It should be noted that the macroscopic characterization of such heterogeneous urban areas is always derived for a constant velocity and flow direction in relation to the urban morphology. Therefore, when describing surface-layer wind profiles it is normally necessary to calculate aggregated values of z_0 and d that account for the heterogeneity of the surface. This could be achieved so far, via source area modeling [94, 95] or blending methods [7]. Other studies have attempted to characterize such spatially heterogeneous geometries and roughness with an agglomerated z_0 and d (e.g. [53]) despite the fact that direct validation becomes difficult to fully address [18]. As a result of the emerging need for a spatially-varying characterization of urban morphologies, simple uniform square grids, "neighborhood regions", have been recently used, of horizontal resolutions ranging from 150 m to 1 km (by e.g. [6, 41, 89]). In order to provide such spatial variation of larger areas, morphometric models are then applied to the individual neighborhoods and the deduced parametrization schemes most frequently involve a statistical characterization of the urban building geometry, e.g. with the derivation of an average building height, a standard deviation in building height and the packing densities, all derived from a pre-specified area size (e.g. [83]).

Using the statistics of an urban morphology in the conventional way that is currently used is useful, as illustrated in the range of applications reviewed. However, such use of the statistics is unable to provide a distinctive characterization of a city or urban area; for example two urban sub-areas may yield the same statistics quantitatively, while being qualitatively different in morphology.

In a recent study by Millward et al. [71], a methodology was developed using an adaptive grid for providing a spatially-varying characterization of z_0 and d, as a function of the local planar packing density,λ_p, and local mean building height, $\bar{H}$, estimated using the morphological data within each grid cell. A convergence criterion (arbitrarily specified as admitted by authors) was also used in order to specify small-enough normalized changes (of either λ_p or $\bar{H}$) for statistical homogeneity and therefore to estimate the relevant aerodynamic parameters. It was accepted that, if

more stringent values than those specified for the convergence criterion in the study were used, the methodology failed to detect the city's boundaries, while if higher, more lenient, values for the convergence criterion were used, the results appeared to be unsatisfactory resulting into excessively small sub-areas. Finally, Millward et al. [71] concluded that there is a need for a more formal mathematical process to determine the most appropriate values of all these aerodynamic parameters.

There are two important implications arising from the existence of various scale-referenced models and the need for derivation of relevant parametrizations from various urban (or other) datasets of given pre-specified size: (a) the use of appropriate representation of urban (or other) datasets in the corresponding scale or resolution of a numerical model requires a coherent framework to associate the appropriate sets of data to be represented both in the model and sub-grid parametrizations, and (b) a spatially-varying characterization of any parametrization, e.g. the roughness length or zero-plane displacement should take into account the spatial heterogeneity in a structured and consistent way for any agglomeration of data. Therefore, for the purposes of improved modeling and forecasting of the behavior of urban winds, turbulence and pollutants dispersion, there is a need for finding a method which represents the spatial complexity of the urban morphology at different scales. The method used in this PhD thesis to understand and model multi-scale phenomena in the urban atmosphere is the multi-scale analysis method based on Wavelet Transform (WT), which has the capacity for multi-scale sampling and multi-scale representation of information. Comprehensive details about the theory and methodology of MRA will be given later in the manuscript in Chapter 2.

1.2.2 The multi-fractal behavior of stochastic processes

A number of multi-fractal methods such as Wavelet Transform Modulus Maxima (WTMM) [64] and Multi-fractal Detrended Fluctuation Analysis (Mf-DFA) [51] were developed and their performance was tested [40, 62], as methods allowing us to study complex objects which are not necessarily *fractal* but their variations exhibit self-similar behavior. In an attempt to carry out a comparative study between WTMM and Mf-DFA methods, Oświęcimka et al. [85] used different sorts of artificial signals generated by well-known mathematical model and found that WTMM performs poorly with signals that include singularities of strength $h > 1$. Thereby

they recommend the use of Mf-DFA method in the cases where one does not know a priori the fractal properties of a process or they suggest a careful use of WTMM method by choosing the proper parameters of the method. In this thesis, WTMM method was selected due to its inherent property of being well-localized in time, taking into considerations all the constrains and limitations that the method has.

During the last two decades, the aforementioned multi-fractal methods were applied at meteorological variables or wind-tunnel data to study their scaling properties. The application of Mf-DFA method on wind speed time series with different resolution [32, 54], indicate the presence of multi-fractal behavior. Furthermore, these studies show singularity spectra with dominant h exponent which do not coincide with Kolmogorov's second hypothesis, but without specification of under which atmospheric conditions this variation of exponents h is observed. This investigation is the novelty of the current study. Contrary to atmospheric field data, wind tunnel measurements, that inherently contain constraints on the spatial scale, appear to verify the Kolmogorov's ideas [46,106]. For example, longitudinal velocity signal obtained by Gagne and collaborators in the large wind tunnel $S1$ of ONERA at Modane (integral scale $L = 7m$, dissipation scale $n = 0.27mm$) was analysed using the WTMM method [75]. Results show that $D(h)$ is maximum at $1/3$, as predicted by the Kolmogorov second hypothesis.

On the other hand, Hosokawa and Yamamoto [43] in their study provide evidence against Kolmogorov's hypothesis on turbulence theory. In addition, there are studies were the multi-fractal methods were applied to time series of meteorological or air quality variables such as temperature [56, 57, 103], cloud structures [55], solar radiation [111] or particulate matter [113], where they reveal the multi-fractal structure of such timeseries measurements.

1.3 Objectives and Contribution of the thesis

This thesis is intended to provide useful insight and understanding to multi-scale phenomena in the urban atmosphere. The main objectives of this research are as follows:

1. To provide novel means for a scale-adaptive and spatially-varying representation of building data for multi-scale modeling studies. Within this framework,

the Multi-Resolution Analysis (MRA), is applied to the urban building datasets of a number of European and North-American cities in order to obtain rigorously scale-adaptive spatially-varying representations of the different urban datasets. As a result of the above, it appears that MRA results can be used in order to quantify the uniqueness of any urban area in essence a DNA-like description of a city.

2. To extend the use of MRA method to the derivation of spatially varying descriptions of more urban parameters, such as the aerodynamic urban canopy parameters or the building energy demand for heating and cooling.

3. To investigate the multi-scale nature of the fluid dynamics and dispersion in a turbulent atmosphere by using high-resolution atmospheric data.

Most of the results presented in Chapters 3-5 are based on published articles declared in Publications section.

1.4 Structure of the thesis

The main body of the thesis contains six Chapters and the content of each chapter is described below. Two Appendices are included to provide complementary explanatory background to the main body of the thesis.

Chapter 2 presents the fundamental framework of multi-scale analysis based on Wavelet Transform. Besides the description of the mathematical concepts that were used throughout this thesis, Chapter 2 describes comprehensively how some of the theory and the ideas implemented in the methodology can be interpreted through the output results.

Chapter 3 describes the atmospheric field measurements collected for the purpose of this thesis, as well as the processing methods that were used. Also a statistical description of datasets from seven (7) different cities is given, this involves three (3) European cities (London, Marseille and Nicosia) and four (4) North-American cities (New York City, Phoenix, Seattle and Oklahoma). The aim of this chapter is through description of the dataset to unveil qualitatively the spatial and temporal multi-scale nature of such data.

Chapter 4 contains an overview of the novel methodology Multi-Resolution Analysis (MRA), as a scale-adaptive spatially-varying representation method. Its

effectiveness is demonstrated in detail, in an example for Oklahoma City building data. Furthermore, this chapter, demonstrates the further application of MRA to urban building datasets for a number of European and North-American cities and it explores the connection between urban scale-building attributes, such as energy demands versus other urban dynamic features (e.g. city breathability).

Chapter 5 investigates the multi-scale behavior and explores them in terms of the stationarity and multi-fractality behavior demonstrated in high resolution atmospheric data. Moreover, through the Wavelet Transform Modulus Maxima (WTMM), the possible statistical connection between the atmospheric flow field and dispersion field was investigated.

Chapter 6 summarizes the main findings in this dissertation and provides recommendations for future research work. The main contributions of this research are also highlighted.

Chapter 2

Mathematical methods for multi-scale and multi-resolusion analysis

---

This Chapter, presents the fundamental mathematical tools of multi-scale analysis based on Wavelet Transform. Continuous Wavelet Analysis and its implementation in 1D atmospheric timeseries data will be presented first, followed by the definition of Orthogonal Wavelet Analysis and its implementation as a Multi-resolution Analysis in 2D building-related data. Also Chapter 2 describes how some of the theory and the methodology ideas can be interpreted through the output results.

2.1 Wavelet Transform: The *microscope* tool

Before we get to the point to predict the urban air quality, it is important to study and understand the physiochemical processes that occur in the urban atmosphere. In this direction, particular emphasis is given to understand multi-scale phenomena. This section presents the theory of Continuous Wavelet Analysis and how it is applied in 1D timeseries data, in the light of the discussion in the Chapter 1, about the stochastic processes and their multi-fractal behavior.

2.1.1 Short History of Wavelets

In signal analysis, the classical FT analysis represents the original information (signal) into the frequency domain. However, functions that are localized in the time

domain have Fourier spectra that are spread out across the frequency domain and vice versa [29]. In time-frequency analysis of a signal, like the way of analyzing turbulent flows (see Chapter 1), the classical FT analysis is inadequate. To overcome this drawback, Dennis Gabor in 1946, first introduced the Windowed-Fourier Transform, i.e. Short-Time Fourier Transform (STFT) known later as Gabor transform.

Wavelet analysis was originally introduced in order to improve seismic signal analysis by switching from STFT analysis to new better algorithms to detect and analyse abrupt changes in signals. In 1982 the French geophysicist Jean Morlet, introduced the concept of a *wavelet* which means small wave. Immediately, Alex Grossmann, a theoretical physicist, studied inverse formula for the WT. The joint collaboration of Morlet and Grossmann yielded a detailed mathematical study of the CWT and their various applications, of course without the realization that similar results had already been obtained in 1950's by Calderon, Littlewood, Paley and Franklin. The modern applications of wavelet theory are as diverse as wave propagation, data compression, signal processing, image processing, pattern recognition, computer graphics etc.

2.1.2 Wavelet Transform detects singularities

Wavelets are functions with compact support. Because they are irregular and often non symmetrical, they are good at describing constant frequency (stationary) signals, anomalies, pulses and other events that start and stop within the signal. Although the exact time and the exact frequency of a signal cannot be associated and determined simultaneously, a relationship between scale and frequency can be obtained. In addition to the concept of frequency which describes accurately the property of periodicity, another useful concept is that of scale, which is used to describe features with no-periodic properties. A WT is also adapted to analyse the scaling evolution of transients with zooming procedures across scales. In order to extract more information with regard to the multi-scale behavior of the measured quantities the CWT is used. The wavelet coefficients, $W(u,s)$, of a given time series $f(t)$ are given by:

$$W(u,s;f(t),\psi(t)) = \int_{-\infty}^{\infty} f(t)\frac{1}{\sqrt{s}}\psi^*(\frac{t-u}{s})dt \tag{2.1}$$

where $\psi(t)$ is the mother wavelet function, which is non-zero only over a finite time interval and its integral over that interval is zero. These two conditions render $\psi(t)$

a small wave, hence its name. The mother wavelet can be dilated or compressed through the scale parameter s. For $s > 1$, $\psi(t)$ is dilated whereas for $s < 1$ is compressed. In order to enable analysis for all the time period of $f(t)$, the dilated or compressed wavelet should be translated across the period that $f(t)$ is defined. This is achieved by the use of u, which is known as the translation parameter. The integral (2.1) is interpreted as a measure of similarity at a translation u between compressed or dilated versions of $\psi(t)$ and $f(t)$. If ψ function is real and has a zero average, a wavelet coefficient $Wf_v(u,s)$ measures the variation of f in a neighborhood of v that has a size proportional to s. For example sharp signal transitions create large-amplitude wavelet coefficients. A set of theorems [64] prove that wavelets which are well localized in time and decay towards low frequencies - meet the properties of compact support and have n vanishing moments respectively - result in wavelet transform to be interpreted as a multi-scale differential operator of order n [96]. The wavelet transform can be written as:

$$Wf(u,s) = s^n \frac{d^n}{du^n}(f \star \bar{\theta}_s)(u) \tag{2.2}$$

with $\bar{\theta}_s = s^{1/2}\theta(-t/s)$ and θ is the Gaussian function. The resulting $Wf(u,s)$ is the n^{th}-derivative of f averaged in the neighborhood of u and smoothed by a dilated version of the Gaussian function. The use of derivatives of Gaussian (DoG) function is proposed because DoG guarantee that all maxima lines propagate up to the finest scales. If $A = \int_{\infty}^{\infty} \theta(t)dt \neq 0$ then the convolution $f \star \bar{\theta}_s(t)$ can be interpreted as weighted average of function f at fine scales.

Wavelet modulus maximum is defined as a point (u_p, s_p) such that $|Wf(u,s)|$ is locally maximum at $u = u_p$. Mallat and Hwang [65] proved that f can be singular in the neighborhood of v if and only if there exists a constant number $A > 0$ and if there is a sequence of wavelet maxima points (u_p, s_p) that converges towards v at fine scales.

$$|Wf(u,s)| \leq As^{h+1/2} \tag{2.3}$$

$$\Leftrightarrow \log_2 |Wf(u,s)| \leq \log_2 A + (h + \frac{1}{2}) \log_2 s \tag{2.4}$$

Eq. 2.4 implies that Hurst exponent h, as defined in Subsection 1.1.3, is estimated by the slope of a log-log plot of the CWT amplitude versus the scale $log_2 s$. Mallat [64] underlies the concept that WT can find isolated singular events and characterize more complex multi-fractal signals having non-isolated singularities. These modulus

maxima points may or may not be along the same maxima line. As a result, all singularities are detected by following the wavelet transform modulus maxima at fine scales. This result is very useful for studying processes like multi-fractal signals since these are signals with singularities vary from point to point. In addition, a typical feature of a fractal signal is that it has a non-integer degree of differentiability.

Muzy et al. [75] in order to calculate the *singularity spectrum* $D(h)$, which depicts the range of different h that exist in a multi-fractal process, used a function called *partition function*. The *partition function* Z measures the sum at a power q of all wavelet modulus maxima. The idea of using a *partition function* Z was taken from statistical mechanics where Z connects the macroscopic thermodynamic quantities of a systems with the micro-state details of the system.

The data processing and analysis based on WTMM method, was implemented in Matlab© by using the software FracLab© v2.1 (*http://fraclab.saclay.inria.fr/*) which it was developed by INRIA.

2.2 Multi-Resolution Analysis (MRA)

Wavelets were developed before the conception of MRA and they constitute the fundamental building blocks of the Continuous Wavelet Transform (CWT). CWT exploits the intuitive notion of scale, as a multiple of time or space variable, in order to create a signal processing technique that enables multi-scale signal analysis. MRA through a set of axioms, introduced by Mallat [64] and Meyer [70], formalizes the notion of scale. The axioms of MRA provided theorems that stimulated the development of:

(a) orthogonal scaling functions and wavelets; the former are used to sample at various scales whereas the latter hold the details removed from lower scales during higher scale sampling, and

(b) fast analysis and synthesis algorithms.

In this thesis, MRA is proposed as a formal framework to represent urban morphologies consistently across different scales and resolutions of models and datasets for the derivation of associated boundary-layer parametrizations; this is mainly due to the capacity of MRA for multi-scale sampling [74]. By being able to represent the urban information (at each selected level-resolution) as an approximation and a

detail, it can provide appropriate and consistent representations of urban data across different scales and resolutions of models. Due to this capacity, MRA has been attractive for applications in several fields, e.g. in soil science for surface roughness characterization [48,110], in the detection of street features in urban fabric [4,21,42] as well as in environmental fluid dynamics [109] and turbulence characterization through coherent structure identification [26, 28–30, 45]. Recently it has been reported that the MRA provides the ability to retain and quantify the unique character of each and every city, and as a function of grid size [19].

The subsections that follow describe the MRA in the context of the application of this thesis. The current Subsection 2.2.1 describes the theory of 1D MRA whereas its extension to 2D is described in Subsection 2.2.2.

2.2.1 The 1D formulation of the MRA

MRA formalizes the notion of scale through labeled, by integers $j \in \mathbb{Z}$, subspaces V_j of the space $L^2(\mathbb{R})$ of finite energy signals as follows: each signal (or function) in V_j contains information up to resolution 2^j. In the theory of MRA a function, known as the scaling function $\phi(t)$, plays a prominent role, since it creates the subspaces V_j, it dictates the wavelet creation methodology and enables multi-scale sampling. Through MRA axioms it can be shown that the scaling function of support δt, has a pulse-like shape and can be normalized to unit area

$$\int_{-\infty}^{\infty} \phi(t)dt = 1 \tag{2.5}$$

The axioms of MRA postulate the existence of a sequence of nested subspaces, V_j of $L^2(\mathbb{R})$, such that $\ldots V_j \subset V_{j+1} \subset V_{j+2} \ldots$, where j denotes an integer, while the original signal f can be projected on to any of the subspaces, V_j, as f_j. Both f_j and V_j belong to the Hilbert function space of finite energy signals, denoted as $L^2(\mathbb{R})$ where $\mathbb{R}$ denotes the set of real numbers. In addition they postulate the existence of a scaling function that can be used to generate these spaces. The complete list of MRA axioms which can be found in many textbooks as for example [22,49,64].

Moreover, it is important to point out that the space V_j is considered to contain information up to resolution of $2^j\tau$. This means that V_j can be deconstructed into an approximation subspace V_{j+1} that contains information up to a resolution of $2^{j+1}\tau$. Furthermore the detail subspace contains the details removed from resolution $2^j\tau$ in

order to obtain the next level approximation with a resolution of $2^{j+1}\tau$ expressed as W_{j+1} is the orthogonal complement of V_{j+1} in V_j expressed as

$$V_j = V_{j-1} \oplus W_{j-1} \tag{2.6}$$

The most important mathematical consequence of MRA axioms is the existence of a function $\phi(t)$, the so-called scaling function, of compact support δt (bounded interval over which $\phi(t)$ is non-zero) whose translates $\left(\phi_n = \phi(t-n)\right)$ generate an orthonormal basis of V_0 (the space on which the original/initial f_s is projected).

Since any function that has a pulse-like shape and satisfies Eq. 2.5 can be used to approximate the impulse function it can furthermore be used to sample a function at a higher scale, as opposed to the actual values sampled at sharp instants by the impulse function.

In addition since $V_j \subset V_{j+1}$, the following functional equation of the scaling function ϕ, called dilation equation can be deduced,

$$\phi(t) = \sqrt{2}\sum_n h_n \phi(2t-n) \tag{2.7}$$

where the coefficients h_n are given by $h_n = \langle \phi(t), \phi(2t-n) \rangle$ and they can be thought of as a sequence of low-pass filter coefficients. These coefficients determine the scaling function and they are very important because, (a) they are used to construct the wavelet function, and (b) their convolution with the analyzing signal yields computational analysis and synthesis procedures.

Wavelet functions in MRA are created through the orthogonal complements, W_{j-1}, of V_{j-1} in V_j. As consequence an $f_j \in V_j$ can be decomposed into

$$f_j = f_{j+1} + d_{j+1} \tag{2.8}$$

where f_{j+1} and $d_{j+1} \in W_{j+1}$. f_{j+1} is interpreted as the approximation of f_j at the scale 2^{j+1} whereas $d_{j+1} \in W_{j+1}$ as the detail of g_j that exists at scale 2^j but is lost at scale 2^{j+1} in order to get f_{j+1}. Given an integer $k > j$ by recursively substituting f_l where $j+1 < l \leq k$ in Eq. 2.8 can be written as

$$f_j = f_k + \sum_{l=j+1}^{k} d_l \tag{2.9}$$

which is the sum of its approximation at scale 2^k with the sum of all its details lost from the intermediate scales between 2^j and 2^k.

As in the case of the approximation spaces V_j, each space W_j has orthonormal basis constituted by translated and dilated versions, $\psi_{j,n} = \frac{1}{\sqrt{2^j}}\psi\left(\frac{t-2^j n}{2^j}\right)$ of a function $\psi \in W_0$, called the mother wavelet. A signal $f \in L^2((R))$ can be projected on a function $d_j \in W_j$

$$d_j = \sum_n \langle f, \psi_{j,n}(t)\rangle \psi_{j,n}(t) \tag{2.10}$$

Therefore the detail removed from approximation f_{j-1} to obtain f_j at higher scale is kept by the inner products $\langle f, \psi_{j,n}(t)\rangle$. Since $\psi(\frac{t}{2})$ belongs to W_1 and W_1 is the orthogonal complement to V_1 in V_0 then $\psi(t)$ can be written as

$$\psi(t) = \sqrt{2}\sum_n g_n \psi(2t - n) \tag{2.11}$$

where g_n are considered as coefficients of a differencing (high-pass) filter. These coefficients can be obtained from the averaging coefficients h_n by

$$g_n = (-1)^n \bar{h}_{1-n} \tag{2.12}$$

where the over-line denotes complex conjugation.

In applications, analysis is done on a sampled signal f_s assumed to belong to V_0 and hence it is set to f_0. Then f_0 is decomposed up to a level k according to Eq. 2.9 and reconstructed back according to

$$f_0 = f_k + \sum_{l=1}^{k} d_l \tag{2.13}$$

Fig. 2.1 depicts diagrammatically the decomposition and reconstruction. In this figure the corresponding levels and subspaces are identified. The maximum value of k is dictated by the number of samples of f_0 and the actual wavelet is used. The functional Eqs. 2.11 and 2.7 are satisfied by many different sets of coefficients h_n and g_n. This means that there is a multitude of different mother wavelets and scaling functions. In the light of the application of MRA on urban building datasets, Section 4.1 describes the properties and the selection rationale of these functions.

2.2.2 The 2-D formulation of the MRA

MRA can also be defined on $L^2(\mathbb{R}^2)$, the space of 2-D finite energy signals $f(x, y)$, by taking the tensor product [64]

$$V_j^2 = V_j \otimes V_j \tag{2.14}$$

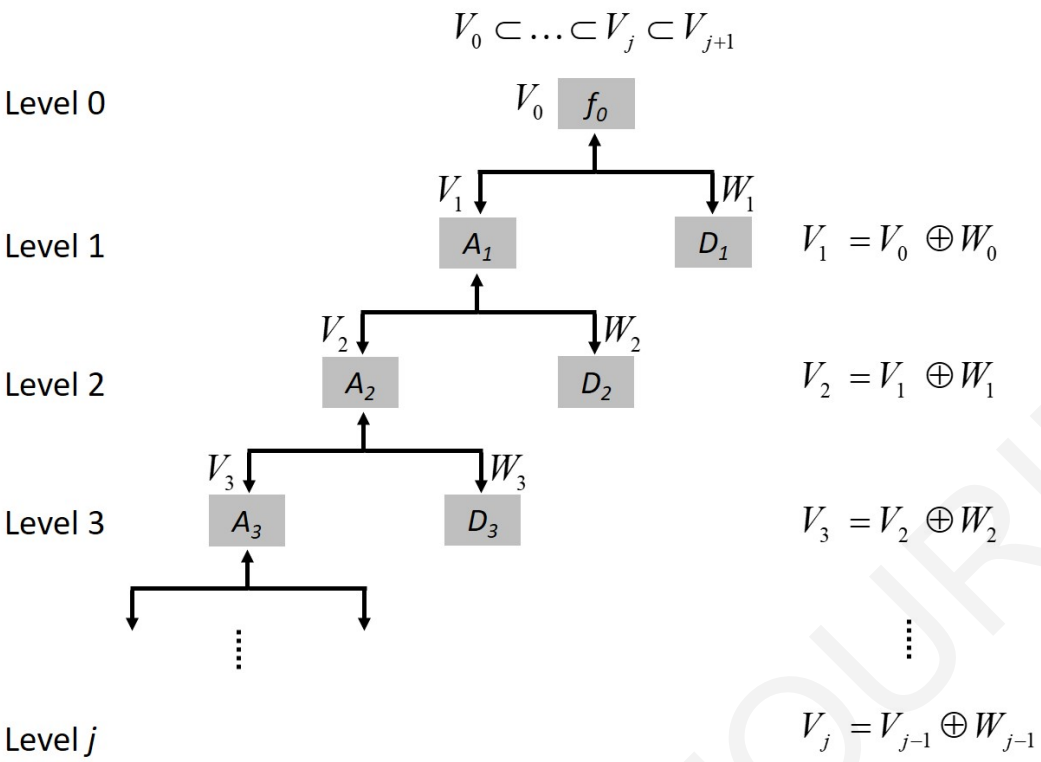

Figure 2.1: The 1D decomposition and reconstruction of a sampled signal f_0

of the approximation spaces V_j of the 1D MRA.

As a consequence of the tensor product a scaling function, $\phi(x, y) \in V_j^2$, associated with the 2D MRA is obtained by the product of the scaling function ϕ with itself,

$$\phi^2(x, y) = \phi(x)\phi(y) \tag{2.15}$$

Therefore, MRA for $L^2(\mathbb{R}^2)$ can be defined by a sequence of nested subspaces $\ldots V_j^2 \subset V_{j+1}^2 \subset V_{j+2}^2 \ldots$. The basis of each V_j^2 is given by the translated dilated versions $\phi^2_{j(n_1,n_2)} = \phi_{j,n_1}(x)\phi_{j,n_2}(y)$ $j, n_1, n_2 \in (Z)$ of the scaling function $\phi^2(x, y)$. The basis of the orthogonal complements, W_{j+1}^2 , of V_{j+1}^2 in V_j^2 constitute the 2D wavelets. The basis can be constructed from the 1D basis of V_j and W_j by noticing that,

$$V_j^2 = V_j \otimes V_j = V_{j-1}^2 \oplus W_{j-1}^2 \tag{2.16}$$

and then by substituting $V_{j-1}^2 \oplus W_{j-1}^2$ and exploiting the distributive property of $\oplus$ over $\otimes$ it can be shown that

$$W_{j-1}^2 = (V_{j-1} \otimes V_{j-1}) \oplus (W_{j-1} \otimes V_{j-1}) \oplus (W_{j-1} \otimes W_{j-1}) \tag{2.17}$$

and hence it can be deduced that the basis of W_{j-1}^2 are the dilated and translated versions of the following functions,

$$\psi_{hor}^2(x, y) = \phi(x)\psi(y) \tag{2.18}$$

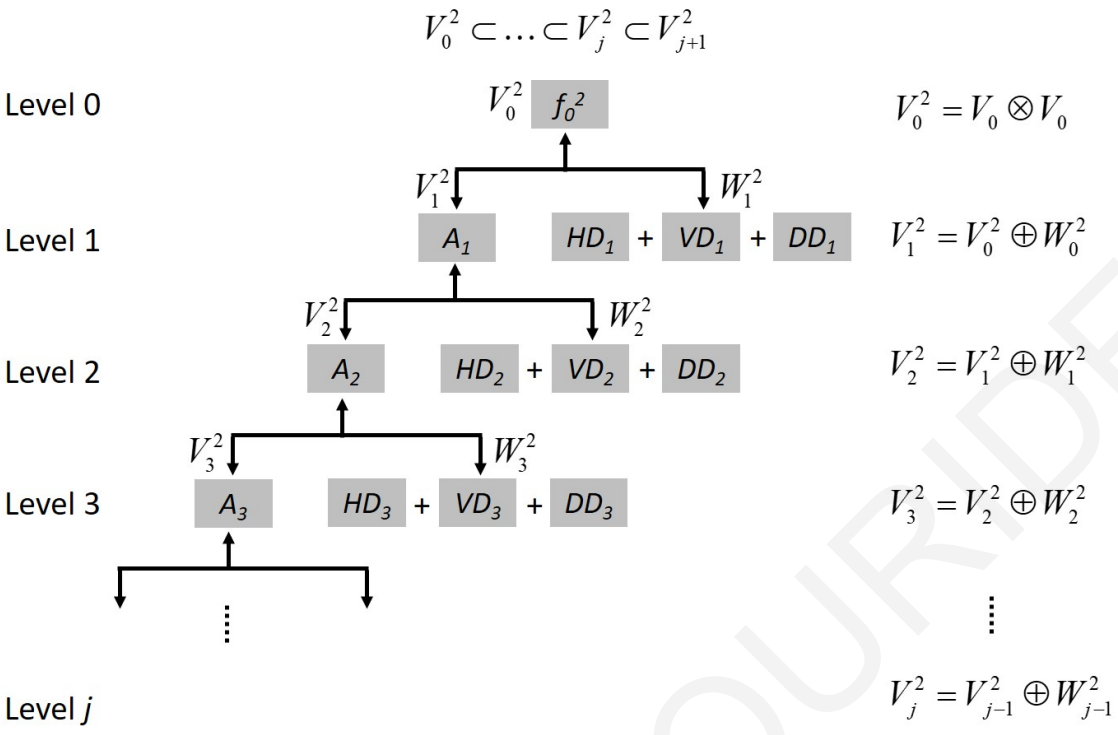

Figure 2.2: The 2D decomposition and reconstruction of a sampled signal f_0^2

$$\psi_{ver}^2(x,y) = \psi(x)\phi(y) \tag{2.19}$$

$$\psi_{diag}^2(x,y) = \psi(x)\psi(y) \tag{2.20}$$

which play the role of the 2D wavelets.

A 2D signal, i.e. an image $f_j(x,y) \in L^2(\mathbb{R}^2)$ can be projected on an $f_j(x,y)$ in $V_j^2 = V_j \otimes V_j$ by,

$$f_j(x,y) = \sum_{n_1,n_2=-\infty}^{\infty} \langle f(x,y), \phi_{j,(n_1,n_2)}^2 \rangle \phi_{j,(n_1,n_2)}^2 \tag{2.21}$$

Similar to the 1D case $f_j(x,y)$ is interpreted as the approximation of f at scale $2^j \delta x \delta y$, which is reconstructed from its samples $\langle f(x,y), \phi_{j,(n_1,n_2)}^2 \rangle$ taken at the same scale.

According to Eqs. 2.18-2.20 three separate projections, $d^{V_j \otimes W_j}$, $d^{W_j \otimes V_j}$, $d^{W_j \otimes W_j}$ in the corresponding orthogonal spaces $V_j \otimes W_j$, $W_j \otimes V_j$, $W_j \otimes W_j$ can be obtained. The projection in $V_j \otimes W_j$ is obtained by,

$$d_j^{V_j \otimes W_j}(x,y) = \sum_{n_1,n_2=-\infty}^{\infty} \langle f(x,y), \psi_{(n_1,n_2)}^{V_j \otimes W_j}(x,y) \rangle \psi_{(n_1,n_2)}^{V_j \otimes W_j}(x,y) \tag{2.22}$$

and the projections in $W_j \otimes V_j$ and $W_j \otimes W_j$ are obtained by using similar equations.

Approximations at higher scales, (lower resolutions) are obtained by removing details along the horizontal, vertical and diagonal directions of the image. The

details removed across the vertical, horizontal and diagonal directions are given by the inner products $f(x,y), \psi_{n_1,n_2}^{V_j \otimes W_j}(x,y)$, $f(x,y), \psi_{n_1,n_2}^{W_j \otimes V_j}(x,y)$ and $f(x,y), \psi_{n_1,n_2}^{W_j \otimes W_j}(x,y)$ respectively.

As a consequence an $f_j(x,y) \in V_j^2$ can be written as,

$$f_j(x,y) = f_{j+1}(x,y) + [d_j^H(x,y) + d_j^V(x,y) + d_j^D(x,y)] \tag{2.23}$$

or

$$f_j(x,y) = f_k(x,y) + \sum_{l=j+1}^{k} (d_l^H(x,y) + d_l^V(x,y) + d_l^D(x,y)) \tag{2.24}$$

which indicates that 2D MRA decomposes iteratively a given two dimensional signal, $f(x,y)$ to smoother parts at larger scales by removing *details* from lower scales.

2.2.3 Interpretation of 2D MRA methodology

In the light of the application of MRA in meso-scale atmospheric modeling what follows below is a short interpretation of MRA methodology description. Approximation at level 1 is obtained by an averaging process over cells of size of 2×2 pixels (of the original resolution); similarly approximation at level 2 is obtained by an averaging process over cells of size of 2×2 cells of the previous resolution (i.e. of 4×4 pixels of the original resolution) and similarly for all the subsequent levels, with approximation at the k^{th} level being the result of the averaging process over a cell of $2^k \times 2^k$ pixels of the original resolution.

The selection of the proper scaling and wavelet functions in the MRA is dictated by the nature of the application. For urban datasets the square shape of the *Haar* function is proposed, since it enables the demarcation of the characteristics of an urban area domain, where buildings have similar square- or rectangular-like shapes. An additional advantage of the *Haar* function is that its operation corresponds to simple averaging and differencing of 2 cell $\times$ 2 cell neighbourhoods [82]. Since this is the first time that MRA is applied in the field of atmospheric modelling and particularly in relation to urban effects, this Subsection illustrates the selection rationale of the analysing function, by means of a comparison between the *Haar*, *Symlet 4* and *Daubechie 4* scaling and wavelet functions. Fig. 2.3 shows the 1-D and 2-D *Haar*, *Symlet 4* and *Daubechie 4* scaling and wavelet functions.

The shape of the *Haar* scaling function dictates that all the values in the neighbourhood are equally weighted. For instance, at the first level of decomposition,

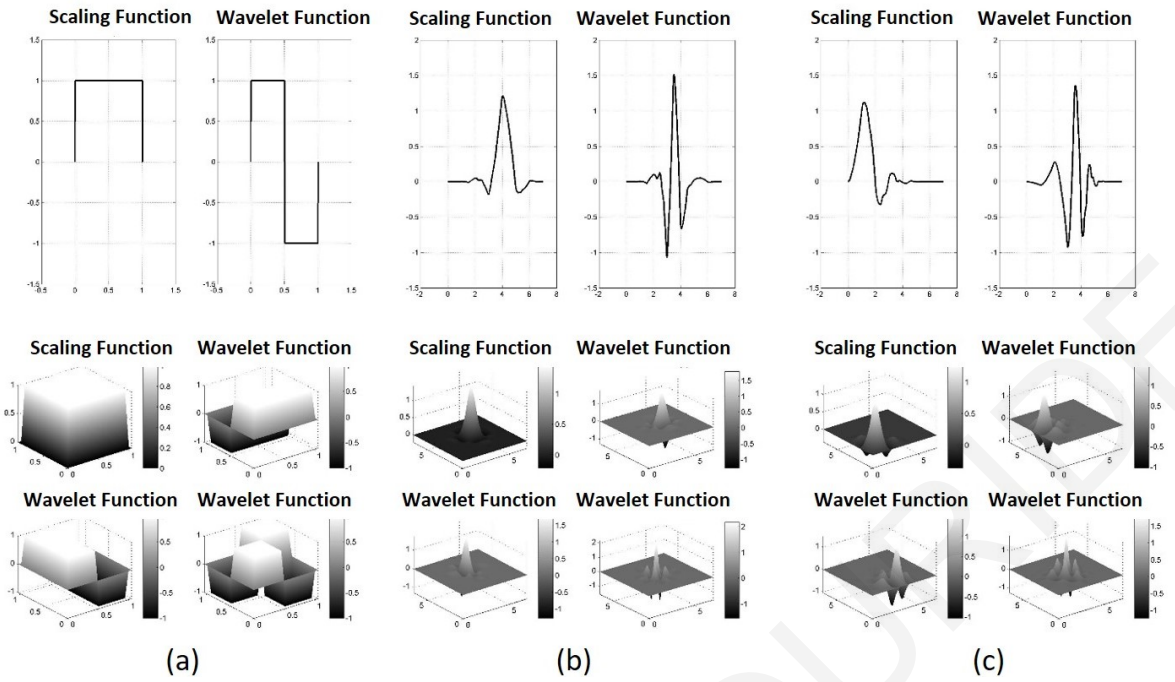

Figure 2.3: The Haar and Symlet 4 scaling and wavelet functions illustrated in 1-D (top row) and 2-D (bottom row) forms.

the *Haar* wavelet transform performs sequential averaging and differencing of 2×2 adjacent pixels; conceptually, this process can be viewed as a structural averaging process in which the height difference between adjacent buildings in the horizontal (x_1), vertical (x_2) and diagonal directions is tracked. On the contrary the *Symlet 4* and *Daubechie 4* scaling functions weigh unequally the corresponding values. *Symlet 4* adds the highest weight to the central value of the neighbourhood and then the weights decay symmetrically towards the boundaries of the neighbourhood. On the other hand, *Daubechie 4* adds most of the weight to the values of the left boundary in 1D cases and at the bottom left corner in the 2D cases. So, due to the shape of the *Symlet 4* and *Daubechie 4* functions, they could be used for example in detecting or capturing phenomena dominated by peaks or sudden occurrences. Thus for the MRA analysis of building database information it is recommended that the *Haar* analysing function is used.

If we consider that we apply the *Haar* analysing function on urban building datasets (due to its particular characteristics as discussed before, the value of each of the resulting cells in the yielded approximation at each level of the analysis corresponds to the weighted average of the height over the entire cell area. Alongside, Horizontal (HD), Vertical (VD) and Diagonal (DD) details at the same level of analysis are directional averaging and differencing in the corresponding directions. Fig.

2.2 depicts the approximation and details obtained at different level: for example in the third row of 2.2, the approximation of image f_0^2 at level 2 obtained from the MRA of the approximation at level 1, while the remaining three images HD_2, VD_2, DD_2 show the details removed from the approximation at level 1 in order to obtain the approximation at level 2. The size of the cells in the images of the approximations is determined by the size of the support of the scaling function at the corresponding scale. In order to obtain HD_2 the values of four specific cells from image at level 1 are firstly averaged across the rows, and subsequently, the difference of the values resulting from the averaging process and appearing in the same column are computed. This reflects the *Haar* analysing function part depicted under the title wavelet function (1) in Fig. 2.3a, where over its first half support takes the value 1 and over its first other half support the 1 value. As a consequence, in the plot of Fig. 2.2 entitled HD_2, adjacent cells, above or beneath each other, have opposite values. This indicates the changes at the scale $2^1 d_{x1} \times 2^1 d_{x2}$ along the vertical direction. A similar operation of that discussed above, but performed in the other direction, namely row differencing first and then column averaging, gives the plot entitled VD. It is evident that the outcome is the average of the differences and again, due to the support shape of the *Haar* analysing function, horizontal neighbouring cells have opposite values. This indicates the changes of the $2^1 d_{x1} \times 2^1 d_{x2}$ scale along the horizontal. Finally, in a similar way, DD_2 image represents the actual computations that generate the DD_2 image plot at level 2 as also indicated by Eq. 2.20. A more detailed description of the methodology in the light of the application of MRA on urban building datasets is given in Section 4.1.1.

The MRA analysis was implemented in Matlab© using its wavelet toolbox. It is important to note that in MRA analysis, the number of computations required to analyse a signal composed of N samples is proportional to N. For example using an i5 CPU 2.4 GHz, the time elapsed during the MRA of a dataset at a resolution of 1195×1185 pixels is 6.24 sec.

Chapter 3

Summary of survey datasets

The aim of this chapter is to present an overiew of the datasets to be used in this thesis for unveiling their multi-scale nature. The data involves atmospheric field measurements and urban building data for various cities. In this chapter, the atmospheric field measurements which were collected, are presented as well as the various building-related attributes of seven (7) different cities are described: three (3) European cities (London, Marseille and Nicosia) and four (4) North-American cities (New York City, Phoenix, Seattle and Oklahoma). This way of presentation (i.e. first the discrete 2D data topics are presented followed by the presentation of timeseries data topics) is retained in all subsequent chapters of the thesis, clearly due to practical reasons, since the elaboration of this thesis began by analysing 2D discrete data related to urban morphology.

3.1 Building geometry-related datasets

The classical description of spatially heterogeneous urban landscapes most frequently involves a statistical characterisation of the buildings in a certain region by a mean building height $\bar{H}$, a standard deviation of the building height σ, and the packing densities - the fraction of the plan surface area covered by building elements, λ_p and the frontal area index of the elements, λ_f, as a function of wind direction - which in turn determine the aerodynamic characteristics of the urban area (e.g. aerodynamic surface roughness length z_0 and zero-plane displacement d) [89], as described in the following equations:

$$\bar{H} = \frac{\sum_{i=1}^{m} H_i}{m} \tag{3.1}$$

$$\sigma = \sqrt{\frac{\sum_{i=1}^{m} (H_i - \bar{H})^2}{m-1}} \tag{3.2}$$

$$\bar{H}_{AW} = \frac{\sum_{i=1}^{m} H_i A_{p,i}}{\sum_{i=1}^{m} A_{p,i}} \tag{3.3}$$

$$\lambda_p = \frac{\sum_{i=1}^{m} A_{p,i}}{A_T} \tag{3.4}$$

$$\lambda_f = \frac{\sum_{i=1}^{m} A_{f,i}}{A_T} \tag{3.5}$$

where m is the total number of buildings in the urban datasets and A_T is the total planar area of the domain.

A number of models has been developed that attempt to relate the aerodynamic roughness length (normalized over the mean building height), $z_0/\bar{H}$, and the zero-plane displacement (normalized over the mean building height), $d/\bar{H}$, to the simplified geometrical parameters of the underlying surface; the plan and frontal area densities, λ_p and λ_f respectively (e.g. [47,52,63,90,91,99]). An important issue is the difficulty of accurately estimating z_0 and d from measurements, which arises from some associated inconsistencies between the experiments and the methodologies used to estimate these parameters. Consequently, there is large scatter in reported values of z_0 and d, even from wind-tunnel experiments over identical uniform arrays [37]. A comprehensive review of many of these models concluded that, in real urban areas, estimates of both z_0 and d parameters can be highly uncertain [37]. Despite this uncertainty there have been a few methods based on morphometric concepts proposed to determine both z_0 and d. The methods are divided into three sets:

(i) the simplest and most frequently used set is the height-based rule-of-thumb, that z_0 and d are directly proportional to the mean building height

(ii) the second set utilizes the fraction of the plan surface area covered by roughness elements λ_p and

(iii) the third set uses the frontal area index of the elements as a function of wind direction, λ_f.

Here, the morphometric relations proposed by Kastner-Klein and Rotach [52] were used as an example. These morphometric relations were derived based on wind-tunnel measurements over a scaled model of a real city area in order to deduce z_0 and d over the λ_p packing density parameter, as follows:

$$\frac{z_0}{\bar{H}} = 0.072\lambda_p[exp\{-2.2(\lambda_p - 1)\} - 1] \tag{3.6}$$

$$\frac{d}{\bar{H}} = 0.4\lambda_p[exp\{-2.2(\lambda_p - 1)\} + 0.6\lambda_p] \tag{3.7}$$

Although such urban morphological measures are useful in certain type of problems, they are unable to describe uniquely an urban area or the city as a whole in atmospheric modeling; two cities or urban areas could yield the same or very similar UCPs, while being quite different in morphology and thereby in aerodynamic behavior. In addition these values of $\bar{H}$, λ_p for example, depend on the size of the domain (neighborhood) and may not necessarily be representative of the scale and grid size of the simulation. In fact, the methodology used is not sensitive to the exact morphometric model used for the derivation of the aerodynamic parameters. The discrepancies noted in the recent literature (e.g by [72]), as arising from the planar packing densities estimated over different domain area sizes and the associated parametrization of z_0 and d are attributed to the weakness to relate and reference morphology parameters at different scales, that the MRA methodology can formally address and therefore overcome. This will be discussed further in the light of the results in Chapter 5.

3.1.1 Overview of the building datasets of survey cities

The 2D data information that was used in this thesis is simply a pixilated image of the urban area, where the value of each pixel refers to the height of the built element above the ground. Therefore, it gives a full, three-dimensional description of the urban building area. In the representation of the λ_p as a pixilated image, each pixel of the image with the original (highest) resolution, a pixel that represents part of a built area or a building gets a value of 1 while open, unbuilt pixel areas get a value

of 0. During this conversion process the pixel resolution must be chosen, and this is important in determining how accurately the geometry is represented. For all datasets that were used, each pixel corresponds to a $1m \times 1m$ area and the color of each pixel maps to the corresponding building height.

Conventional statistics of the $\bar{H}$ and λ_p of the depicted urban area within each city are summarized in Table 3.1. The statistical analysis is based solely on the data that we had at our disposal. The results are considered very satisfactory as they do not differ by more than 5% from the corresponding values found in the literature

Table 3.1: Comparison of statistical building height parameters

	Domain Size	Mean Building Height $\bar{H}$ (m)	Standard Deviation σ (m)	Area-Weighted Mean Building Height $\bar{H}_{AW}$ (m)	Planar Packing Density λ_p
London	$1112m \times 1253m$	22.20	6.66	22.52	0.29
Marseille	$650m \times 825m$	9.11	5.50	10.67	0.21
Nicosia	$600m \times 610m$	8.10	3.66	8.38	0.40
New York	$1420m \times 1780m$	71.78	54.39	60.67	0.51
Oklahoma	$1310m \times 1280m$	25.17	27.35	22.77	0.22
Phoenix	$1590m \times 1730m$	16.23	21.24	18.21	0.26
Seattle	$1480m \times 1700m$	35.23	39.49	32.04	0.26

What follows below is a short description of each dataset for each city.

(a) *London*: London is the largest city of the United Kingdom. The study area for the purposes of this thesis is located in Paddington area. The extent of the study area is approximately rectangular and covers an area of $1112m \times 1253m$ (Fig.3.1). The plan area fraction, λ_p, of the investigated area is 0.29 and the mean building height, $\bar{H}$, is 22.2 m with a standard deviation, σ, of 6.66 m (Table 3.1).

(b) *Marseille*: Marseille is the second largest city in France and is located on the southeast coast of France; thus it can be considered as a typical Mediterranean city. The study area is an area of the city called Saint Marcel. This study focuses on an area of $640m \times 825m$ (Fig.3.2). The plan area fraction, λ_p, in the study area is 0.21 and the mean building height, $\bar{H}$, is 9.1 m with a standard deviation, σ, of 5.5 m (Table 3.1). The building dataset was obtained in the framework of the EUREQUA ANR project and is based on data from the French National Geographic Institute (IGN).

(c) *Nicosia*: Nicosia is the capital and largest city on the island-country of Cyprus and its morphological structure reflects that of a Mediterranean city. The study area is centred around Ledras Street which is characterized by densely packed buildings of one or two stories-high with irregular footprints, flat terrace-type roofs, and internal courtyards. This study focuses on an area of $600m \times 610m$ (Fig.3.3). The plan area fraction λ_p in the study area is 0.40 and the mean building height $\bar{H}$ is 8.1 m with a standard deviation σ of 3.7 m (Table 3.1). The urban building dataset, was derived from the European Research Project TOPEUM [76].

(d) *New York City*: New York City is the most populous city in the U.S.A. and it is characterized by its many skyscrapers and some of the tallest buildings in the world. The study area is located in Midtown Manhattan just to the south of Central Park and covers an area of $1420m \times 1780m$. (Fig.3.4). The plan area fraction, λ_p, in the study area is 0.51 and the mean building height, $\bar{H}$, is 71.8 m with a standard deviation, σ, of 54.4 m (Table 3.1). The building data set was obtained from the National Geospatial-Intelligence Agency (NGA).

(e) *Oklahoma*: Oklahoma is the capital and the largest city of the U.S.A. State of Oklahoma. The investigated area is the Central Business District (CBD) and derives from the urban dataset by Burian et al. [10]. The dataset covers an area of $1310m \times 1280m$ (Fig.3.5) with a plan area fraction, λ_p, of 0.22, a mean building height, $\bar{H}$, 25.2 m and a standard deviation, σ, of 27.4 m. (Table 3.1).

(f) *Phoenix*: Phoenix is the capital and largest city of the U.S.A. State of Arizona, as well as the sixth most populous city in the U.S.A.. The corresponding building data covers a study domain of $1590m \times 1730m$ (Fig.3.6) and includes almost the Phoenix downtown core [12]. The plan area fraction, λ_p, in the study area is 0.26 and the mean building height, $\bar{H}$, is 16.2 m with a standard deviation, σ, of 21.2 m (Table 3.1).

(g) *Seattle*: Seattle is the largest city in the Pacific Northwest region of the U.S.A.. The building data cover mainly the Seattle downtown area (Fig.3.7) and extend over a domain of $1480m \times 1700m$ [11]. The plan area fraction, λ_p, in the study area is 0.26 and the mean building height, $\bar{H}$, is 35.2 m with a standard deviation, σ, of 39.5 m (Table 3.1).

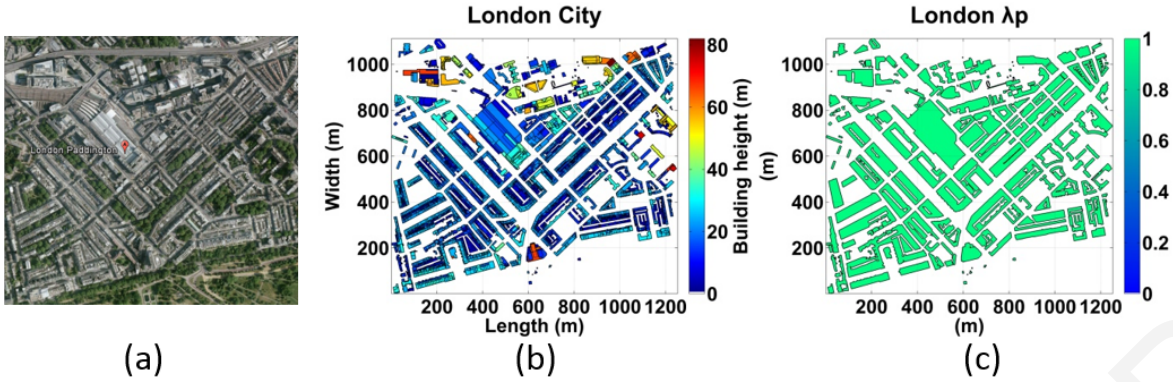

Figure 3.1: Building elevation dataset of London ($1112m \times 1253m$). (a) Left side images depict the Google image of study area. (b) Right side images depict the digitized building elevation datasets. Each pixel corresponds to $1m \times 1m$.

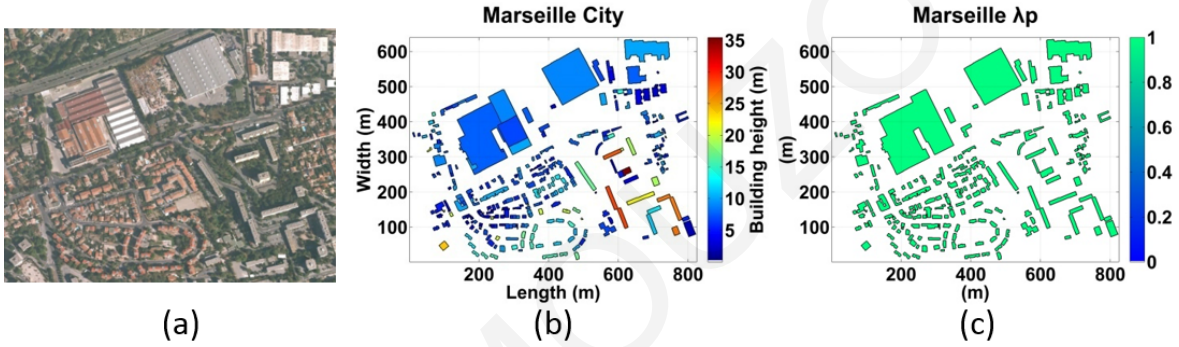

Figure 3.2: Building elevation dataset of Marseille ($640m \times 825m$). (a) Left side images depict the Google image of study area. (b) Right side images depict the digitized building elevation datasets. Each pixel corresponds to $1m \times 1m$.

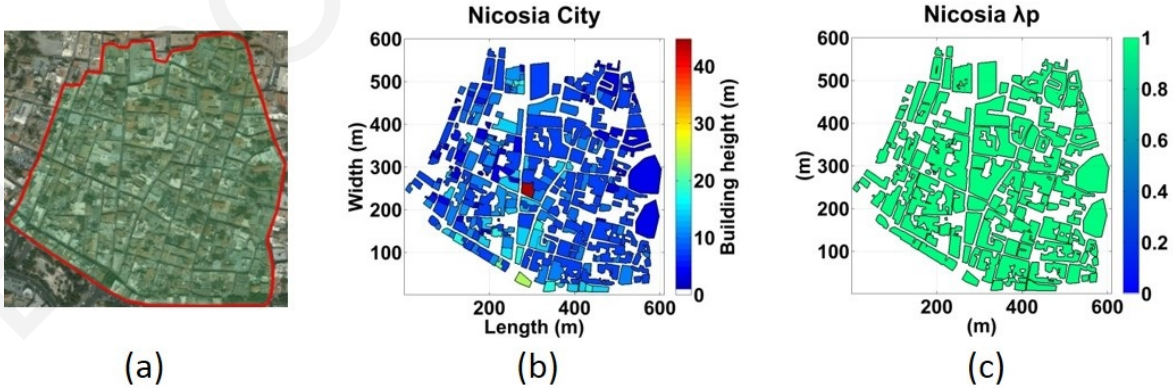

Figure 3.3: Building elevation dataset of Nicosia ($600m \times 610m$). (a) Left side images depict the Google image of study area. (b) Right side images depict the digitized building elevation datasets. Each pixel corresponds to $1m \times 1m$.

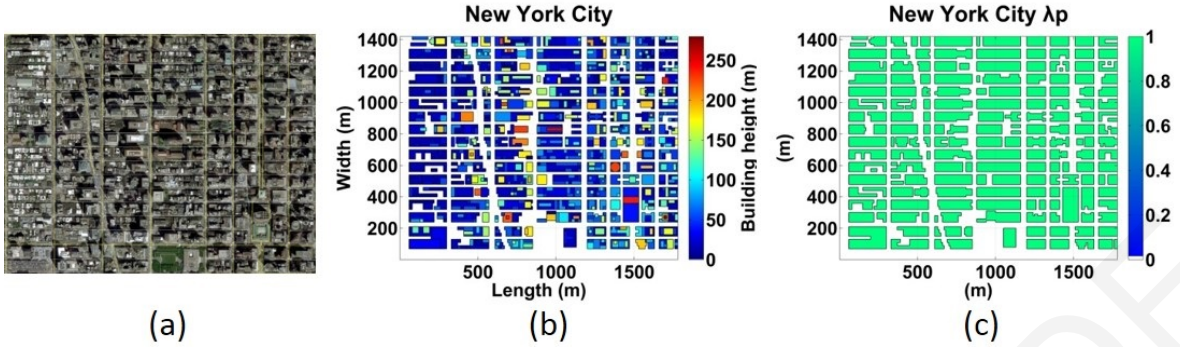

Figure 3.4: Building elevation dataset of New York City ($1420m \times 1780m$). (a) Left side images depict the Google image of study area. (b) Right side images depict the digitized building elevation datasets. Each pixel corresponds to $1m \times 1m$.

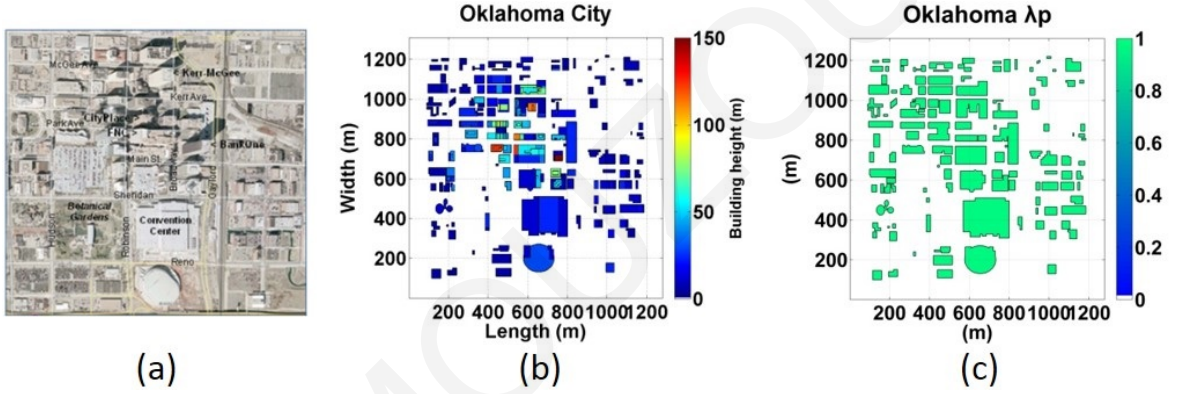

Figure 3.5: Building elevation dataset of Oklahoma ($1310m \times 1280m$). (a) Left side images depict the Google image of study area. (b) Right side images depict the digitized building elevation datasets. Each pixel corresponds to $1m \times 1m$.

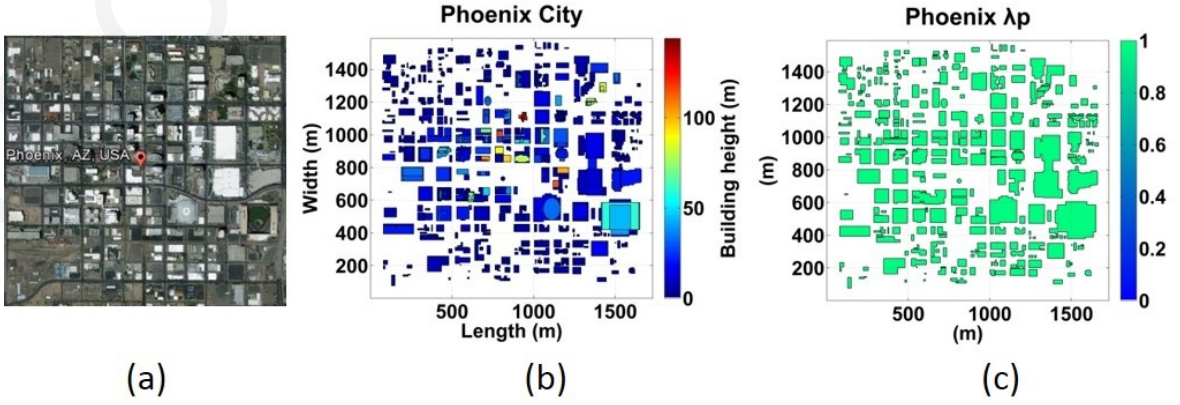

Figure 3.6: Building elevation dataset of Phoenix ($1590m \times 1730m$). (a) Left side images depict the Google image of study area. (b) Right side images depict the digitized building elevation datasets. Each pixel corresponds to $1m \times 1m$.

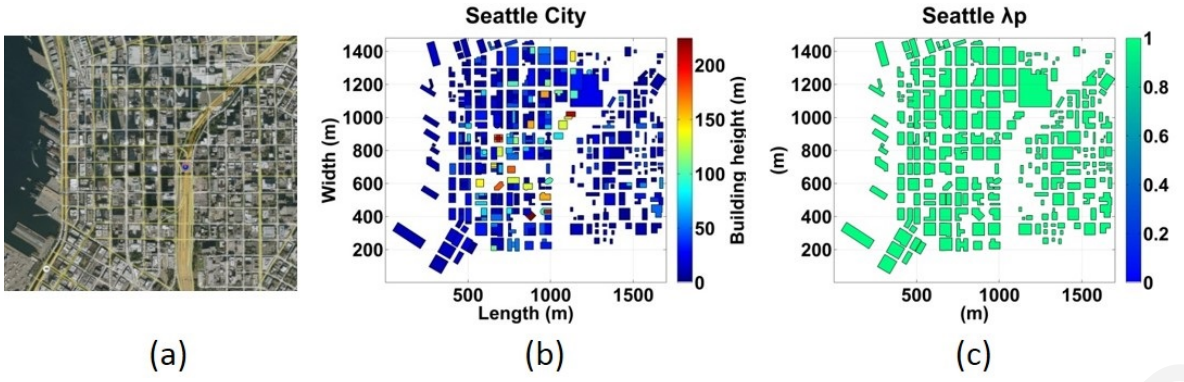

Figure 3.7: Building elevation dataset of Seattle ($1480m \times 1700m$). (a) Left side images depict the Google image of study area. (b) Right side images depict the digitized building elevation datasets. Each pixel corresponds to $1m \times 1m$.

3.2 The dataset for the urban building energy demands

A key challenge in analysing urban-scale energy data is to make sense of large amounts of spatio-temporal data associated with energy consumption in a manner that is useful, tractable, efficient, and flexible for decision-makers. So far, the study of urban-scale energy consumption due to buildings has followed the archetype approach where a few samples of representative buildings within a city are selected and analysed and then the results are extrapolated across the entire city or district [23, 107].

A complete dataset has recently emerged from Tian et al. [107], where a range of information on building geometry used, (building heights, population), and energy consumption for heating and cooling has been available for the London Westminster Borough. In particular, each building within the borough is simulated using a dynamic energy model in order to derive the corresponding hourly consumptions for heating, cooling, and power. The simulation process and the associated outputs are described in Choudhary and Tian [20] and Tian et al. [107]. In summary, high resolution maps are used to create a 3D geometric model of each building within the Westminster borough. The maps give precise information regarding use of the building, its orientation, height, as well as adjacencies with neighbouring buildings (for calculating solar gains).

This information, together with other data sources (energy performance certificate data per building) result in an input model for annual energy simulation at hourly time steps (the simulations are carried out using the energy simulation software *eEnergyPlus* (*v6.0*). The outputs include diurnal variations of energy demand

for typical days in different seasons per building. The results are verified against publically available data provided by UK Department of Energy and Climate Change (DECC). These include hourly heating, cooling and power demand per building.

Fig. 3.8 shows the spatial visualization of the Westminsters Borough data as derived for (i) the building heights across the city, (ii) packing density (λ_p) and (iii) population density. The dataset concerns the central business district (CBD) of Westminster City, with an approximate coverage area size of 6000×7000 m^2 at an initial (highest) resolution of 10m $\times$ 10m per pixel. As noted from Fig. 3.8, the tallest buildings of Westminster Borough are located centrally and eastward, where most of the buildings are designated as offices and retail stores [107]. On the other hand, most of the population is located mainly in the south and northwest areas (Fig. 3.8d).

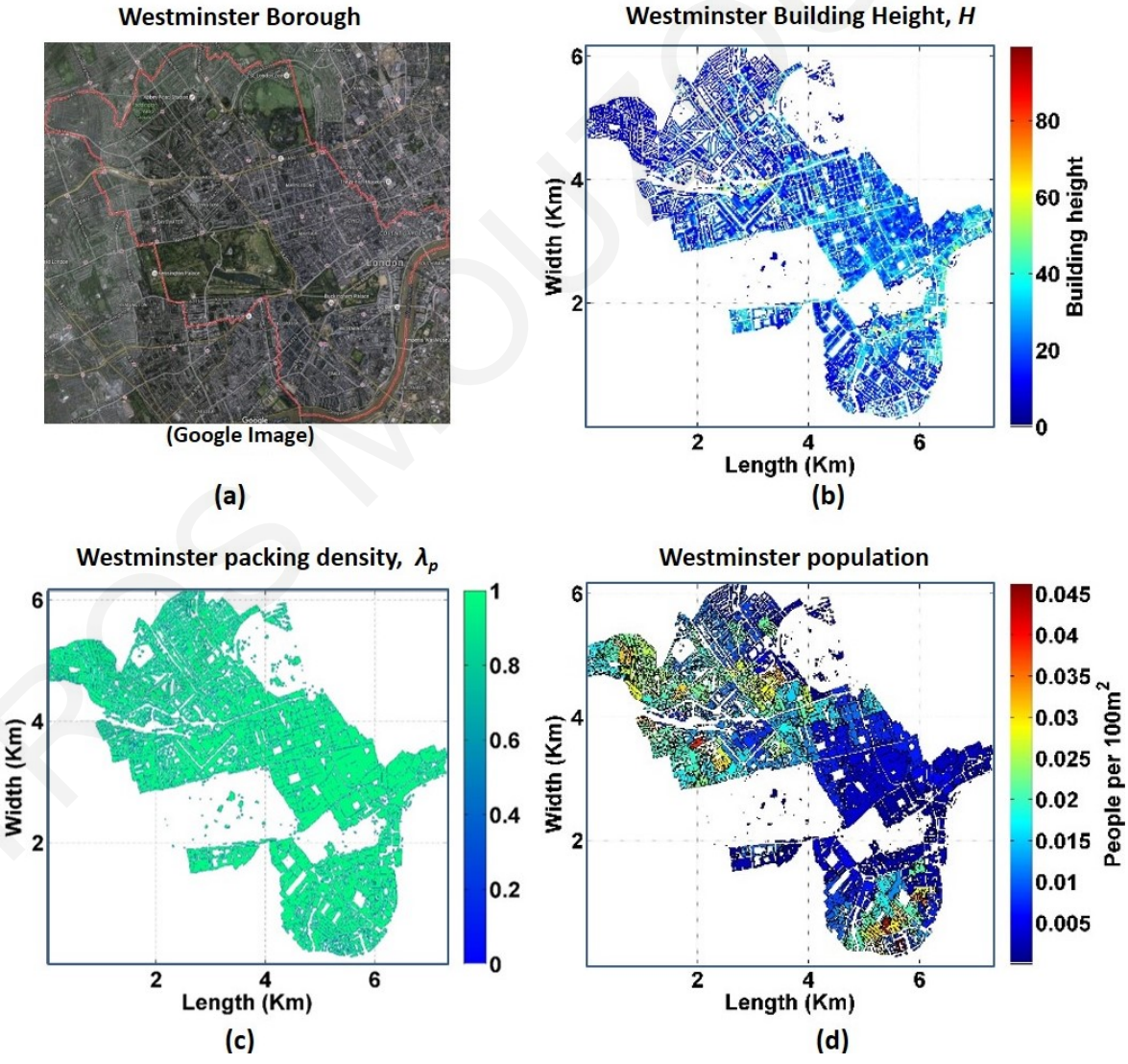

Figure 3.8: Westminster's Borough central business district (CBD) depicted as a Google image/map (a) and as digitized map for building height (b), planar packing density - λ_p (c) and population density (d) of the corresponding area. Each pixel of the dataset corresponds to $10m \times 10m$ of physical area

In Chapter 5, it will be presented how possible associations of building height, packing density (λ_p) and population density with energy demands, can be concluded, taking into account observations that these parameters are expected to have high impact on energy demand (e.g. [20]).

3.3 Atmospheric data in urban scale

In this section, an assessment of long-term measurements of particulate matter (PM) and gaseous pollutants as well as the meteorological conditions in Nicosia is provided, using the data that were collected in the form of time-series, from Air Quality Monitoring Station (AQMS) of University of Cyprus (UCY) over a period of past 69 months. Statistical analysis of the dataset provides the most significant conditions and parameters that affect the air quality in the area.

Table 3.2: Standards and guidelines of the criteria urban air pollutants (CO, NO_2, PM_{10})

Pollutant	Concentration	Averaging period	Legal nature	Permitted exceedences each year	Description
Carbon monoxide (CO)	10 mg/m^3 (11.6 ppm)	Maximum daily 8 hour mean	Limit value entered into force 01/01/2005	n/a	Limit value for the protection of human health
Nitrogen dioxide (NO_2)	200 μg/m^3 (105 ppb)	1 hour	Limit value entered into force 01/01/2010	18	Limit value for the protection of human health
	40μg/m^3 (21 ppb)	1 year	Limit value entered into force 01/01/2010	n/a	Limit value for the protection of human health
	30 μg/m^3 (16 ppb)	1 year	Limit value entered into force 01/01/2010	n/a	Limit value for the protection of vegetation
Particulate Matter (PM_{10})	50 μg/m^3	24 hours	Limit value entered into force 01/01/2005	35	Limit value for the protection of human health
	40 μg/m^3	1 year	Limit value entered into force 01/01/2005	n/a	Limit value for the protection of human health

The impact of air pollution on public health - especially the airborne particulate matter (PM) - has been of major interest during the last years both to the air quality management community and regulatory authorities (Heal et al., 2012; Middleton et

Table 3.3: Natural and anthropogenic sources of criteria pollutants

Compounds	Natural sources	Antropogenic sources	Scales	
			Spatial	Temporal
CO (Carbon Monoxide)	Forest fires Atmospheric oxidation of natural hydrocarbons and methane	Incomplete combustion of fossil fuels and wood Motor vehicles Oxidation of hydrocarbons Industrial processes Blast furnaces	100 Km (Regional Scale)	6-9 months
NOx (Nitrogen oxides)	Forest fires Anaerobic processes in soil Electric storms	Combustion of oil, gas and goal Atmospheric transformation of NO	1 Km (Urban Scale)	1 day
Particulate Matter	Mineral dust Sea salt Volcanic dust Biological debris Sulphates from DMS Sulphates from volcanic SO_2 Organic aerosol from biogenic VOC	Industrial dust Black carbon Organic aerosol Sulphates from SO_2 Nitrates from NOx	10 Km (Meso-scale)	1 year

al., 2008). The European Union Directive on Air Quality 2008/50/EC [25] sets the general legislative framework on assessing the air quality in populated areas (Table 3.2). This legislative framework has also recommended target values for harmful pollutants to public health, environment and the built infrastructure [58]. These pollutants include nitrogen oxides (NO_x), carbon monoxide (CO), PM with diameter of 10 μm or less (PM_{10}) and Sulfur Dioxide (SO_2). The prescribed standard values are intended to protect public health, including the health of "sensitive" populations such as asthmatics, children, and the elderly as well as to protect public welfare, including protection against decreased visibility [44], damage to animal health [87], crops and vegetation [5] and buildings [108].

Air quality in an area is defined by the meteorological conditions and the levels of emissions. The former is known to exhibit strong annual and seasonal variations

modulated by the respective changes of large scale atmospheric circulation [98]. The latter change from year to year, as a result of changes in the intensity of activities that emit pollutants because of socio-economic reasons such as wood burning for heating due to the economic crisis [92]. The sources of pollution are related to traffic, industrial and domestic anthropogenic activities which could be local or elsewhere, whilst sinks are mainly due to chemical reactions or depositions (e.g. dry and wet) (Table 3.3). Usually the concentrations of pollutants due to local sources are those which significantly affect the air quality in an area. However, background concentrations of pollutants in an urban environment play a key role throughout the equilibrium of urban pollution. There are cases where background concentrations are greater than concentrations associated with local sources.

3.3.1 Data acquisition

3.3.1.1 Site description

Continuous monitoring data were collected in the South-East Mediterranean basin in the period from 1st April 2008 to 31st December 2013 using the AQMS of UCY; the station is located at the South East (SE) outskirts of Nicosia city, in the New UCY Campus. The initial location of the station was in the proximity of the UCY Student Halls Campus and next to a busy road with a traffic light at about 250 m away controlling a T-junction (Fig. 3.9). Therefore, the station measurements during that period were considered as urban roadside measurements. On 12th April 2011, the station was relocated 1 km away from the previous location of the station in the North East (NE) direction (Fig. 3.9); it is considered as a rural background location, because the surrounding area is open with agricultural fields and the small road located 30 m in front of the station has very sparse road traffic. Any construction activities taking place during the monitoring period were also noted, since they may affect the air quality of the surrounding area [59]. Such construction and road works were in progress in the UCY New Campus area during 2008.

3.3.1.2 Instrumentation and data collection

All continuous monitoring data were reported on hourly average intervals over the period from 2008 to 2013. This data streaming was performed using WinAQMS and WinCollect softwares (Ecotech 2007). WinAQMS software was also used for

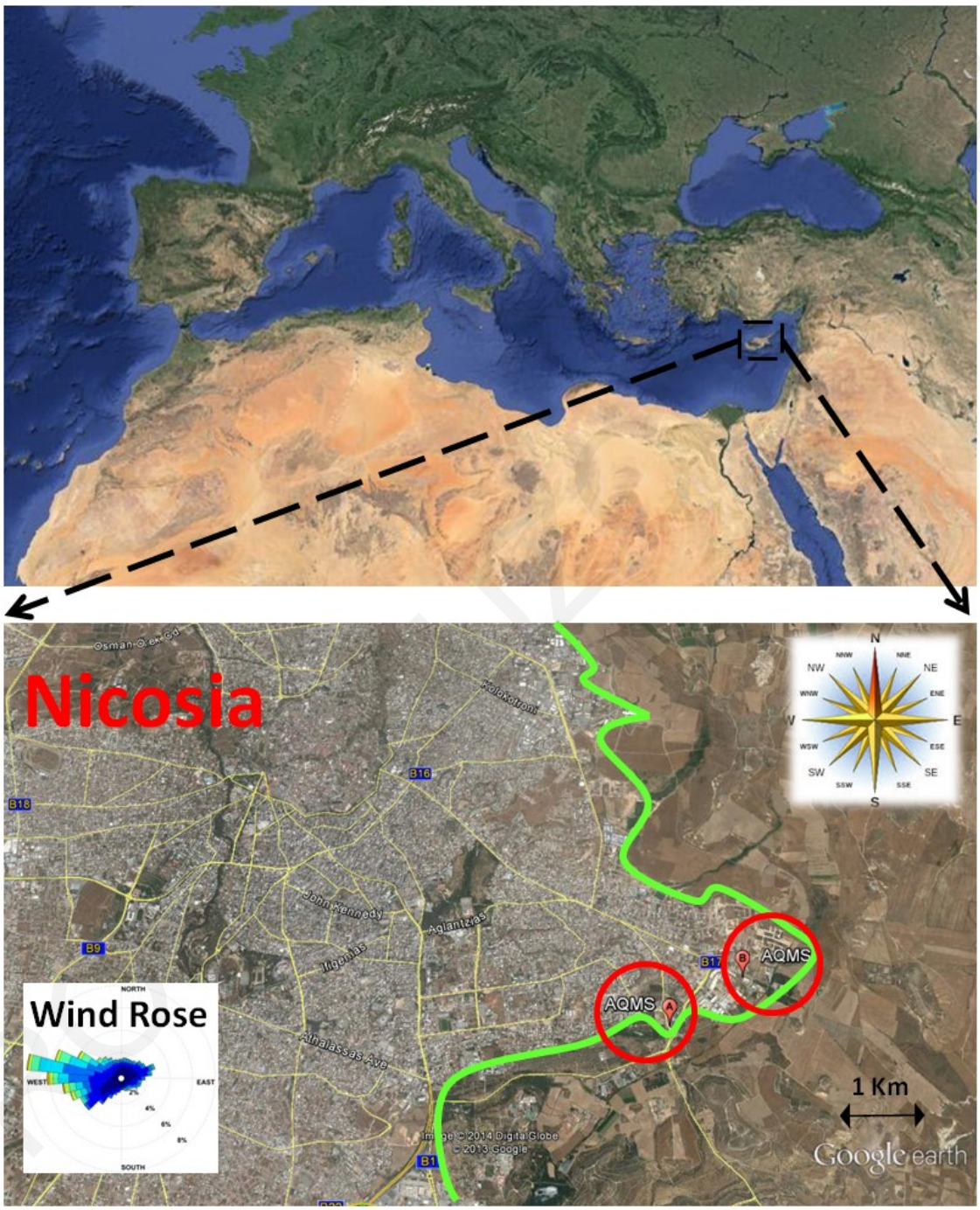

Figure 3.9: Google Earth image depicting the two different locations of the University of Cyprus AQMS in Nicosia, Cyprus. Positions A and B are the initial and new locations of the station, respectively. Wind rose shows the wind directions in the area based on daily averaged values.

calibration, maintenance and monitoring of instruments performance on a weekly-basis during the study period. AQMS station measures meteorological parameters such as wind speed (WS), wind direction (WD), ambient temperature (AT), barometric pressure (BP), relative humidity (RH), rain fall (RF) and solar radiation (SR). Concentration measurements of nitrogen monoxide (NO), nitrogen dioxide (NO_2), nitrogen oxides NO_x (= NO + NO_2), PM_{10} and CO were also taken; the samples for these measurements were at 3 m height above ground level.

A Model48i-analyser and Model 42i (Thermo Fisher Scientific Inc.) were used to carry out measurements of CO and NO_x concentrations respectively. Sampling rate of NO_x and CO analysers is 10 sec, and once the period of 60 min has elapsed, WinAQMS calculates the hourly-average value of NO_x and CO concentration by using the 10 s data values. In a same way, WinAQMS calculates the hourly-average value for all instruments and sensors. Finally an ambient particulate monitor, a Tapered Element Oscillating Microbalance (TEOM; 1400ab; Thermo Fisher Scientific Inc.) was used to measure gravimetrically the PM_{10} levels.

Statistical values of the mean and standard deviation are shown in Table 3.4 and were calculated over the actual collected measurements and not over the entire possible data encapsulated in the time period of observation. Specifically, the measurements contained 40 224, 36 607 and 40 907 samples of NO_x, CO and PM_{10} hourly measurements respectively, which corresponds to 80%, 73% and 81% of possible data over the entire period, respectively. It is also noted that from the above number of records, a total of 34 368 hourly data correspond to simultaneous hourly measurements of NO_x, CO and PM_{10} concentrations. Any missing values that exist in the dataset (i.e. gaps that appear in time series plots) are either because of maintenance or calibration processes on instruments or instruments being out of service due to some failure e.g. a power-cut.

3.3.2 Overall description of atmospheric data

The collected hourly data were analysed using Matlab© [68] and R© statistical software [88]. These data are presented either in the form of a time-series plot or wind rose. The red vertical line in the time series plots marks the time of relocation of the AQMS station from its initial position to its current one in the University Campus. In the present study, the frequency distribution was deduced for the wind speed and

Table 3.4: Statistical analysis of atmospheric and air quality parameters during the period of 1st April 2008 to 31st December 2013. The words Aver and SD stand for the average value and standard deviation, respectively. Note: BP=Barometric pressure; RH=Relative humidity; RF=Rainfall (annual cumulative); AT=Ambient temperature; SR=Solar radiation; WS=Wind speed; WD=Wind direction.

Parameters	Year					
Aver, (SD)	2008	2009	2010	2011	2012	2013
BP (mbar)	1001.0 (12.7)	999.9 (5.2)	998.2 (5.1)	1002.7 (5.6)	1002.1 (6.1)	1005.1 (4.8)
RH (%)	61.7 (20.1)	64.5 (19.9)	63.7 (19.7)	65.3 (18.2)	66.0 (18.9)	59.3 (20.1)
RF (mm)	0 (0.4)	0 (0.4)	0 (0.4)	0.7 (0.4)	0.9 (0.4)	0 (0.4)
AT (^{o}C)	21.6 (7.5)	19.0 (8.1)	20.8 (8.6)	19.6 (8.4)	18.5 (8.6)	21.0 (8.9)
SR (W/m^2)	226.5 (303.7)	202.8 (287.6)	211.3 (295.0)	208.0 (291.7)	205.0 (291.5)	73.57 (151.1)
WS (m/s)	1.7 (1.2)	1.6 (1.2)	1.6 (1.2)	2.2 (1.6)	2.2 (1.6)	2.5 (1.5)
WD (deg)	225.9 (89.0)	223.9 (88.1)	217.8 (86.4)	191.1 (102.4)	189.6 (110.5)	200.8 (110.5)
NO_x (ppb)	15.5 (35.7)	8.5 (13.3)	18.0 (21.0)	13.9 (19.9)	11.1 (13.9)	15.9 (18.0)
CO (ppm)	0.5 (0.4)	2.4 (0.9)	2.0 (0.6)	1.0 (1.4)	1.3 (0.5)	0.5 (0.4)
PM_{10} (μg/m^3)	67.4 (70.6)	31.5 (50.8)	11.5 (22.8)	27.3 (31.9)	30.1 (29.6)	28.6 (20.5)

wind direction data in order to study the dominant-prevailing winds regime and its seasonal variability as well as the levels of pollutant concentrations in Nicosia area.

Fig. 3.10 f-h shows the time series of NO_x, CO and PM_{10} and Table 3.4 summarizes the yearly averaged values (with their corresponding standard deviation) of the three criteria pollutants. The highest annual average values for NO_x were observed during 2010 to be 18.0 ± 21.0 ppb and the lowest values were observed during 2012 to be 11.1 ± 13.9 ppb. Regarding CO measurements, it must be noted that there is a relatively high proportion of missing concentration data in 2008 and in 2013 (25% and 28% respectively) and therefore the year exhibiting the higher or lower CO concentration cannot be concluded confidently. However the year 2010 showed the highest annual average value of CO as 2.0 ± 0.6 ppm. The atmospheric pollution levels reported for other Mediterranean cities [50] provide NO_x concentrations levels to range between 49.9 ± 22.0 and 197.5 ± 14.1 ppb, while CO concentration to be between 1.9 ± 0.6 and 6.2 ± 1.2 ppm. For PM_{10}, the annual average in 2008 was found to be 67.44 ± 70.55 μg/m^3; it is noted that during that year construction works were carried all around in the broader area of the University Campus. The lowest average annual concentration for PM_{10} (11.48 ± 22.80 μg/m^3) was recorded during 2010. Kanakidou et al. [50] reported annual average PM_{10} levels that reached 75.5 ± 27.5 μg/m^3 (for June 1999-May 2000) in Athens PM_{10} on a busy central street. Therefore, comparison of the above results with the results in an urban area in S-E Mediterranean shows

that the air pollution level at the outskirts of Nicosia is moderate.

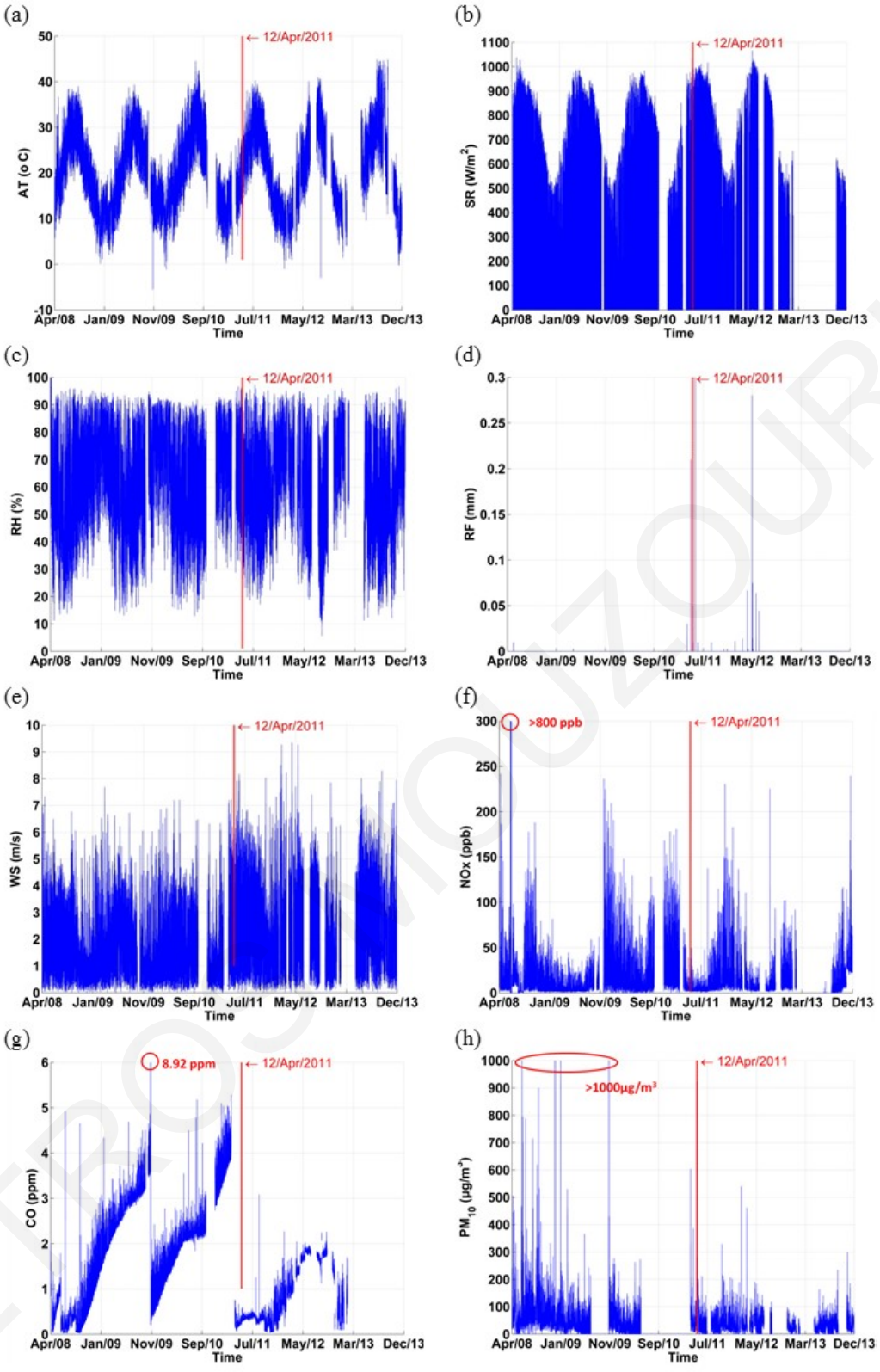

Figure 3.10: The time series data of hourly values over the period extending from 1st April 2008 to 31st December 2013: (a) Ambient Temperature, AT (^{o}C), (b) Solar radiation, SR (W/m^2), (c) Relative humidity, RH (%), (d) Rainfall, RF (*mm*), (e) Wind Speed,WS (m/s), (f) NO_x (ppb), (g) CO (ppm), (h) PM_{10} (μg/m^3). Vertical red line depicts the time of AQMS relocation.

The distribution of wind direction and speed over the whole period of measurements is best represented using the wind rose diagrams. Fig. 3.11 presents the hourly frequency distribution during the measurement period. The frequency distribution function is indicated by the concentric circles and the wind speed frequency distribution for a particular wind sector is given by the radial dimension of the radius. The center of each plot represents a wind speed of zero, which increases radially outwards. This figure indicates that winds in Nicosia exist within the wind sectors of 270.0 ± 22.5 (West; W) and 292.5 ± 22.5 (West to North-West; W-NW) for most of the time. Furthermore, strong winds above 4.0 m/s occur mainly from the same sectors. The overall probability of occurrence of strong winds on these sectors is approximately 6%.

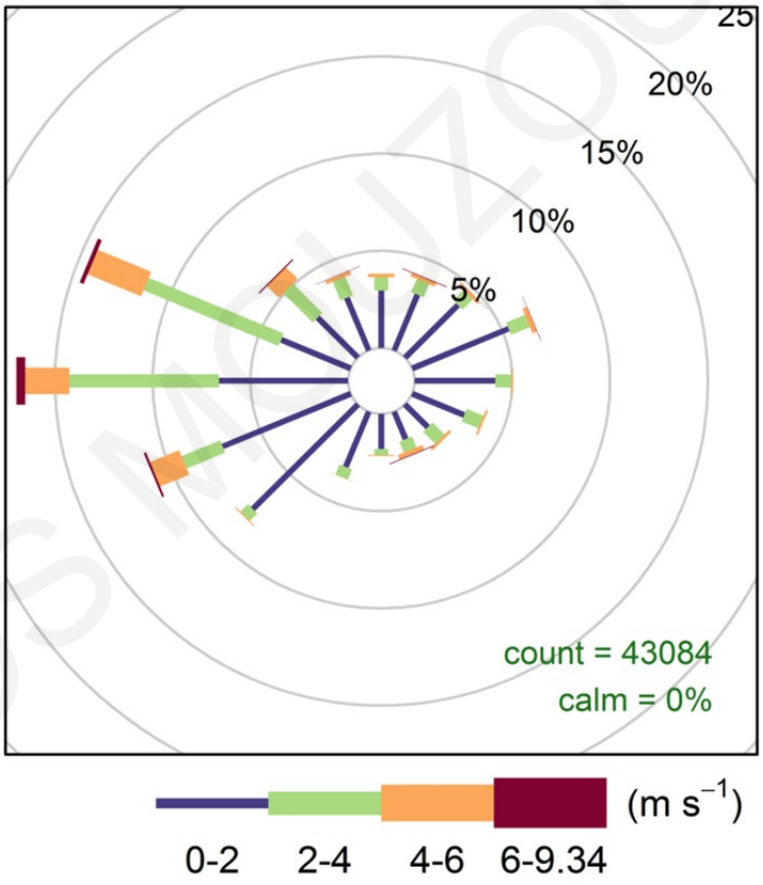

Figure 3.11: Wind rose diagram of the Wind speed (m/s) and Wind Directions (^{o}) over the measurement period extending from 1st April 2008 to 31st December 2013 using hourly data.

The annual wind speed frequency distribution - using hourly average values - is presented in Fig. 3.12. It is observed that W and W-NW wind directions dominate the period of 2008-2013, except in 2011 when West and West to South-West (W-SW) are the predominant wind directions. As shown in Fig. 3.12, during the year of 2012,

winds in North-West (NW) and W-SW directions are also present. The frequency of occurrence of NW and W-SW wind directions in 2012 is 11% and 12%, respectively.

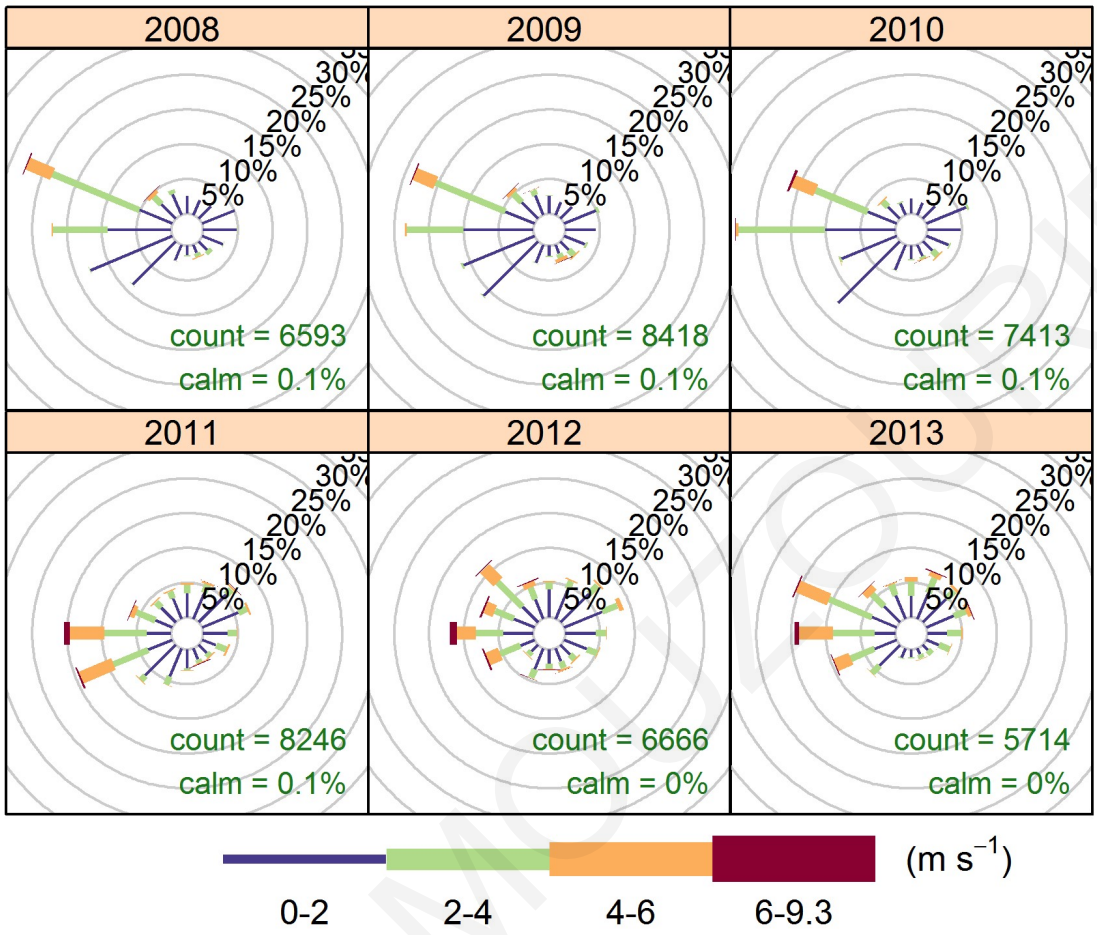

Figure 3.12: Wind rose diagrams depict the hourly frequency distribution from top left to bottom right for 2008, 2009, 2010, 2011, 2012 and 2013.

Table 3.5: Long-term seasonal average values for criteria pollutants NO_x, CO and PM_{10} as well as WS and AT. All data represents a time span of 1st April 2008 to 31st December 2013. The words Aver and SD stand for average value and standard deviation, respectively.

Factor	NO_x (ppb) Aver (SD)	CO (ppm) Aver (SD)	PM_{10} (μg/m^3) Aver (SD)	WS (m/s) Aver (SD)	AT (^{o}C) Aver (SD)
Winter	20.0 (23.4)	1.9 (1.2)	25.3 (42.4)	1.5 (1.3)	10.7 (4.1)
Spring	10.5 (13.3)	1.5 (0.9)	36.9 (41.8)	2.0 (1.5)	18.1 (7.1)
Summer	8.1 (27.0)	1.5 (1.1)	29.4 (42.9)	2.4 (1.5)	28.2 (5.3)
Autumn	13.3 (16.1)	1.4 (1.2)	34.1 (43.3)	1.9 (1.3)	21.2 (6.5)

Table 3.5 presents the seasonal average values of NO_x, CO and PM_{10} over the entired monitored period. The highest seasonal average value for NO_x was observed

to be in the winter season, equal to 19.95 ± 23.36 ppb, while the lowest seasonal average was observed for the summer period and found to be 8.09 ± 26.93 ppb. For the CO concentrations, the highest seasonal average value was found to be for the winter season equalling 1.91 ± 1.18 ppm, while the lowest seasonal average value (1.39 ± 1.24 ppm) was observed during autumn season. On the contrary, the highest concentrations of PM_{10} were measured during the seasons of spring and autumn where the predominant wind directions are from the WN-W sector.

Chapter 4

MRA results on the 2D urban building data

This chapter presents the results from the application of the MRA in the urban building databases; these include three European cities (London, Marseille and Nicosia) and four North-American cities (New York City, Oklahoma, Phoenix and Seattle). The main objective of this analysis is to illustrate how multi-scale representations of an urban area can be obtained rigorously and how a distinctive capability is manifested. Specifically the capability of MRA to reconstruct the original urban "signal" from the decomposed approximations *and* details *enables the urban dataset to hold its signature through the levels.*

4.1 The application of MRA on OKC data

This section illustrates through an example, the application of MRA on an urban building database in order to obtain multi-scale representations of such an urban information. The illustrated example is taken from Oklahoma City (OKC) and a detailed building database and associated statistics of the broader OKC can be found in Burian et al. [10]. The investigated area specifically derives from the Central Business District (CBD) and has an approximate size of 1200×1200 m^2. This urban area is depicted in Fig. 4.1 at a resolution of 1195×1185 pixels, where each pixel corresponds to a 1×1 m^2 area and the colour of each pixel maps the corresponding building height. The accuracy in the mapping of the actual geometries is within

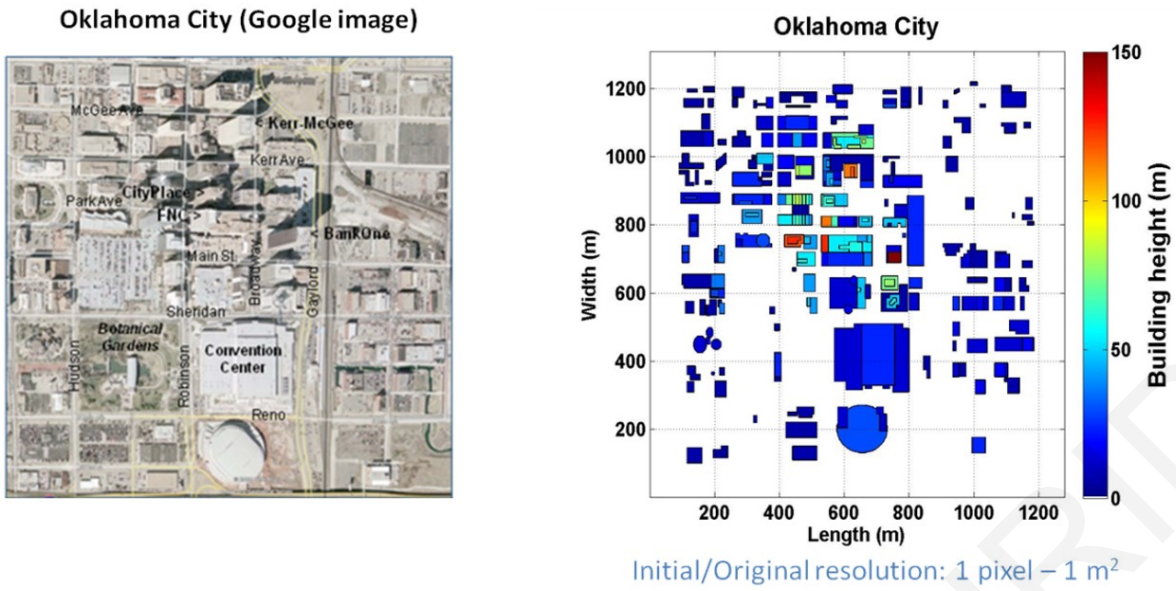

Figure 4.1: The Oklahoma City (OKC) Central Business District (CBD) depicted as Google image - to the left, and as digitized building elevation image - to the right.

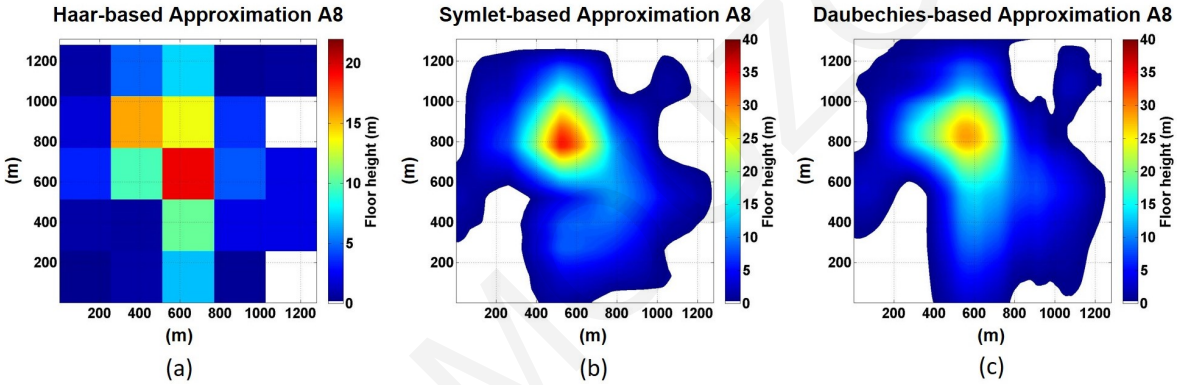

Figure 4.2: Example of MRA results using the *Haar* (left) and *Symlet 4* (right) functions to the OKC-CBD area.

3 m for the vertical direction and within 5 m for the horizontal directions. This urban database information as represented in Fig. 4.1 will be treated as our 2D signal to be analysed using MRA. The MRA was applied to all urban datasets that were described in Chapter 3. The MRA analysis was implemented in Matlab© using its wavelet toolbox. The scaling and wavelet functions that were descriped in Subsection 2.2.3 (i.e *Haar*, *Symlet 4* and *Daubechie 4* functions), were applied to the OKC building database and the results are depicted in Fig. 4.2. All sets of functions identify the sub-area where the city's tallest buildings are located, however the three scaling and wavelet functions give completely different qualitative and quantitative results with regard to the rest of the building information analysis. *Symlet 4* and *Daubechie 4* scaling function, as opposed to the *Haar* function, are not constant

over their support. This means that the approximation values at the scale $2^8 \times 2^8$ corresponding to the *Symlet 4* and *Daubechie 4* analysis are not the same over their support and hence the $2^8 \times 2^8$ cells are not demarcated as in the case of the *Haar* scaling function.

4.1.1 The interpretation of MRA results

At this point, before proceeding to MRA results of all urban datasets, a brief computation of the analysed *approximation* and *detail* components is demonstrated plus some of the theory and the methodology ideas are interpreted. As indicated in Chapter 2, the *approximation* component at the kth level can be decomposed according to Eq. 2.21 into an *approximation* component at the (k+1)th level by removing the vertical (d^V), horizontal (d^H) and diagonal (d^D) detail components. The total detail removed from the *approximation* at the kth level in order to yield the approximation at the (k+1)th level is the summation $\sum_{l=j+1}^{k}(d_l^H(x,y) + d_l^V(x,y) + d_l^D(x,y))$.

It is important to mention that the cells' size in the images of the *approximations* is determined by the size-scale of the support of the scaling function at the corresponding level. Due to this attribute and given that the supports are of scale proportional to 2^j, where j denotes the j^{th} level of MRA, the (largest) highest level of MRA analysis that can be obtained is given by the integer j that generates a scale of 2^j that can be contained in the smallest dimension of the domain; i.e. the smallest integer j close to $\log_2 d$, where d is the smallest dimension of the domain. For example if a domain has dimensions $600m \times 1200m$, the largest level of analysis would be $\log_2 600$, rounding to 9, so the (largest) highest level of analysis of this example is level 9.

Fig. 4.3 demonstrates four (4) out of the ten (10) reconstructed approximations and details obtained from the MRA of the OKC-CBD urban 2D signal, with the single plot at the top of the figure being the digitized image that is analysed. The plots in the two following rows depict the approximation and detail reconstructions of the urban signal at levels 1 and 2 respectively. There are 10 levels overall resulting from MRA since the size and resolution of the original 2D OKC-CBD urban signal allows up to $2^{10} \times 2^{10}$ (1024×1024) m^2 to be covered/completed. The number denoting each level, corresponds to the exponents e.g. 1, 2 of the scales (as area sizes) $2^1 \times 2^1$ and $2^2 \times 2^2$ m^2 respectively, that are used to label the scales. The fourth row (level 8) of Fig. 4.3 illustrates schematically the outcome of the same process at the scale $2^8 \times 2^8$

m^2 .

More specifically, the reconstructed approximation at level 1 in the first row of Fig. 4.3 is obtained by removing the reconstructed details shown in the three remaining plots of the first row entitled *Horizontal Detail 1*-HD_1, (West-East or *x-direction*), *Vertical Detail 1*-VD_1, (North-South or *y-direction*), and *Diagonal Detail 1*, DD_1, from the original, digitized image at the top of the figure. The plot denoted as HD1 depicts the reconstructed detail at level 1 that simulates changes in the vertical direction within the scale $2^1 \times 2^1$ m^2.

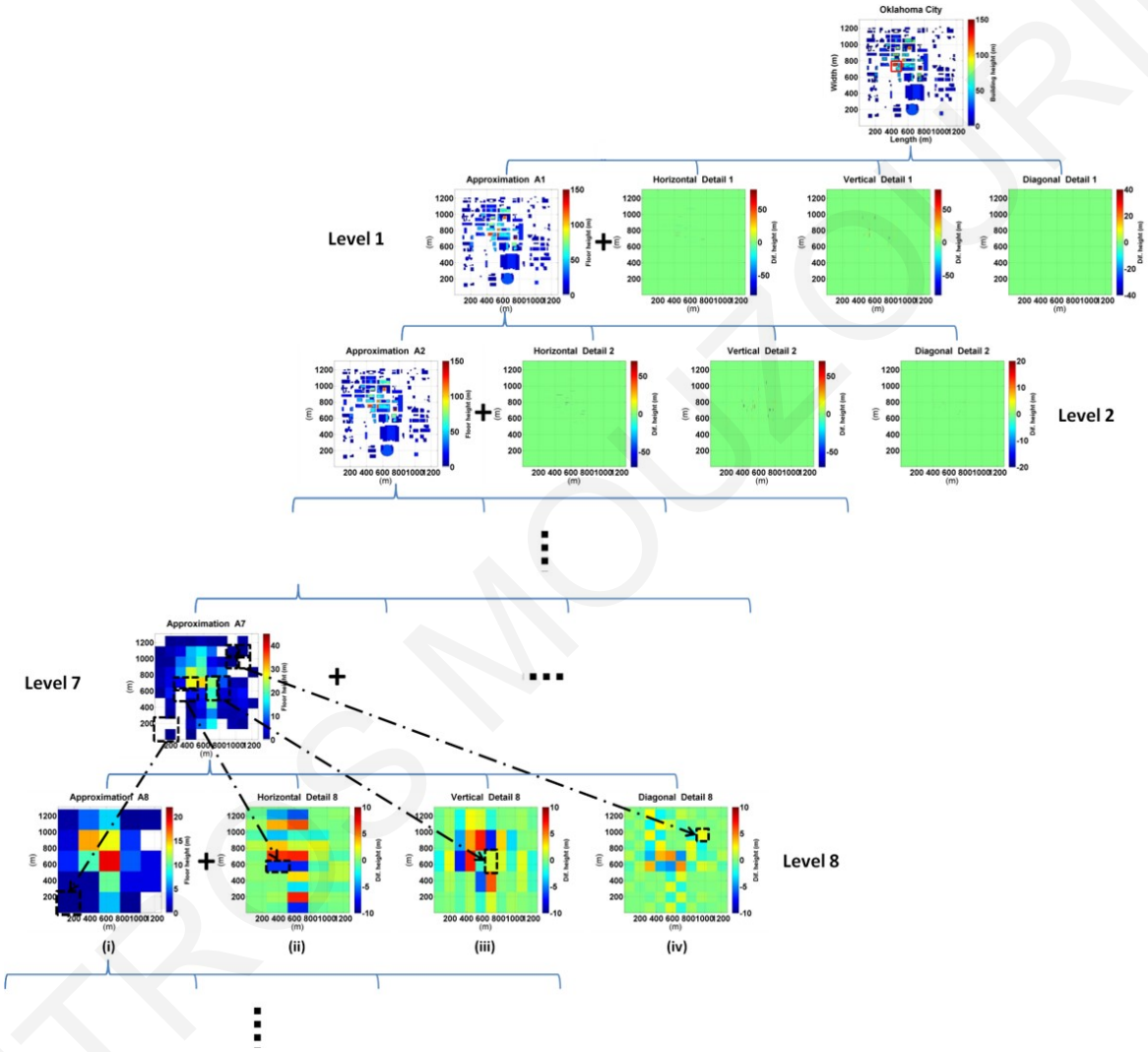

Figure 4.3: Illustrations of the reconstructed approximations and details of the multi-resolution analysis (MRA) of the digitized image of the OKC-CBD at different MRA levels using the *Haar* scaling and wavelet function. The encircled part in red of the digitized image at the top of the figure is presented as zoomed plots in Fig. 4.4

The inner products in Eq. 2.22 measure the variation within the scale $2^1 \times 2^1$ m^2 in the vertical direction, and thereby where these variations are high it appears as high values in the plot HD_1. Changes occurring along the horizontals and diagonals of

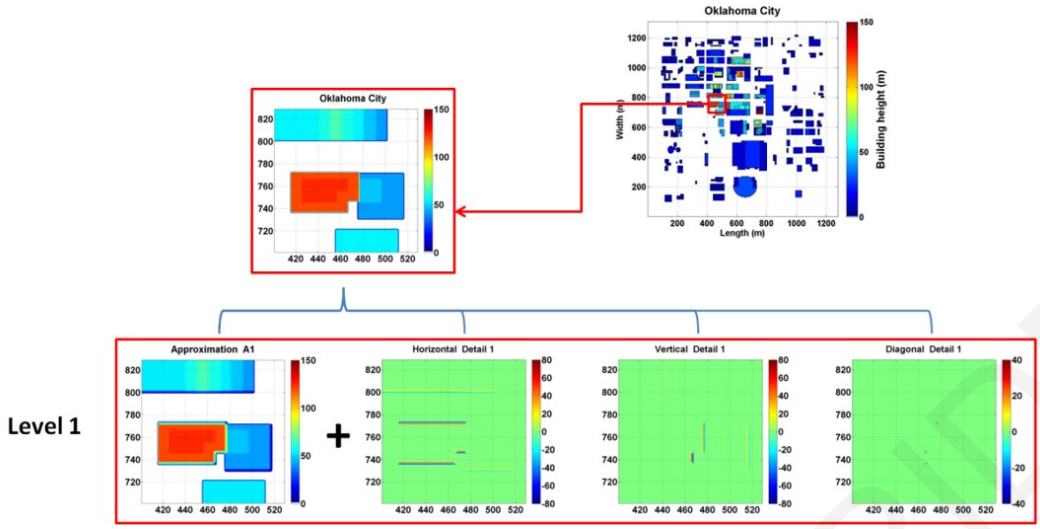

Figure 4.4: Zoomed plots of the reconstructed approximation and details of the multi-resolution analysis (MRA) of the digitized image of the OKC-CBD area at scale $2^1 \times 2^1$ m^2 (level 1) using the *Haar* scaling and wavelet function.

the image at $2^1 \times 2^1$ m^2 are depicted in the plots denoted as VD_1 and DD_1 respectively. What exactly happens in the plots at level 1 becomes clearer if the encircled area, for example appearing in Fig. 4.4 is zoomed and the corresponding results observed. In *Approximation 1*, A1, the edges and corners of the buildings are smoothed, simply because they are adjacent to non-built, empty space. The removed details that cause the edges and corners to smooth out during the approximation process are reconstructed in the detail part as HD_1, VD_1, DD_1 in the same row (level 1).

The value in each cell in the larger scale approximation component is obtained by computing the average of the values of the four (4) cells of the previous scale that were coalesced to create the bigger cell at the higher scale. The details removed during the averaging process are not rejected but retained in the *detail* components at the previous level. As an illustration of the analysis the complete MRA decomposition of OKC-CBD is given in Fig. 4.5. The last column in Fig. 4.5 contains only the total summation of the detail components of each row of the complete decomposition featured in Fig. 4.5. The total details at each level j correspond to the sum $d_j^x + d_j^y + d_j^d$ of Eq. 2.23. The MRA decomposition of each city studied in this thesis is given in Figs. A.1-A.12 in Appendix A. For each MRA result of urban dataset that is shown in Figs. A.1-A.12, the highest level of analysis was determined by the corresponding domain dimension (see Table 3.1). Therefore for the largest multi-resolution representation of urban building morphology, a signal with larger dimensions or finer resolution than $1m \times 1m$ per pixel is required.

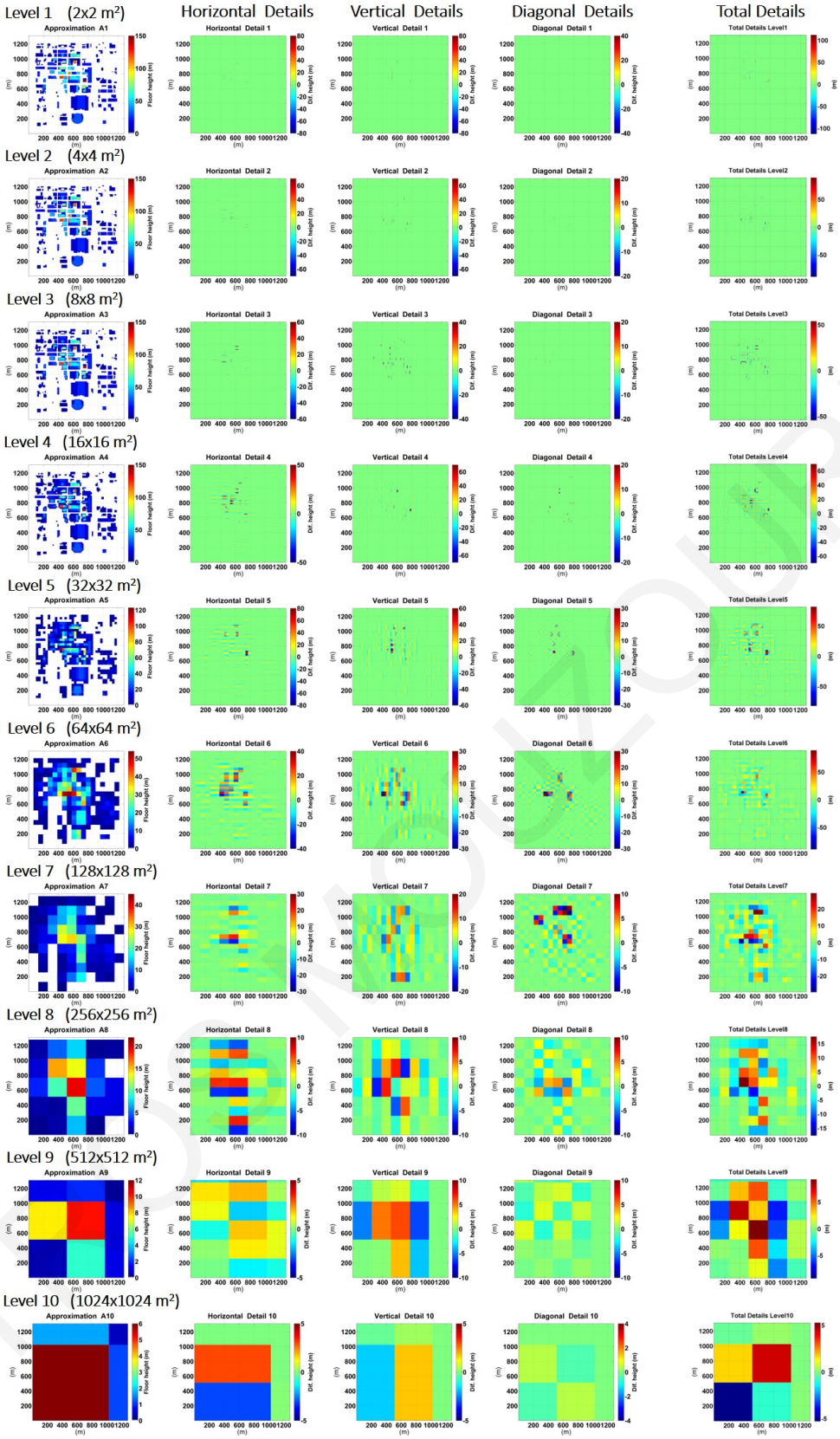

Figure 4.5: MRA results of the 2D urban building database of OKC-CBD. The leftmost column depicts the approximation components at each level that were obtained by removing the horizontal, vertical and diagonal details whose components are shown by the three plots on the right following the approximation in each row. The rightmost image (in each row - Level of MRA) depicts the total details (which is the summation of the horizontal, vertical and diagonal details as per Eq. 2.17).

In order to facilitate the process of reproducing MRA results, the research group by Dr. Neophytou and collaborators has developed a user friendly tool to produce rigorously scale-adaptive and spatially-varying representations of urban information datasets using the MRA method. Scaler© is a tool designed specifically to facilitate basic applications, such as the processing of data in terms of griding, scaling and establishing appropriately scaled model inputs to various modeling systems. *Scaler* tool helps to address the macroscopic feedback of urban canopies into larger scale models. It represents and resolves (grid) data fields (*Approximation*) and sub-grid information (*Details*) at different scales, using the MRA method. Fig. 4.6 illustrates the schematic concept of MRA method. The total length of the developed code is 892 lines.

The main features concerning the usage of *Scaler* tool, are shown in Appendix B

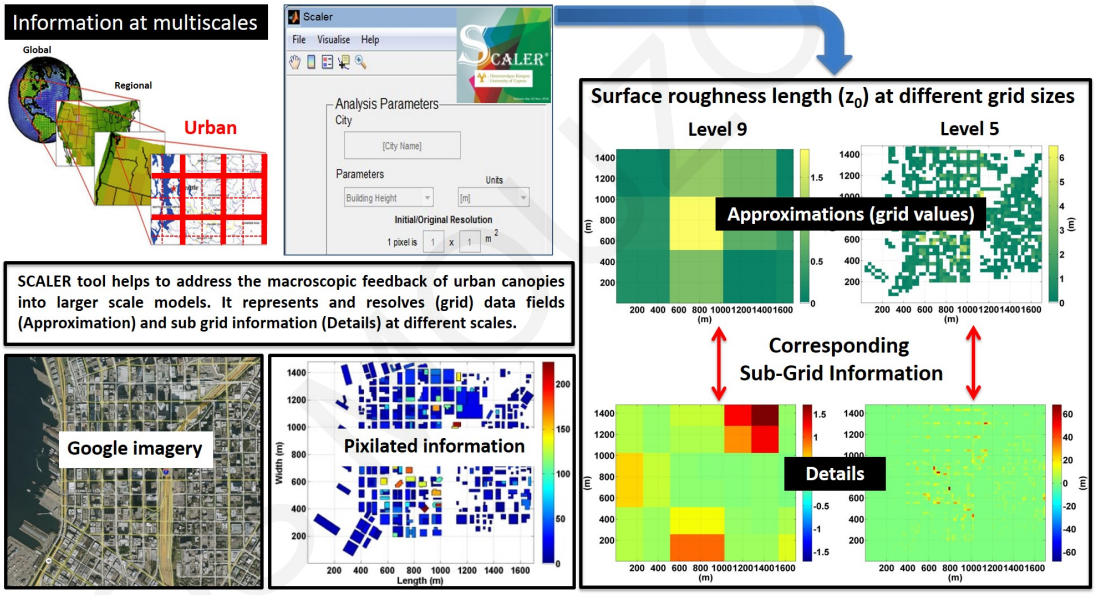

Figure 4.6: An overview of concept schematic of MRA method.

4.2 MRA results of urban building data and their interpretations

The MRA was conducted for all the urban databases addressed in the thesis and a summary of the results from the last three levels of *approximations* of all the featured cities (London, Marseille, Nicosia and New York City, Oklahoma, Phoenix and Seattle) is presented in Figs. 4.7 and 4.14 - both for the urban morphological parameters of $\bar{H}$, λ_p and the aerodynamic parameters. The detailed results containing the *ap-*

proximation and *total details* at each level of the MRA for each of the featured cities in this thesis (London, Marseille, New York, Phoenix, Seattle) are also separately presented for reference in Figs. A.1 to A.12 in Appendix A.

At this point it is important to note that the MRA methodology permits a coherent inter-comparison between the different urban datasets, which can be made at different scales. From the interpretation point of view, it is also noted that in the case of analysing the variability of the urban building height, the numerical value of the *approximation* at each level is the area-weighted built-height average (i.e. an average including the empty, unbuilt space in between the built-up parts of the area), i.e. $H_{app}^{(level)} = \lambda_p \times \bar{H}_{AW}$, and not a statistical mean. It should also be noted that the MRA results of mean building height $\bar{H}$ and planar packing density λ_p that presented in Table 3.1, are calculated over the entire urban study area.

In the cases considered here, North American cities show (based on conventional statistical means listed in Table 1) a smaller λ_p than European cities, except New York City, which has the biggest value λ_p=0.50. In contrast, North American cities have greater building heights (listed in Table 3.1). The MRA analysis provides qualitatively similar results for building heights values for each city, but the quantitative difference which is observed between statistical results and the MRA results stems from the different means of obtaining mean building height. It is also noted that the results which are depicted in Fig. 4.7 are calculated concerning only the cell marked with a value and not the entire study area. For example, the values $H_{app}^{(9)} = 4.30m$ and $\lambda_p^{(9)} = 0.48$ correspond to the Nicosia area with grid dimensions $512m \times 512m$ (Level 9) and not for the entire region with dimensions of $600m \times 610m$. In the MRA deduced results of the average building or built height (the main value of the central *cell* at the higher level of analysis) indicate that for example New York's largest built height $H_{app}^{(10)}$ is 39.76m, while Nicosia has the smallest building height $H_{app}^{(9)}$ equal to $4.30m$. Similarly, the MRA analysis provides quantitative results for λ_p with statistical values of Table 3.1 for each city. MRA deduced results of λ_p (the main value of the central *cell*) indicate that New York is the city with the largest λ_p equal to $\lambda_p^{app(10)}$ = 0.50. In contrast Marseille and Oklahoma are the cities with the smallest λ_p. For a more precise presentation in Fig. 4.7, the actual values of the MRA output results per cell are also featured except for the segmented cells at the edges of the different domains.

As an example of comparative differences between the MRA deduced results

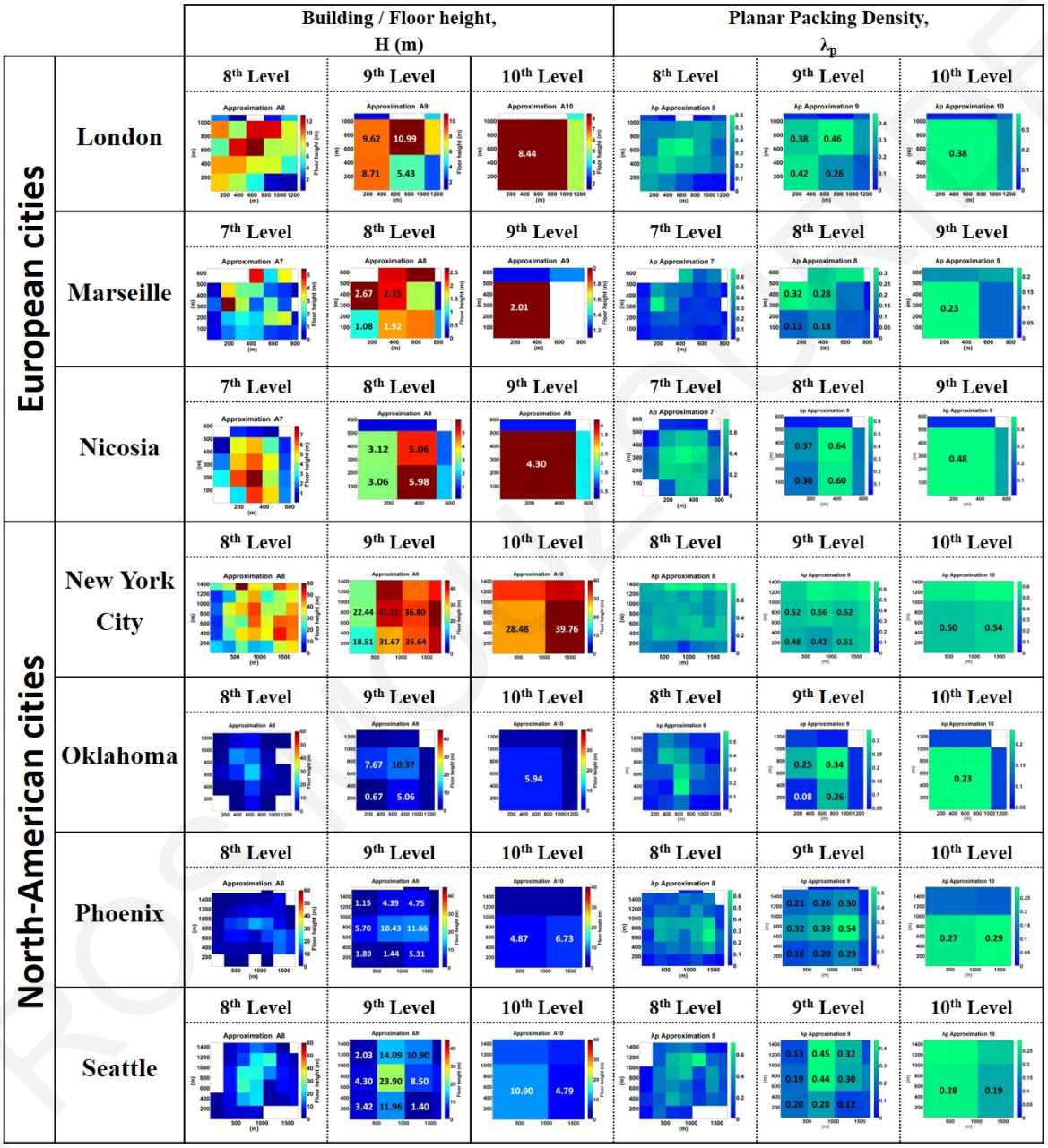

Figure 4.7: The MRA results (for the last three reconstructed approximations) of the building height, H, and the planar packing density, λ_p for European and North-American cities.

with results reported in the literature, Ratti et al. [89] report a value of λ_p of London at the neigborhood scale of 0.55 (for a domain size of $0.2km \times 0.2km$). Comparing the results of London's λ_p in Fig. 4.7 at the nearest scale to that reported in Ratti et al. [89] is that of Level 8, corresponding to cell sizes of $256m \times 256m$ the central cells of the corresponding image, we note that the central cells do have values close to 0.55 but they are surrounded by many cells of much lower values; going to Level 9 *approximation*, we note that there is a higher spatial variation in the λ_p values, resulting at a value at the largest approximation scale (of $1024m \times 1024m$) of 0.38. This example illustrates the scale-dependence of the values of λ_p and the sensitivity of its actual numerical value. Levels 9 and 10 depicted in Fig. 4.7 are the resolutions that currently mesoscale models may be run and therefore the capacity of such a spatially-varying representation or description of urban-morphology parameters is advantageous.

4.2.1 Searching the DNA of a city using MRA

A number of test cases have been constructed and investigated in order to illustrate the capacity and potential of the MRA application in the context of multi-scale numerical weather modelling: (i) in the first, reference case, the MRA of the actual OKC-CBD area is performed; this case is also used as the benchmark case for the comparisons with the subsequent test cases; (ii) a second test case is constructed in order to manifest the influence of different distributions of building height in a specified area with the same statistical urban morphology parameters as those in the benchmark case; and (iii) a third test case is performed in order to illustratethe extent of the influence of a particular building in pre-specified areas.

The specific settings in the test cases are summarized below.

Test case 1 (Benchmark case) This case analyses the actual OKC-CBD area as a digitized signal. This case is considered the reference benchmark case.

Test case 2 (Sibling city) This case investigates a very similar, hypothetically re-constructed OKC-CBD area, where the distribution of heights of the buildings is now changed while the original built plan area of the actual OKC-CBD area is retained. The new resulting values of the statistical parameters, i.e. the average building

height of the area, the area-weighted average building height and the building-height standard deviation, are kept the same (within 1% accuracy) as those of the benchmark case (Test case 1). Specifically, the height of 28 buildings in the OKC-CBD area was changed, corresponding to the 9.7% of the overall 290 buildings. Fig. 4.8 depicts the modified OKC-CBD urban area analysed in Test case 2. The aim behind this investigation is to reveal the MRA capacity of identifying or distinguishing apparently similar urban cases (e.g. with the same building-height averages and building height standard deviations).

Test case 3 In this case the range of impact (or influence) of a building in pre-specified surrounding neighbourhoods of different sizes or scales is investigated. Specifically, this is done by constructing a modified urban area in which the particular building under investigation is removed from the original-reference OKC-CBD urban database. Here one of the tallest buildings was removed. The building whose impact is examined in Test case 3 (and therefore removed from the original database) is the Bank One Building with a mapped height of 150m and a 2250 m^2 plan area; as a consequence of this removal, the resulting average building height is 24.7 m corresponding to a 2.1% change of the original-reference and the resulting standard deviation is 26.4m corresponding to 3.5%. All test cases performed are summarized in Table 4.1.

4.2.1.1 The actual OKC-CBD Area (Test Case 1 - Benchmark)

The results obtained from the application of the MRA to the original OKC-CBD urban dataset (Test case 1 - benchmark) using the *Haar* analysing function are presented in Fig. 4.5; specifically, the resulting approximation and details that the MRA yields at 10 successive levels of the analysis are shown for this urban dataset. At low levels of the MRA (e.g. level 2 or 3) where the size of the averaging cell is still relatively small compared to the urban database information resolution, the obtained approximations, as seen in Fig. 4.5, may not yield discernible differences. However, as the level of analysis increases and the cell size of the averaging (and differencing) process increases, the differences in the distribution of the averaged urban height become more evident. For example, the cell at the OKC-CBD centre, i.e. at the point (600, 600) in (x_1, x_2) coordinates, has a value at the Approximation level 8 of 19.61 m, which is the sum of the values of the cells containing the point in the approximation

at level 9 (i.e. 10.37 m), in the Horizontal, the Vertical as well as the Diagonal Details of the same cell at level 9, i.e. 1.77, 6.17, and 1.31 m respectively. Similarly, at the level 10 for example, the yielded approximation provides an average height of 5.94 m, which corresponds to the average area-weighted building height of that area, taking into consideration the unbuilt-empty spaces. This stratified or structural averaging process leads to an average of the area 1024×1024 m^2, which corresponds to $\lambda_p \bar{H}_{AW}$. In terms of physical interpretation, this value is in agreement with the average building height of the area (22.8 m) and the planar packing density (the built fraction area, 0.22); if an area-weighted average is calculated, taking into account the fraction of the unbuilt area, this yields 5.0 m.

A particular advantage of this "stratified"-structural averaging process is that the removed details are tracked at each level of analysis, and therefore sub-cell information can also be provided. Moreover, the removed horizontal, vertical and diagonal details provide directional differences in the heights of the cells areas and can be possibly associated with other currently used statistical measures in the urban morphology characterization. It is also noted that the different values of approximations obtained at the different levels of MRA are the samples of the urban database at the corresponding scales/grid sizes associated with model resolution (also mentioned in Section 2.2.2).

From the above, MRA is illustrated to be a powerful methodology for multi-scale numerical weather prediction models; it provides gridded and scaled attributes of cities as well as sub-grid information for a hierarchy of scales of such numerical models. Moreover, the ability to track the details at every stage of averaging, and thus scale, enables a unique identification or rather a quantification of the uniqueness of a city. This will be further discussed in the light of the results for the next test case presented below.

4.2.1.2 The sibling OKC-CBD Case (Test case 2)

A hypothetical, sibling OKC-CBD case has been constructed such that the built plan area as well as the average building height and standard deviation of the building heights were the same as the real, reference OKC-CBD, but only the distribution of building heights across the domain was differentiated. Table 4.1 lists the number of buildings that were modified. Fig. 4.8 depicts the modified database as digitized

Table 4.1: Basic urban building morphology statistics for Oklahoma City (OKC) and test cases

	Test case 1 (Reference) Real OKC	Test case 2	Test case 3
Average building height $\bar{H}$ (m)	25.17	25.17	24.65
Standard deviation σ (m)	27.35	27.16	26.38
Area-weighted average building height $\bar{H}_{AW}$ (m)	22.77	22.14	22.27
Planar packing density λ_p	0.221	0.221	0.220
Total number of volumes	290	290	289
Number of changed buildings		28	1
% Change of buildings		9.7	0.3

images to be analysed as well as the associated results obtained from the application of the MRA at all levels. In addition, a zoomed view of the level 8 analysis for both siblings, the real and hypothetical OKC-CBD, is presented in Fig. 4.9 depicting the approximation as well as the horizontal, vertical and diagonal details for both cases; the colour bar scales in the plots were kept the same in both cases to facilitate direct comparison. By direct inspection, it becomes obvious that MRA yields a different multi-resolution representation of the area city with the same $\bar{H}$, λ_p and $\bar{H}_{AW}$. At the level 10 (last) of the analysis (e.g. in Fig. 4.8) where the averaging cell is nearly the entire investigated area, both approximations yield the same average (as one would expect).

However because of this directional differencing that the details provide through their tracking, a distinction between the two cases is made possible through the horizontal, vertical and diagonal details. In fact, the addition of all the details (obtained at each level of analysis) would provide all the subtracted detail from the original urban database in obtaining the (final) approximation, i.e. the overall area-weighted building-height average. In addition, this cell-like or rather matrix-like tracking of the details can be used to assess the impact of the removed details at different resolutions of mapping (visualization), of the city, which in turn can be linked with topological information and therefore dynamics of an urban problem. In contrast, conventional statistics currently used, such as the standard deviation of the building heights, cannot be insightful enough in relation to the dynamics since the spatial variability collapses to a single value. Due to its capacity, MRA

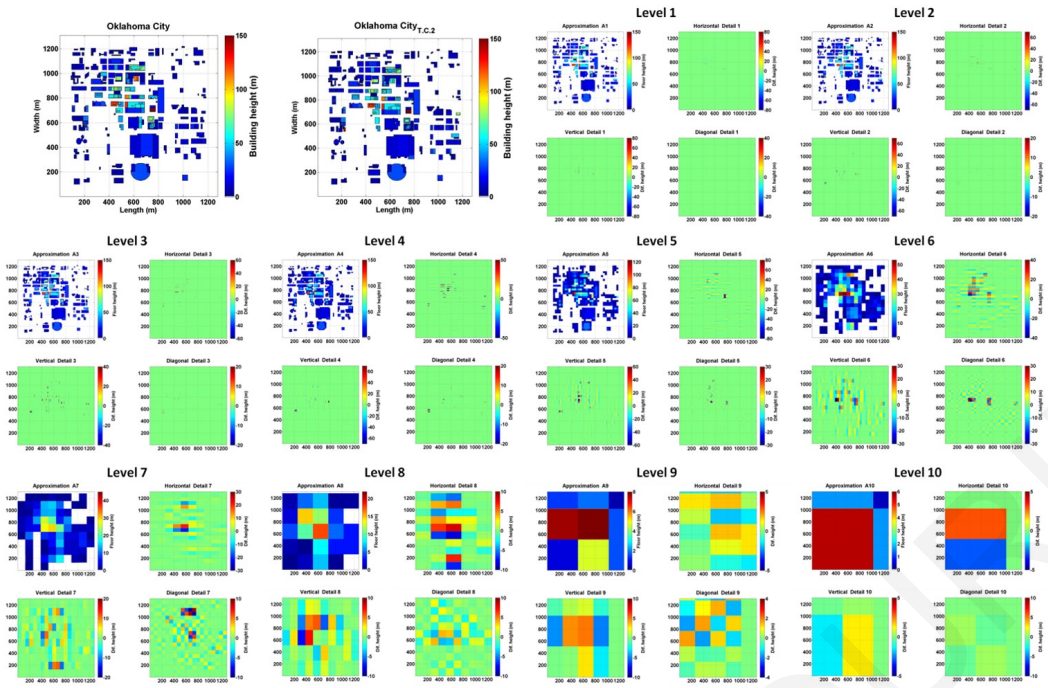

Figure 4.8: The complete MRA results of a slightly modified (hypothetically-reconstructed) OKC-CBD area in which the plan area remains the same but the distribution of the heights of the buildings are modified, such that the new, yielded average building height and the standard deviation of the building height are the same as the original case [hypothetical sibling OKC-CBD area/Test case 2].

encodes the unique information that an urban building database embodies. By having the approximation of the last level and the details of all the MRA levels, we can reconstruct the original urban building database signal.

In addition to the scale-adaptive description of the urban morphology (building height and planar packing density), the boundary-layer aerodynamic parameters have also been derived. As it was shown in Section 3.1, the surface roughness length z_0 can be expressed as a function of the packing density λ_p, or λ_f, and the average building height $\bar{H}$, based on various morphometric and other models. In order to determine z_0 and d, the multi-resolution approximations of the building height and the corresponding λ_p (of area sizes of 250×250 m^2 and above) are used in conjunction with the morphometric model by Kastner-Klein and Rotach (2004).

Using Eqs. 3.6 and 3.7, scale-adaptive values of z_0 and d were obtained at scales of 250 m (that is a representative of a neighbourhood scale) and above using corresponding values of $\bar{H}$ and λ_p at the corresponding levels of MRA, i.e. at cell-sizes of 256×256 m^2, 512×512 m^2 and 1024×1024 m^2 corresponding respectively to levels 8, 9 and 10 of the MRA. Figure 4.10 depicts the scale-adaptive results ofz_0 and d for the cases of the actual Oklahoma City (Test case 1) and the hypothetical sibling

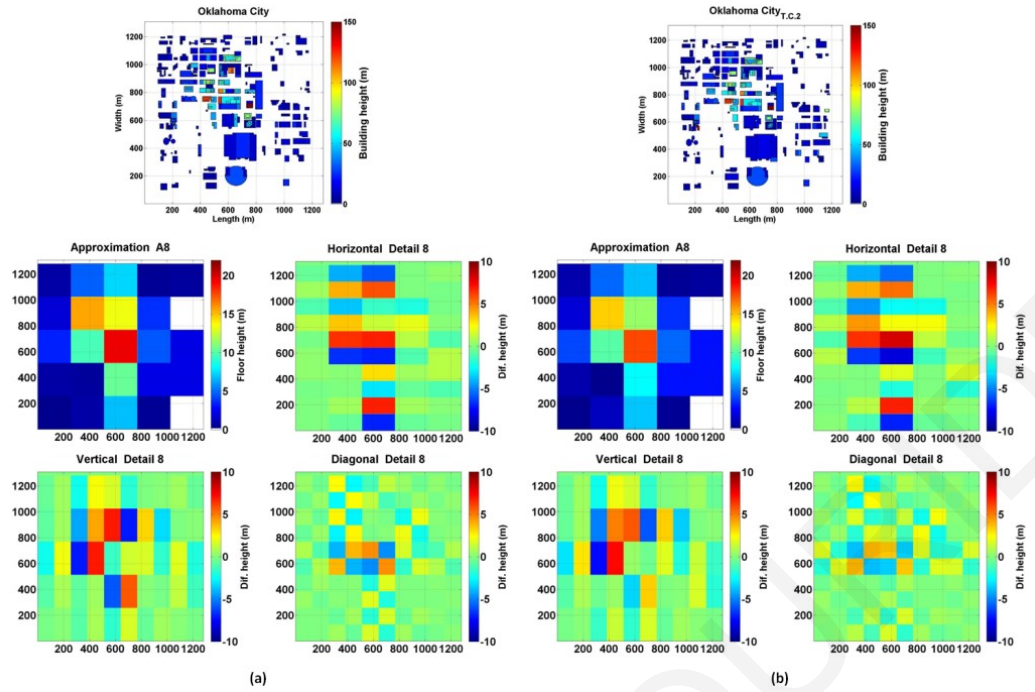

Figure 4.9: Direct comparison between the Reference and Sibling OKC-CBD areas (Test cases 1 and 2) with zoomed plots of the approximation and details obtained at level 8 from the MRA results.

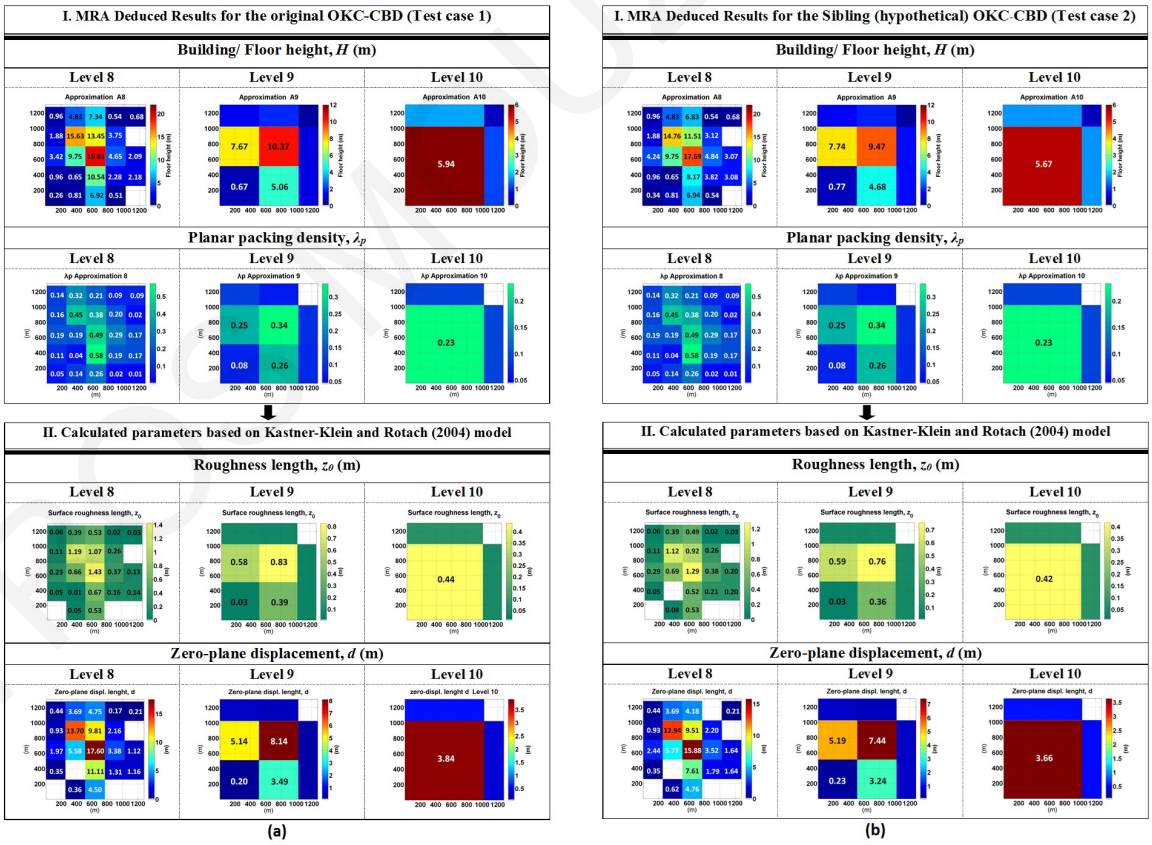

Figure 4.10: The representation of aerodynamic description of OKC-CBD area at a scale higher than 250 m. (I) MRA deduced results; (II) Calculated parameters based on Kastner-Klein and Rotach [52] model. (a) Results refer to original/Benchmark case; (b) Results refer to hypothetical Sibling OKC-CBD area /Test case 2.

Oklahoma City (Test case 2). Although the average building/floor height and packing density over the entire domain (1310×1280 m^2) are the same in both cases, the MRA deduced results depicted in Fig. 4.10 for example, shows the spatial differentiation of the aerodynamic parameters of the two sibling cases enabled exactly because of the structural averaging process.

Such capacity of representation corresponds to potential sub-grid-scale information that can be held in climate models with a coherent scale-adaptive capacity. This also resolves a weakness that has been identified in recent literature in specifying sub-domain areas of variable sizes in a rather arbitrary way in order to derive the corresponding aerodynamic parametrization for boundary-layer flow (e.g. [72]).

4.2.1.3 Some advantages of the MRA results

Test case 3 (OKC-CBD area with removal of the tallest building): Building on the MRA capacity for a unique encoding/representation of a city and scaled attributes of it, this Test case 3 illustrates how the impact of a particular building can be deduced both in the entire domain as well as in different pre-specified sub-domains - e.g. of different sizes. Test case 3 (as listed in Table 4.1) was constructed by removing the tallest building (The Bank One Building) in the actual OKC-CBD area which was examined as the benchmark case (Test case 1). The selected building which is depicted encircled in Fig. 4.11 has a height of 150 m and a plan area of 2250 m^2. The values of the new average building height and the new standard deviation are reduced by 2.0 and 3.5% respectively. This confirms that the final level of analysis yields approximation and details that are consistent with the variation in the conventional average building height: the cell value in the approximation obtained in the last analysis level is 2% smaller than that in Fig. 4.5. Although these observations confirm the expected output of the MRA and its association and consistency with conventional statistical measures, the most attractive feature from the MRA analysis in this case is that the differences observed in the approximations yielded at different levels (or scales) of the MRA reveal and represent the impact of the removed building in the scaled attributes. Fig. 4.12 shows directly for the sake of ease and clarity of observation the difference between the MRA results obtain for the original OKC-CBD domain i.e. including the tallest building (Fig. 4.5) and the MRA results obtained for the same domain but excluding the tallest building. In fact, the

results in Fig. 4.12 show that the removal of the tallest building becomes evident right from the first level of analysis (i.e. the denser resolution) while at higher levels of analysis (coarser resolutions), the impact of the building is manifested differently in different adjacent cells. This capacity enables useful deductions relevant to urban planning deriving from the quantified evaluation of the impact of individual (or complex of) buildings within a domain or sub-domain area. This illustrates in another way how MRA can quantify the uniqueness of an urban database.

In addition to scale-adaptive representations, MRA also allows us to distinguish between urban databases that contain similar information. Fig. 4.13 shows the *approximations* at Level 9, that were reconstructed using the *approximations* and *details* at Level 10, which were obtained for Phoenix and Seattle planar packing density λ_p 2D urban datasets. The DNA-like description arises from the fact that the tracking of the details at each level of the MRA process enables at any point, to obtain/retrieve the very original urban information signal (by adding the *approximation* of a particular, desired level with the *details* discarded at the previous levels). This example, apart from the schematic description of the methodology, highlights the potential of the methodology to distinguish between seemingly similar datasets of urban morphology.

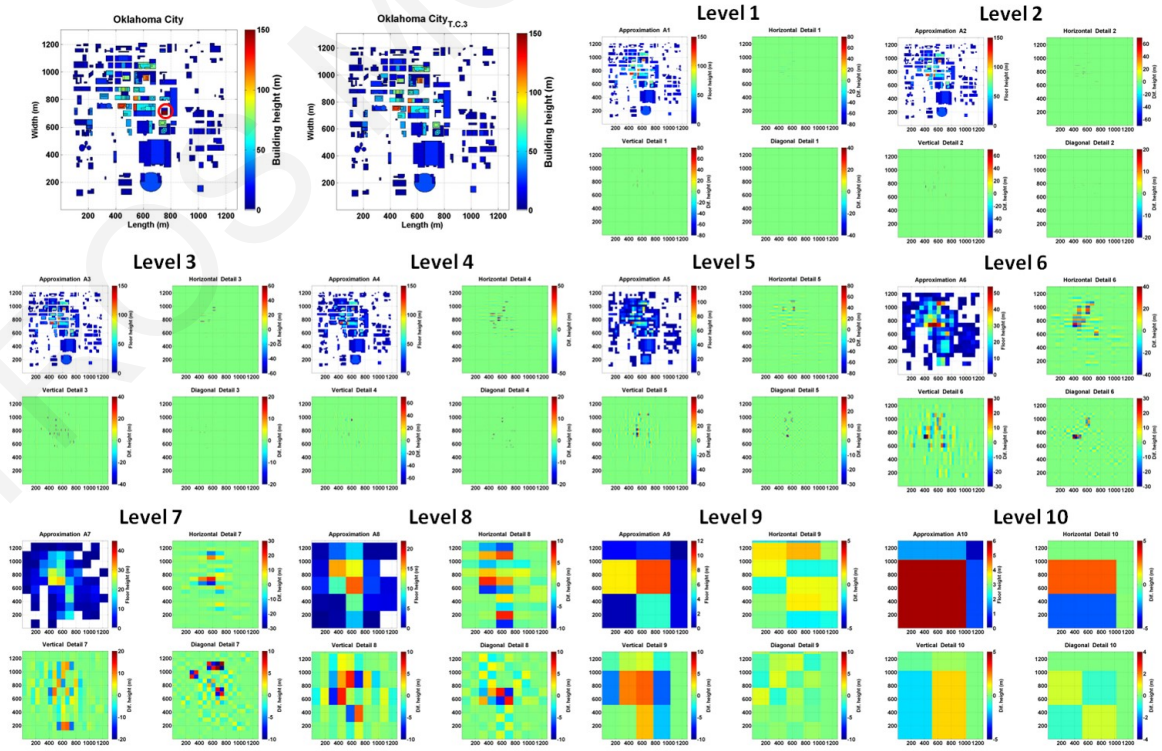

Figure 4.11: The complete MRA results of the original OKC-CBD area with the encircled (in red) tallest building removed [Test case 3].

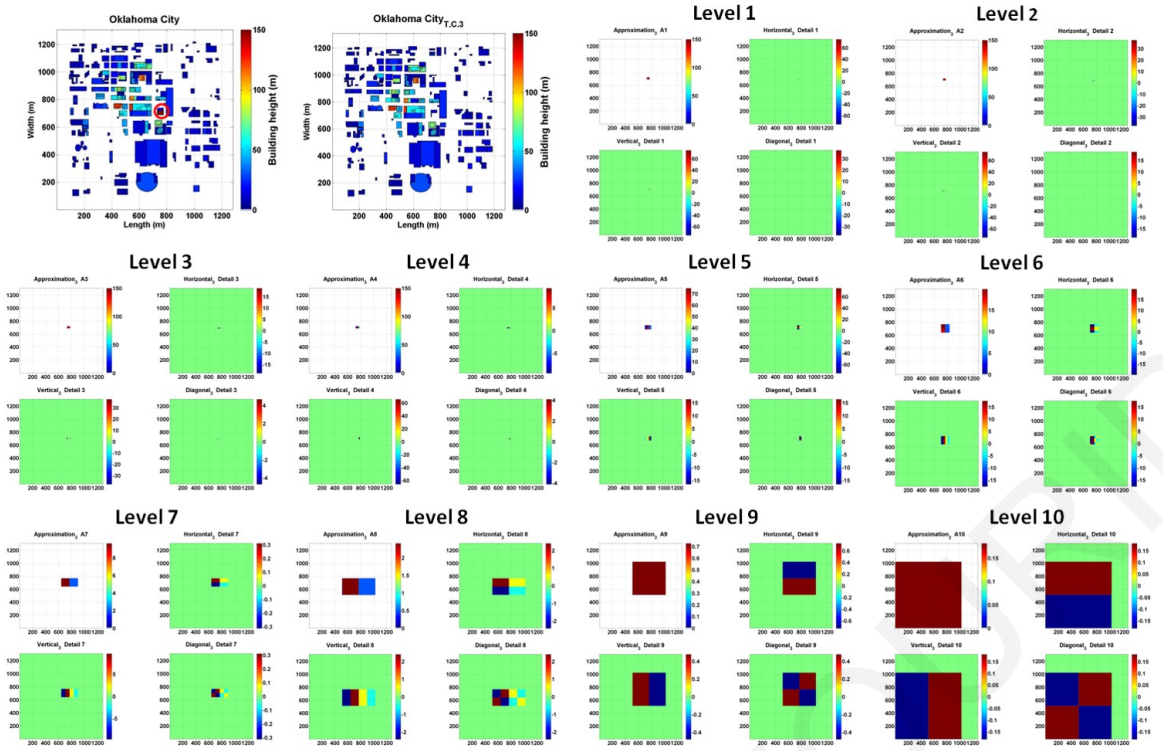

Figure 4.12: The depiction of the impact of the tallest building of OKC-CBD area (in different subdomains at different scales) as a result of the subtraction between the approximations and the details of benchmark case (Test case 1) and the corresponding approximations and the details of Test case 3.

Phoenix and Seattle have the same value of λ_p at Level 10, which corresponds to a cell size of $1024m \times 1024m$. However, at Level 9, the results are entirely different. Respectively, for the case of the city of Seattle, the removal of information, in going from the *approximation* at Level 9 to Level 10, is its corresponding result of total details at Level 10. Therefore, what becomes obvious is that although both cities have the same value of λ_p for the cell size of $1024m \times 1024m$, at level 9 of the analysis entirely different results are obtained for each city. On the other hand, the third column of Fig. 4.13, depicts the total details across all the levels of analysis (according to summation in parentheses of Eq. 2.24) that were removed from the original urban building signal, in order to obtain the λ_p at *approximation* at level 10. Therefore by having the *approximation* of the last level of analysis and the *total details* of all MRA levels, we can recover the original urban building "signal".

Due to this capability of retaining the details removed at each level the MRA can encode the unique information that an urban building database contains. As a result it provides an innovative means to perform rigorous scale-adaptive, spatially-varying descriptions of any urban area while retaining the capability of reconstructing the original dataset, should it be needed in order to get the distinctive signature

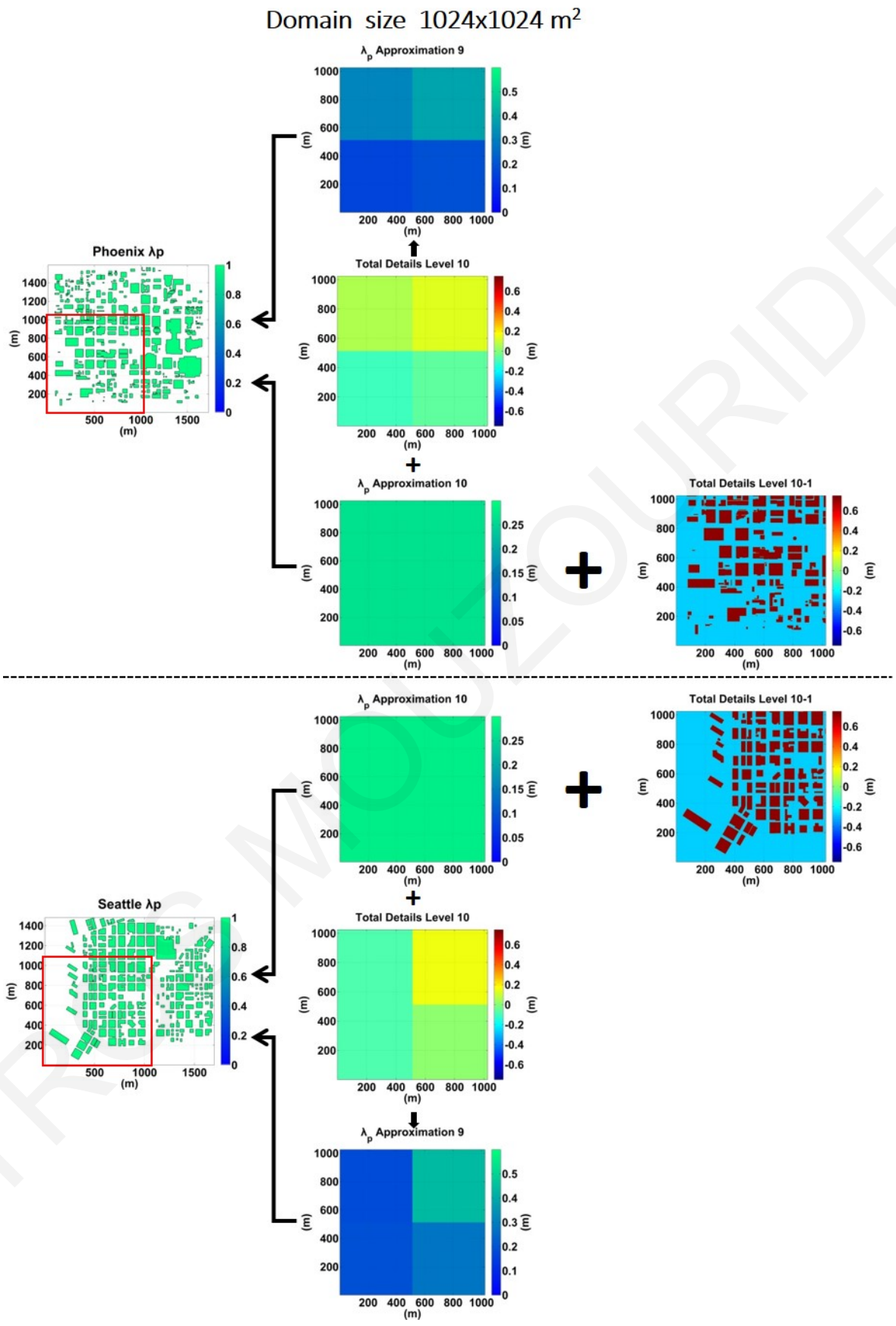

Figure 4.13: Example of the approximations and total details obtained from the MRA analysis of the planar packing density λ_p of the 2D urban building databases of Phoenix and Seattle (corresponding to the domain size of 1024 m × 1024 m) enabling distinction between the two cities despite the identical value of λ_p.

of a city i.e. a DNA-like description.

4.2.2 Derivation of urban aerodynamic parameters using MRA results

A further example of depicting an urban attribute (e.g. a set of UCPs) across different scales and resolutions are the z_0 and the d. The MRA-deduced results for the $\bar{H}$ and λ_p of each city, were used together with the morphometric model by Kastner-Klein and Rotach [52] (Eqs. 3.6-3.7) in order to derive spatially-varying scale-adaptive descriptions of z_0 and d.

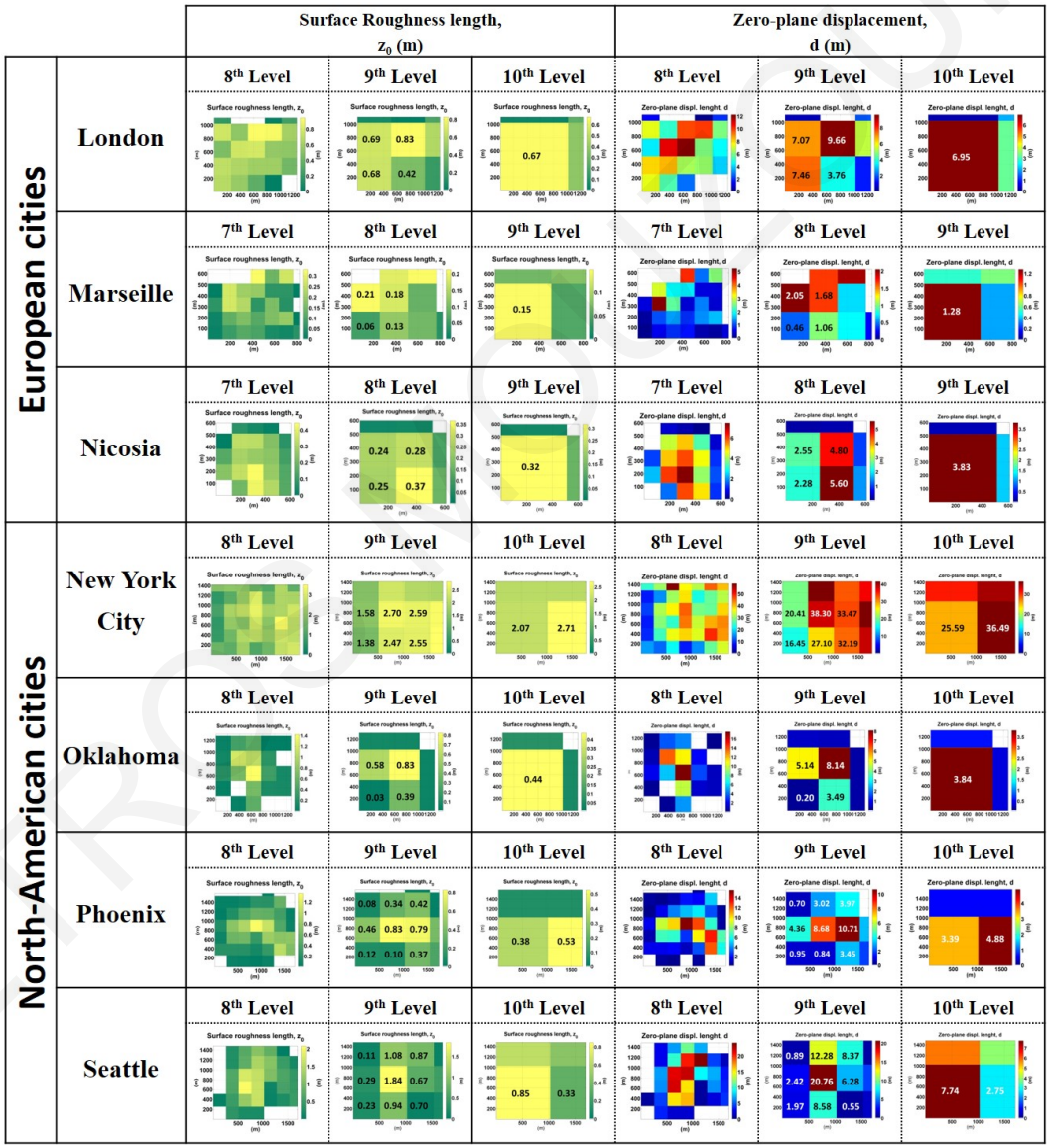

Figure 4.14: MRA-deduced parameters (for the last three levels) of the surface roughness length, z_0, and the zero-plane displacement, d, using the Kastner-Klein and Rotach [52] model for European and North-American cities.

Fig 4.14 depicts the calculated results of the urban morphological parameters of z_0 and d, for the European and North American cities. Therefore, the results show that Phoenix, Seattle and London have similar values of z_0, Marseille has the lowest ($z_0 = 0.15\ m$) and New York the highest ($z_0 = 2.07\ m$, the main value of the central *cell*).

From this analysis and results, the homogeneity or heterogeneity of a city can be quantified and thereby deduced in the three directions - horizontal (x-direction), vertical (y-direction), diagonal and finally the total homogeneity of the domain. In order to illustrate the capacity of MRA to deduce the homogeneity/heterogeneity of a city, MRA *details* of Level 8 of each urban dataset, were normalized with their corresponding statistical mean building height (listed in Table 3.1). Level 8 corresponds to $256m \times 256m$ cell/grid- resolution and was chosen because the length of 250 m can be considered as a representative scale of a neighbourhood while be a minimum length of boundary layer adjustment at this neighbourhood scale.

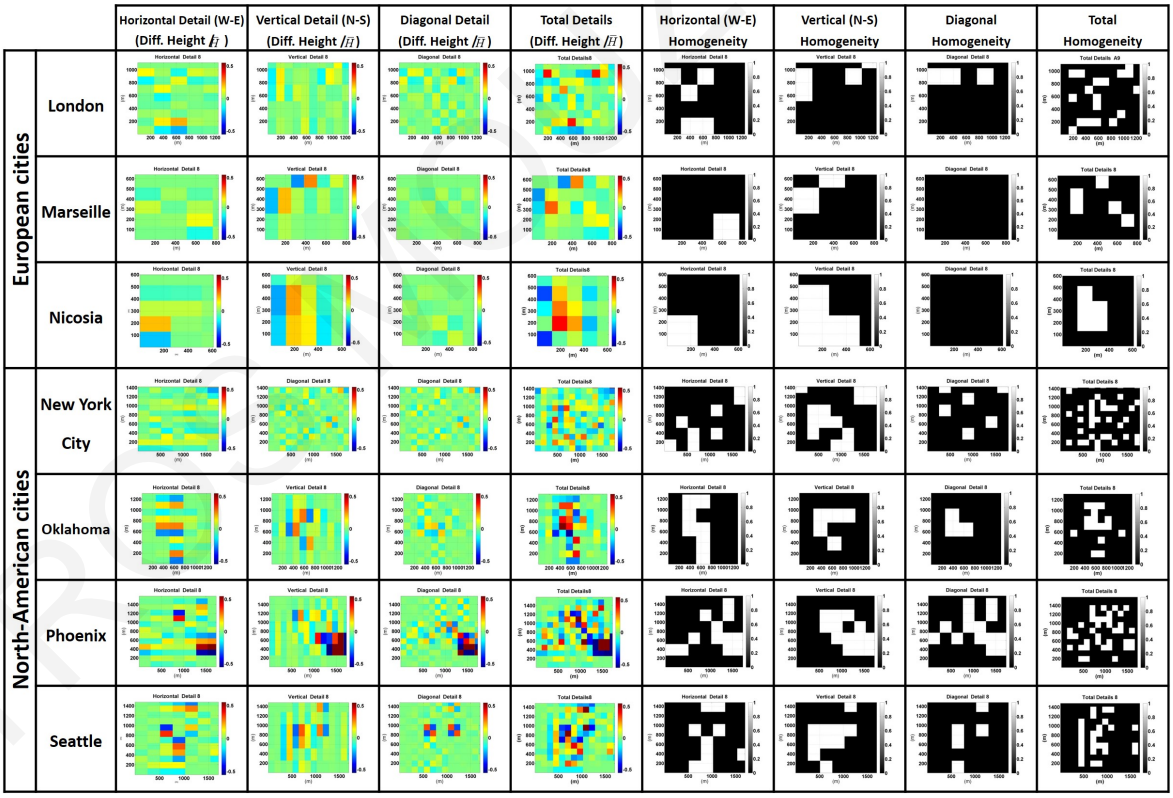

Figure 4.15: MRA results of the horizontal, vertical, diagonal and total details of Level 8 (in color) and their corresponding black-and-white conversion for the homogeneity description of the building height, H.

As a first attempt to classify systematically the homogeneity of a city, it was set that regions/cells in coloured images of Fig. 4.15, with (normalized) values smaller than

0.1 (the floor height of each cell normalized over the statistical mean building height is smaller than 0.1) can be characterized as a homogeneous regions and depicted as black cells, while regions with values bigger than 0.1 can be characterized as a heterogeneous regions and depicted as white cells. The choice of this threshold of 0.1 is arbitrary, however a generic methodology is proposed to characterize and visualize the homogeneity/heterogeneity of a city at the neighbourhood scale.

Comparing the results for *Total Homogeneity* in Fig. 4.15 across the different cities shows, for example, that the featured North-American cities have a spatial spread of heterogeneity across the urban domain, while the featured European cities seem to concentrate the heterogeneity at larger patches and in specific parts of the urban domain. Moreover, the above proposed method of characterizing the homogeneity of the city yields different patterns of homogeneity. For example, by comparing the results of the cities of New York and Nicosia, it was found that the percentage of black cells (homogeneous regions) per total area of each city is the same and equal to 78%, but the pattern of homogeneity is completely different.

Directional homogeneity can also be identified in the neighbourhoods; for example, Nicosia has mainly vertical heterogeneity, while Phoenix and Settle have horizontal (x-direction) and vertical (y-direction) heterogeneity which means that these cities have abrupt changes in the heights of buildings occur along the horizontal x-axis and vertical y-axis of domain. On the other hand New York City, is the most heterogeneous city since it is the city with the largest abrupt changes in the building heights in all directions.

4.3 MRA results of urban building energy demands and their interpretations

The main feature of the MRA is that it is scale-flexible and thus scale-adaptive, allowing thereby identification of appropriate spatial resolution at which data of a given quantity of interest can be presented. Indeed, MRA has been successfully used so far for its scale-adaptive and spatially-varying characterization capacity in the atmospheric urban boundary layer characterization and parametrization. This Section illustrates the application of MRA analysis on energy consumption data and discusses its use in urban energy management and planning. The urban-building

and energy-demand datasets of the London Westminster Borough, derived from Tian et al [107], were used.

4.3.1 Visualization and insights into the urban energy data through the MRA analysis

In this sub-section, the results obtained using the MRA on the urban data of the CBD-London Westminster City Borough are first presented; this presentation is also a means of visualization of the various scale-adaptive representations of the urban information. The representations of MRA results shown in Fig. 4.16 depict the scale-adaptive representation of daily average of heating demands (kWh/100m^2) of a typical winter weekend day for London Westminster Borough. There are 9 levels overall resulting from MRA since the size and resolution of the original 2D urban signal allows up to $(2^9 \times 10) \times (2^9 \times 10)$ to be covered completely. The label denoting each level corresponds to the exponents (e.g. 1, 2, 3) of the scales given in a power of two format (as area sizes). The size of each cell in the relevant level of approximation is listed in brackets for each scale. In the following paragraphs it will be explained why this kind of representations can provide useful information.

At this point it should be noted that the numerical values of the cells in the approximation components should be considered as densities, i.e. quantity per surface area of the cell at the corresponding approximation level. For example, to interpret the results of Fig. 4.16, the encircled "Approximation" and "Total Detail" results at Level 7 will be used. The encircled "cell" at approximation of Level 7 denotes that the mean heating energy demand per 100 m^2 in the corresponding region of Westminster Borough, is 1.72 kWh/100m^2. This outcome may seem very low compared to the original values of the datasets. This is due to the averaging process (see Section 4.1.1) which takes into account also any unbuilt area within the considered region and such unbuilt area does not have any energy demand. In the case that one is interested in the overall energy demand of the encircled area, then this mean value should be multiplied by the area of the corresponding region, i.e. 1.72 [kWh/100m^2] $\times(2^7 \times 10) \times (2^7 \times 10)$ = 28.18 MWh. The mean total energy demand per area - for an urban region - for different scales and different zones/regions can be similarly estimated.

The four cells encircled in the figure showing Total Details of Level 7 denote the

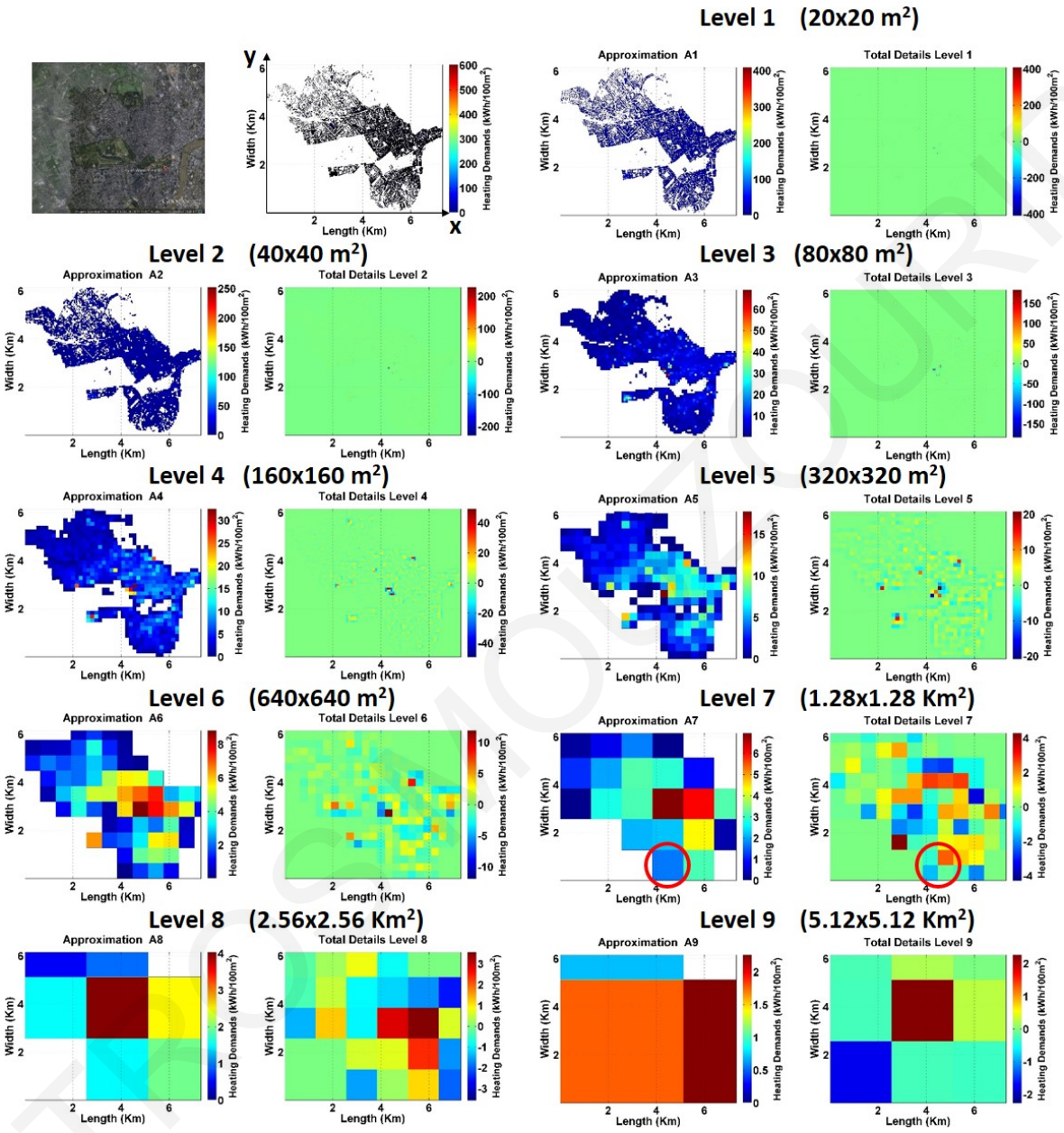

Figure 4.16: The scale-adaptive representations and associated sub-grid information as obtained through MRA analysis for the average daily Heating Demands (kWh/100m^2) for a typical winter weekend day.

summation of the details (in all three directions horizontal, vertical and diagonal) removed from the previous approximation of Level 6 in order to provide the approximation of Level 7. Positive values of Total Details at Level 7 imply that the mean energy demand of the small cell in approximation of Level 6 is lower than the mean value of the corresponding cell that encloses it at approximation of Level 7; whereas negative values imply the opposite. If the values of total details in a region are close to zero, it is implied that the parameter is homogeneous across its lower level.

By using MRA, spatial-area-based visualization of the energy data is possible. It can allow rapid comparisons across neighborhoods within a district - both in terms of energy demand, as well as influencing features such as building heights, packing densities, breathability, etc. This visualization approach is fundamentally more efficient than collecting individual properties on a building-by-building basis and aggregating them over pre-allocated neighborhoods. Furthermore, MRA naturally enables peak-hour identification and localization of best-neighboring candidate zone area for extra energy supply in case of power failures. There are few urban energy models that allow attributes at high-resolution to be explored easily and flexibility across neighborhoods within a district and this represents a key barrier to their usefulness in practice. In this initial proof-of-concept study, full-day (24-hr) evolutions are analysed using urban-scale energy demands for heating and cooling on typical weekends and week days over different seasons.

4.3.1.1 Homogeneity in energy demands within neighbourhoods

The ability of MRA to implement multi-scale sampling, without discarding the redundant details from the corresponding smaller scales at each Level, can be exploited to identify the energy demand homogeneity in a given region/zone. Using Fig. 4.16 as example, it is recalled that approximation Level 6 (cell size 640×640 m^2) was obtained by subtracting from approximation Level 5 (cell size is 320×320 m^2) the corresponding difference called Total Details 6 in the image of cell size 320×320 m^2. The results of Total Details determine which *neighbourhoods* in an urban area have large (or small) and positive (or negative) energy differences from their surrounding *neighbourhoods*. Fig. 4.17 shows Total Details for three different levels of approximation.

As described in Section 4.3.1, net values at Total Details figures imply the homo-

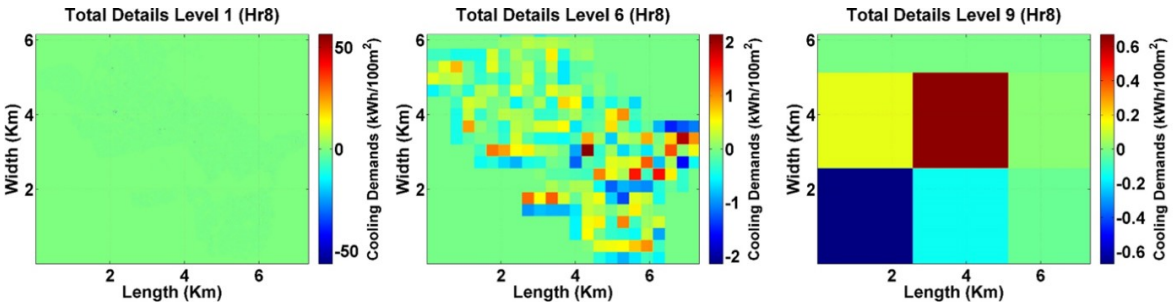

Figure 4.17: A snapshot (at 0800 hours) from the accompanied movie showing the visualization of the diurnal time evolution of the MRA results obtained for the energy-demand differences from their surrounding *neighbourhoods* at the Approximation Levels (a) 1 (left), (b) 6 (middle) and (c) 9 (right). [Please watch the full accompanied video denoted as Fig. 4.17].

geneity of the energy demand across the total area, where positive values denote lower approximation energy demand at the small cell at lower approximation level compare to the corresponding cell that encloses it at higher approximation level; whereas negative values denote the opposite. Thereby according to Fig. 4.17, there are no differences across neighbourhoods in Level 1 because the difference with a lower Level is very close to zero. Level 6 clearly shows a higher difference (from Level 5) towards eastern part of Westminster - which is also the area with a large number of smaller and more varied buildings. These variations are smoothed when one moves across to Level 9.

4.3.2 Identification of spatial and temporal evolution of energy demands

This sub-section presents the scale-adaptive ability of MRA method to represent energy demands exhibiting spatial and temporal variation. In addition, it examines the results obtained from different analysing functions against their ability to identify peak energy demand both in terms of location and time during the day.

4.3.2.1 Time evolution of energy demands with respect to spatial scale of neighbourhoods

The aim of the analysis is to shift our vision regarding the daily energy demand variation from the building scale- to the neighbourhood scale of variable size. Fig. 4.18 (movie) shows the daily evolution of heating demand during winter (Fig. 4.18a) and cooling demand during summer (Fig. 4.18b) in the Westminster Borough at three

Table 4.2: Identification of peak hours of heating and cooling demands for typical days over different seasons

	Heating		Cooling	
	WeekEnd	WeekDay	WeekEnd	WeekDay
Winter	0500	0500	1300	1300
Spring	0600	0600	1200	1400
Summer	0400	0400	1200	1300
Autumn	0500	0500	1400	1200

different scales; at a relatively small scale (size 20 m $\times$ 20 m), a medium scale (size 640 m $\times$ 640 m) and the largest scale (of size 5.12 km $\times$ 5.12 km). At each different scale the timing of peak energy demands for cooling and heating across the entire domain was identified. The MRA results show that the peak hour of energy demand over the total area and during a typical day is independent of the Approximation Level or scale (see Table 4.2). What is varying across the spatial scales is the numerical value of the energy demand at the corresponding region/zone. These results verify the ability of MRA to correctly capture the energy demand data: Indeed, as described in Tian et al. [107], the energy simulations of buildings that yielded this dataset do not consider variations in operational schedules across similar types of buildings. For example, all office buildings follow the same occupancy patterns and are subjected to the same outdoor weather conditions. However, the simulations take into account features such as geometry, orientation, and thermal properties uniquely per building. One would therefore expect no variations in peak energy demand across spatial scales, as neighbourhoods within the Westminster borough tend to be dominated by a uniform building type. Some variations are possible and attributable to the presence of different types of buildings within a particular scale. The numerical value of energy demand, on the other hand, is expected to vary depending on the physical features of buildings within a scale.

A similar analysis was conducted for all the seasons of the year, for both the heating and the cooling demands; Table 4.2 summarizes the peak hour of heating and cooling demands observed over the different seasons of a year for typical weekdays and weekend days.

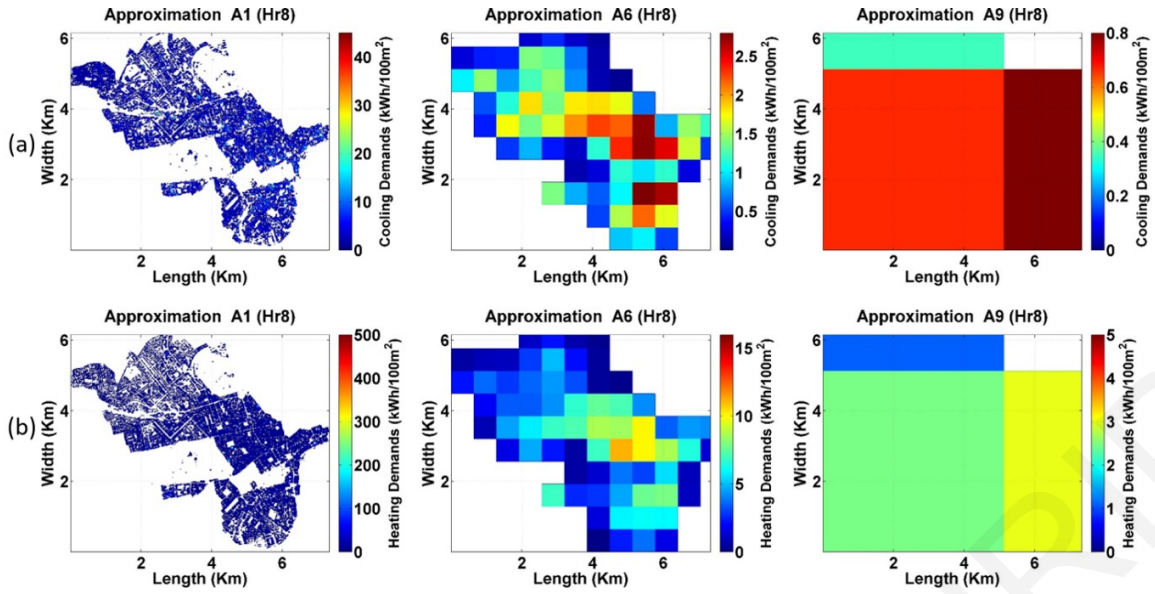

Figure 4.18: A snapshot (at 0800 hours) from the accompanied movie showing the diurnal time evolution of (a) the cooling and (b) the heating demands of a typical summer and winter day. [Please watch the full accompanied video denoted as Fig. 4.18].

4.3.2.2 Identification of the locations of peak energy demands

The aim of this study is to investigate the ability of the MRA analysis to correctly identify peak energy demands across different scale-adaptive representations. The movies in 4.19 present the heating energy demand density (kWh/100m^2) during a typical winter day in London Westminster borough using the three different scaling functions: *Haar*, *Symlet 4* and *Daubechie 4* functions, also referred to in Section 4.1.

The results from the MRA analysis using the *Haar* scaling function yield quantitative values that are consistent with the conventional average value of energy demand in every individual cell (at a given resolution), thus smoothening any patterns of variation within. *Symlet 4* and *Daubechie 4* functions exhibit a different behaviour and are used to detect sudden occurrences appearing across neighbouring cells. For example, by using the*Symlet 4* scaling function and depending on the resolution level of analysis, the local areas exhibiting the peak values of heating/cooling demands can be identified more precisely.

Fig. 4.19 summarises these results: At approximation Level 6 (left column of Fig.4.19), the peak demand identified by *Symlet 4* (middle row) and *Daubechie 4* (bottom row) is very similar. However, the results are different at approximation Level 9 (i.e. at enlarged *neighborhood*, of size corresponding to 5.12 km), albeit in the same corner of the region. These differences, at approximation Level 9, are due

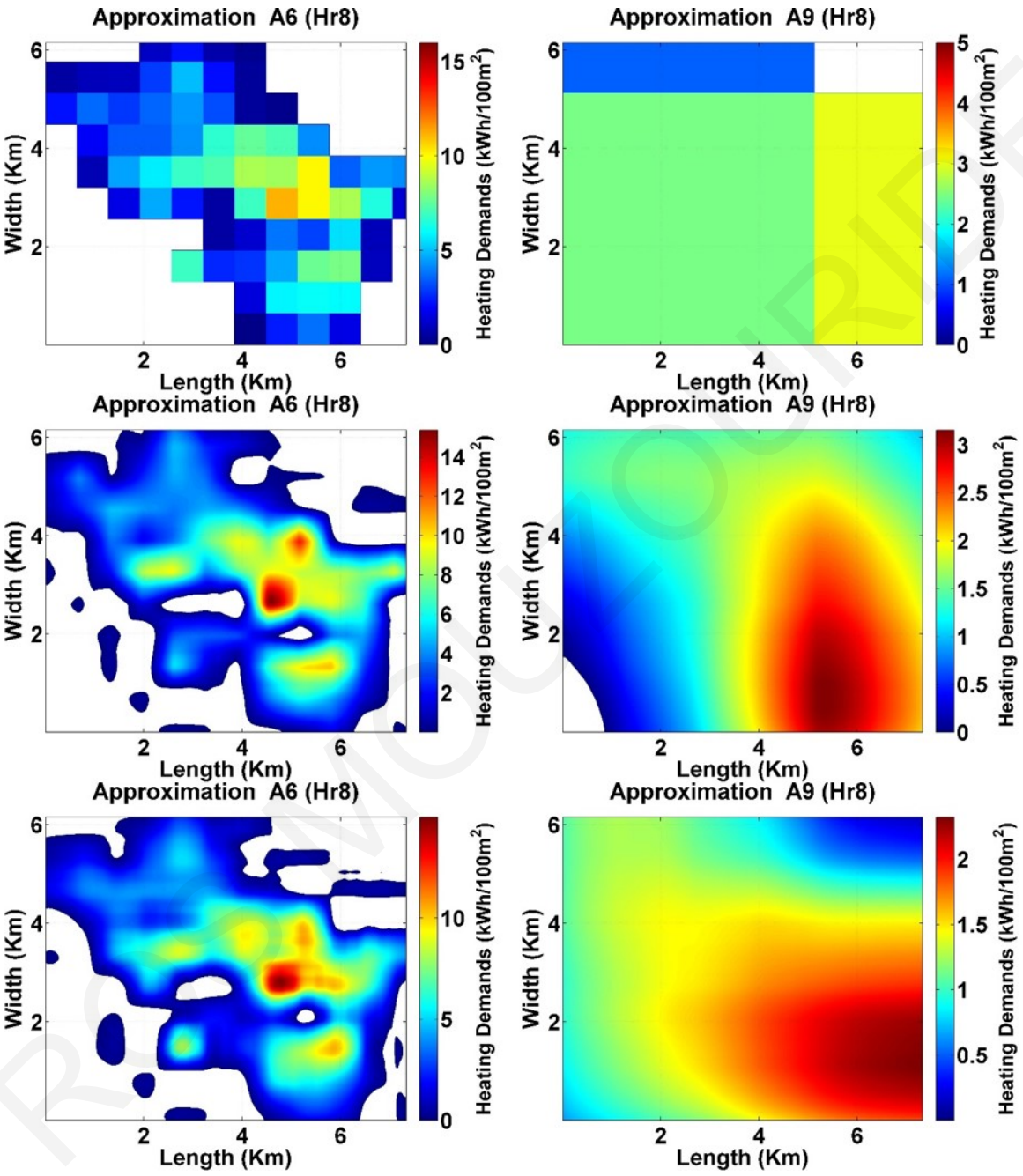

Figure 4.19: A snapshot (at 0800 hours) from the accompanied movie showing the diurnal time evolution of the MRA results obtained at the Approximation Level 6 (left column) and Approximation Level 9 (right column) using the *Haar* (top), *Symlet 4* (middle) and *Daubechie 4* (lower row) scaling functions. [Please watch the full accompanied video denoted as Fig.4.19

to the actual shape of the scaling function (as described in the methodology Fig. 2.3). As aforementioned, in the MRA analysis, different scaling functions must be carefully selected according to the nature of the data. For example, if building-height information across the area is considered, the *Haar* analysing function is recommended due to its multi-scale representation. *Symlet 4* and *Daubechie 4*, on the other hand, can provide smoothening representations (at larger *neighborhood* sizes) while retaining *peak occurrences* across neighborhoods within a district.

4.3.3 Connecting urban-scale building energy demands data with other urban features

4.3.3.1 Relating energy demands with building and population-density parameters

The interpretation of built environment at city scale is a complex task because of the variability of a number of factors such as the physical characteristics of the buildings and the influence of urban conditions. A key challenge in analysing urban-scale energy data is to make sense of large amounts of spatio-temporal data associated with energy consumption in a manner that is useful, tractable, efficient, and flexible for decision-makers. Through the MRA analysis, it is possible to examine the influence of physical features and/or urban context on energy demand.

To do so, the 2D correlation coefficients (R) between the MRA approximations of energy demands and (i) the population density and (ii) the building and land use parameters (building height and planar packing density - λ_p) at different (resolution) Levels were derived. Typically, a 2D correlation coefficient is used to detect similarities between two images or two 2D signals. The aim in this investigation is to observe the daily variation of the correlation between the energy demands with these parameters across different scales (i.e Levels of Approximation). The results in Fig. 4.20 show the values of these correlations as the Approximation Level changes as well as their temporal evolution during the day.

Specifically, results in Fig. 4.20 depict a high correlation between the energy demands of a typical winter day and the physical characteristics of buildings (building height and packing density). The correlation coefficient between the energy demands of a typical winter day and the built area characteristics (buildings height and planar packing density) is found to be higher than 0.93 during daytime for ap-

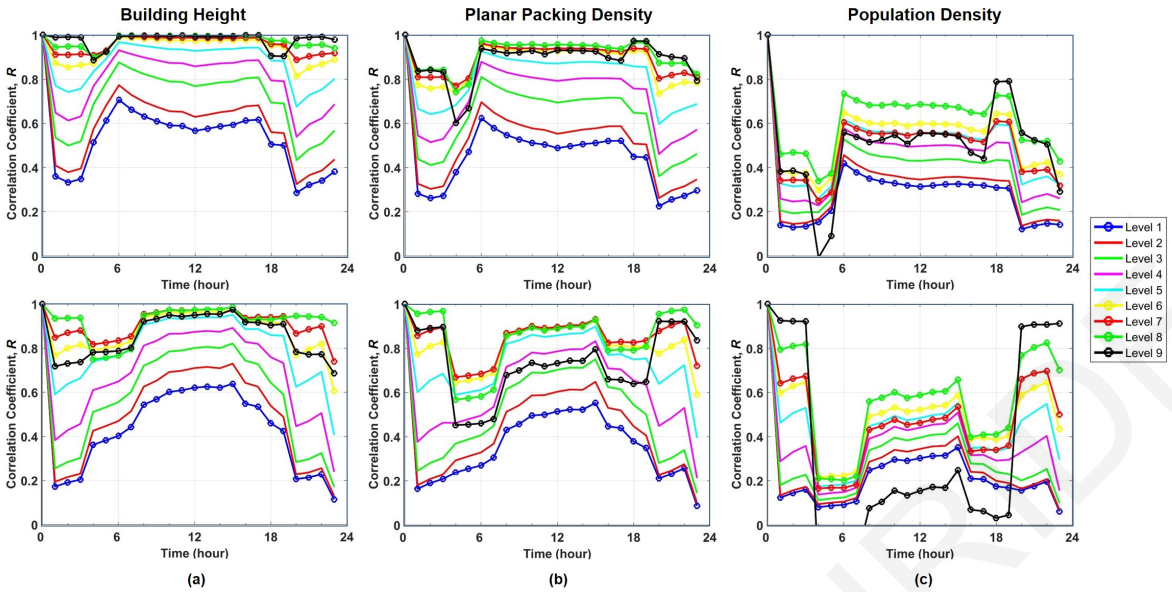

Figure 4.20: Diurnal variation of the Correlation Coefficient, R of heating demands with (a) building height (b) planar packing density and (c) population density across different levels of Approximation (i.e. area sizes) for a typical winter day.

proximation Level 6 (cell size 640 m $\times$ 640 m) and above. This result can be attributed to the fact that in the day-time hours there is full business activity, especially at offices and retail stores. Contrary, during the nocturnal hours, where the population is less active (not working), the correlation of energy demands with population appears (as expected) significantly lower. Generally, the correlation between the heating energy demands with the population residing in the Westminster area exhibits low correlation values, probably because during most of the day time, the residences are unoccupied, therefore there is no energy demand. The only case where there is a high correlation between the heating energy demands and the population, is between 18:00 - 19:00 at approximation Level 9. This occurs because this is rather a transition time in the peoples activity where the usual working hours end and people move to the place of their residence. As a result, residences which were previously unoccupied become occupied space and thus there is an increasing energy demand. Therefore, the conclusion is that the energy demand is strongly related to the population between the hours 18:00 - 19:00 as far as the temporal patterns are concerned. This conclusion covers and concerns the entire region of Westminster Borough. It is noted that as the spatial scale of examination of the correlation coefficient becomes smaller, the actual quantitative value of the correlation coefficient is reduced, this is because it becomes more inclusive of other cross-neighboring cells effects and

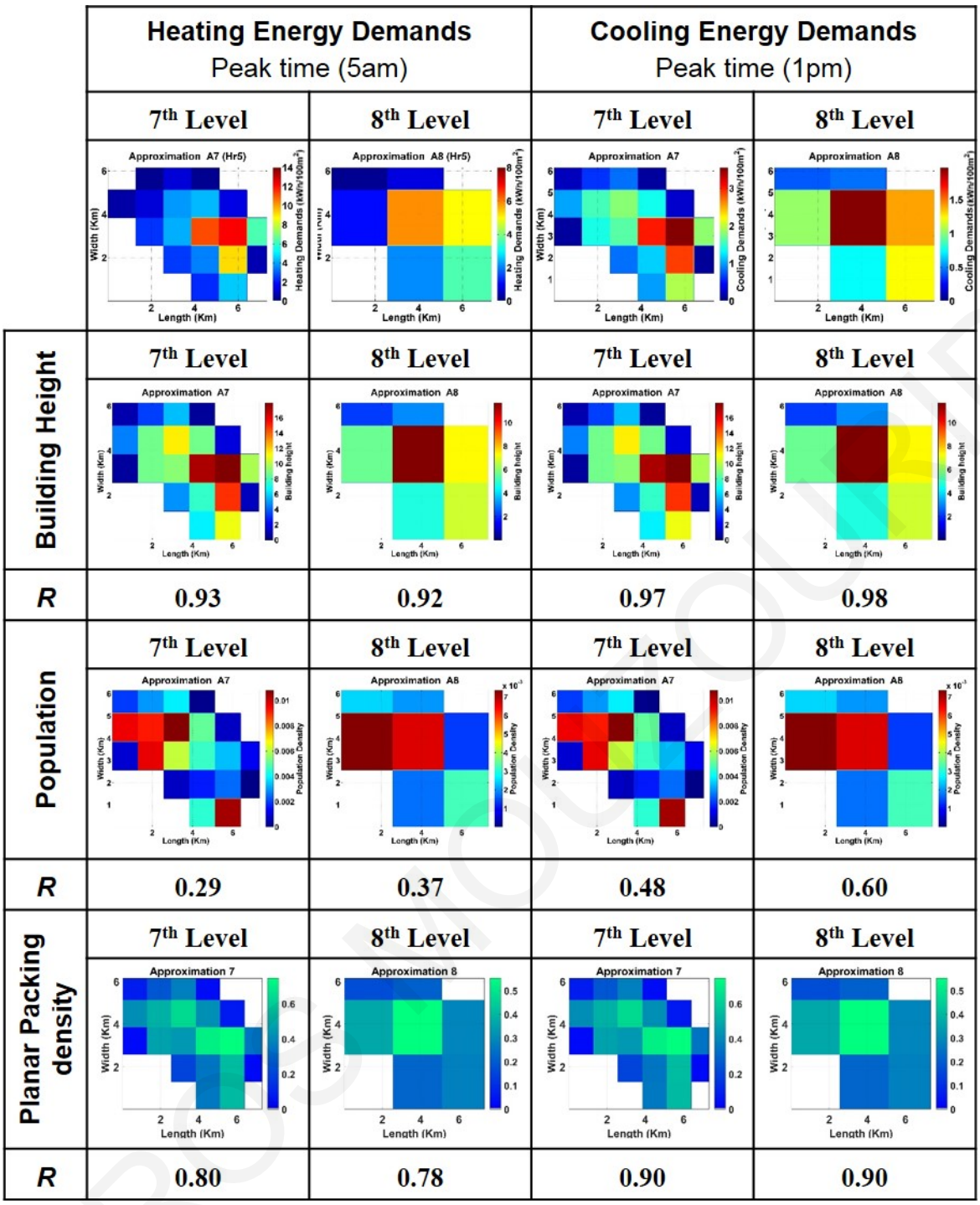

Figure 4.21: The correlation coefficients of the heating energy demands (of a typical winter day at peak hour 05:00) with respect to (a) building height (b) population and (c) planar packing density.

the number of cells accounting for the calculation is larger (for the finite-size area considered in this example). However, in all cases the diurnal pattern remains the same both for the typical winter, spring, summer and autumn days.

Fig. 4.21 shows the scale-adaptive representations (from Levels 6 and above) of the spatially-varying correlation coefficients. The collective value of the correlation coefficient between the heating energy demands of a typical winter day with respect

to building height, population and packing density, at the peak hour of 05:00 is listed below each figure. This figure illustrates the sensitivity of the correlation coefficient to the neighbourhood (scale)-size; it appears that for the building characteristics (building height and planar packing density the correlation coefficient across scales is consistent. However, the correlation coefficient between heating demand and population at 05:00 is weak and random across scales. This is indicative of the fact that large areas within the Westminster borough are non-residential and therefore there is no consistent heating demand during non-work hours.

4.3.3.2 Relating energy demands with city breathability

It is accepted that high-resolution urban-scale energy datasets are not yet widely available and neither yet easily-possible to collect. On the contrary, physical information of buildings is more widely available and if not, it is more accessible to collect or obtain. In recent studies of urban fluid dynamics, it was found that it is possible to relate physical forms of cities (using detailed building information) with the aerodynamical response of the urban configurations, particularly in terms of the air flow within the street canyons [79]. In particular, the capacity of a city to ventilate itself and thereby remove heat or pollutants, or other scalars from its street canyons was termed by Neophytou and Britter [77] as city breathability. Moreover, Panagiotou et al. [86], showed that breathabilities vary across a district and these variations are consistent with the packing density of each neighborhood within the district. In this thesis, it is postulated that the heat accumulation that occurs in a neighborhood are correlated with the heating or cooling demands of buildings. For example, a high level of heat flux within a canyon must correspond to lower heating or higher cooling demand from buildings within the same canyon.

Therefore, further to the methodology part described in Sections 4.1 and 4.1.1, MRA results of the energy data were used to derive correlations that can associate the energy demands of the urban area with the breathability capacity and the packing density of urban areas. It has to be noted that such an association is not exhaustive of the all other contributing and confounding parts in forming the energy demands of an urban area: it serves to quantify only the contribution which stems from the air flow ventilation through the urban streets and buildings.

The breathability capacity is quantified using the exchange velocity which is an

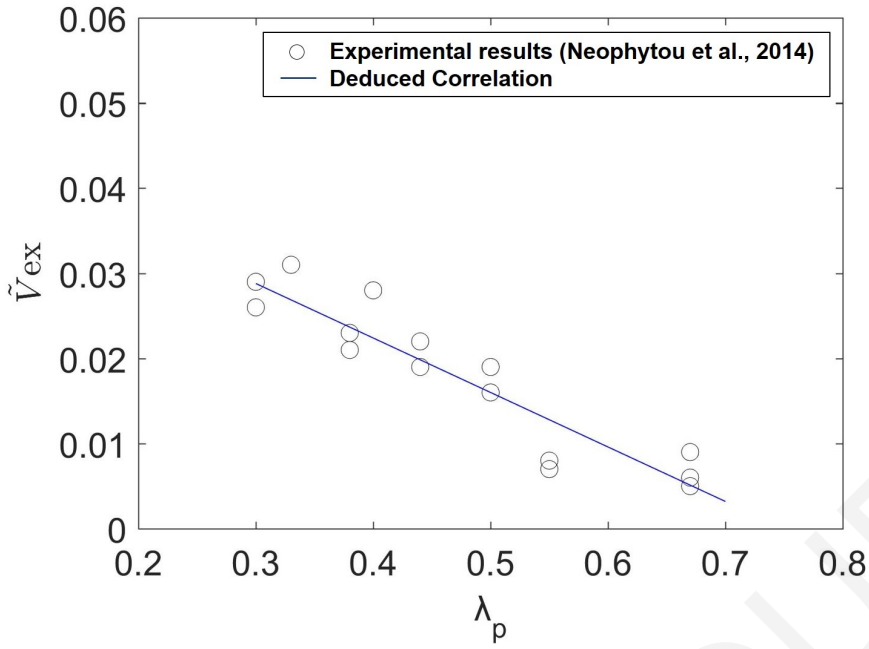

Figure 4.22: The variation of breathability capacity as quantified by the normalized exchange velocity, $\tilde{V}_{ex}$, with the planar packing density, p; the regression line was derived using the experimental results by Neophytou et al. [79] (plotted in this graph).

indicator of the air volume flux exchange at the rooftop levels [79]. Exchange velocity is the rate at which fresh, cool air enters the street canyons from the rooftops level and at the same time warm polluted air from within the street canyons escapes above the rooftop levels. This rate, as quantified by the exchange velocity and termed as breathability, determines eventually the outdoor air conditions (temperature and pollution levels) within street canyons and thereby the demands for heating or cooling within buildings. The breathability capacity as a function of the packing density of an urban area was tested in laboratory experiments by Neophytou et al. [79]. Fig. 4.22 shows the variation of the normalized exchange velocity with the urban canopy morphological parameter λ_p as presented by Neophytou et al. [79]. For the objectives of this study, that is the scale-adaptive representation of city breathability, we assume a linear variation of the non-dimensional with the geometric packing density λ_p, as suggested from the experimental results. The initial values of $\tilde{V}_{ex}$ (corresponding to the initial resolution of the urban building data) were deduced by using the packing density data of Fig. 3.8b and Eq. 4.23 as follows

$$\tilde{V}_{ex}(\lambda_p) = -0.064\lambda_p + 0.048 \tag{4.1}$$

Having illustrated the ability to identify transient spatial structures of energy demand in relation to features of buildings (heights), neighborhood (packing density) and context (population), this section examines the relationship between city breathability with associated energy demands of the city. City breathability, as used by Panagiotou et al. [86], is the capacity of a city to ventilate itself and thereby remove heat (or pollutants) from its street canyons. Thereby, the heat accumulation that occurs in the canyon can be linked to the cooling demands of buildings for satisfying the needs of indoor thermal comfort (be it for heating). Panagiotou et al. [86] quantified the city breathability as a dynamic parameter called exchange velocity and showed that different breathability capacities can occur within a district with the its variation being linked to the local packing density of an urban area.

Fig. 4.23 shows the diurnal variation of the correlation coefficient between the cooling demands and the breathability capacity (as quantified by the exchange velocity parameter) on a typical summer day for different resolution levels (*neighborhood* sizes). The results indicate an overall negative correlation throughout the day confirming (as expected) that high energy demands are associated with low ventilation (breathability) capacity. The diurnal variation of the correlation coefficient is marked by a quasi-steady variation in the middle day period from 06:00 to 19:00 hours with a numerical value ranging from -0.5 at the smallest scale to -0.9 at the largest scales showing the strong interrelation of the two. The actual absolute numerical values of the correlation coefficient (at a given time in the day) reduces as the size of the neighborhood areas considered is smaller a feature also observed and discussed in the previous scale-adaptive variations of such correlation coefficients. However, the variation in the quantitative value of the correlation coefficient across the Levels (i.e. different scales of consideration) is likely to contain sensitivities of heating demands to other parameters than breathability which emerge more evidently at smaller scales (i.e. more locally than globally).

Fig. 4.24 shows the MRA analysis results across the entire CBD-London Westminster City domain of (a) the packing density, (b) the city breathability, (c) the energy demand for cooling over a typical summer day and (d) the energy demand for heating over a typical winter day - both at 13:00 hours. The information on the breathability (normalized exchange velocity) spatial variation was computed using the packing density information map at the original resolution and the correlation relation (Eq. 4.1) between the packing density and the normalized exchange velocity

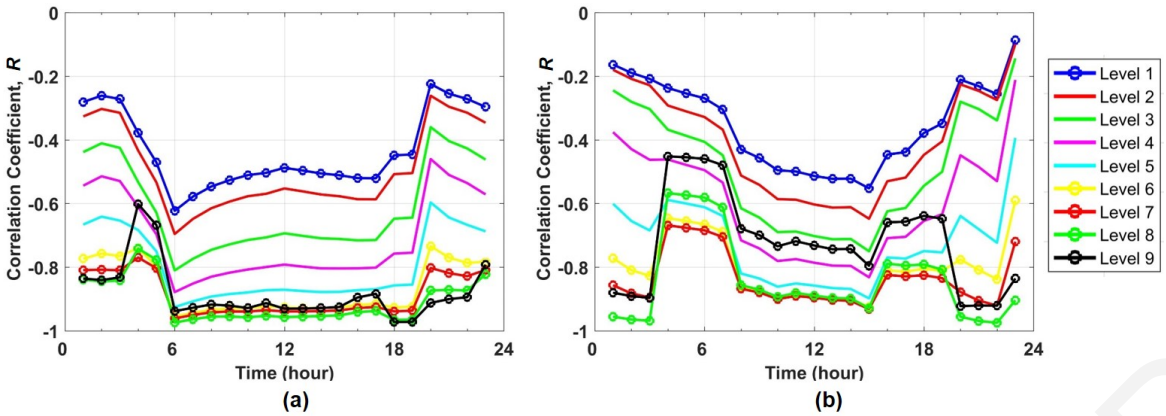

Figure 4.23: Variation of correlation between heating demands of a typical winter day and exchange velocity.

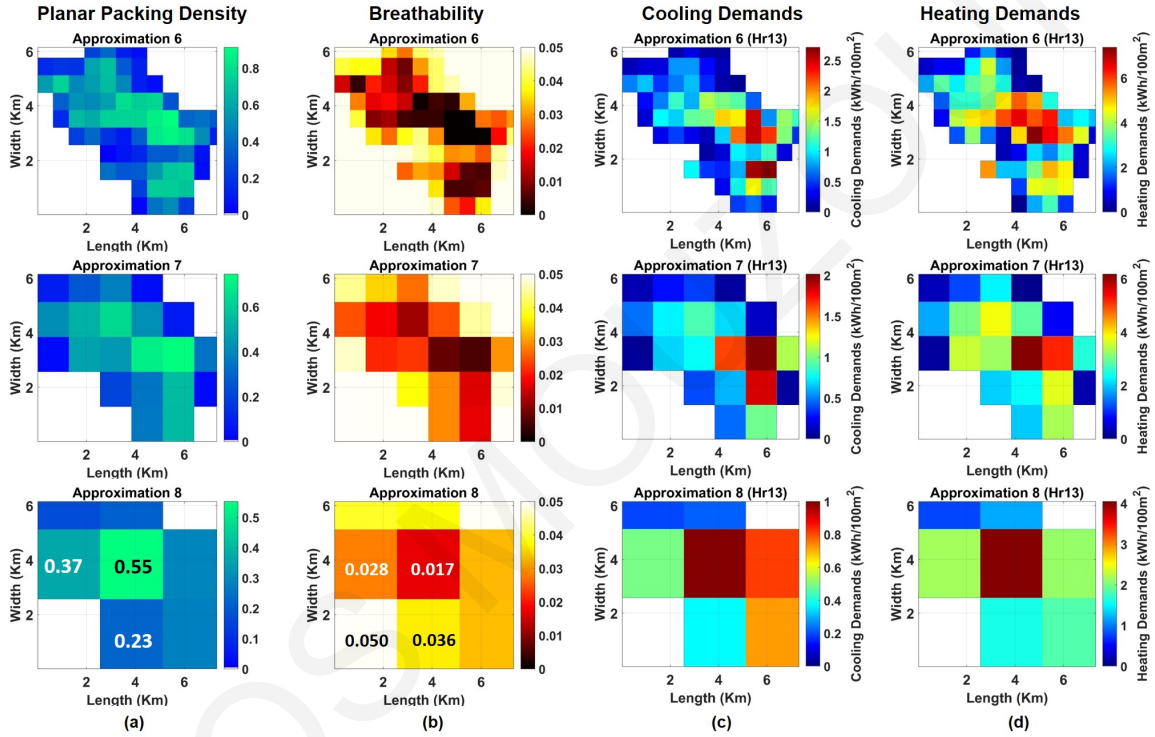

Figure 4.24: MRA deduced results of (a) packing density, λ_p, (b) breathability (normalized exchange velocity), (c) cooling demands of a typical summer day at 13pm and (d) heating demands of a typical winter day at 1300 hours.

(as a quantitative measure of breathability). The selection of the energy demand data at 13:00 hours was made based on the fact that this is still during the normal working hours and it does not exhibit much transitive changes (e.g. during morning arrival at or afternoon departure from work.

Fig. 4.24 very interestingly shows that areas or zones with high energy demands for either heating or cooling are areas with low breathability (low values of normalized exchange velocity).

4.4 Chapter concluding remarks

The key conclusions drawn from this Chapter are summarised below:

1. MRA can be applied on a number of urban building databases in order to provide scale-adaptive, spatially-varying representations of the urban building databases for atmospheric modeling.

2. MRA can be used for distinction between urban databases recognized as identical or similar based on conventional statistics. This provides a sound basis for rigorous inter-comparisons between different urban datasets as well as for appropriate representations - suitably adapted to the referenced resolution for mesoscale models. Also, the spatial structure of the MRA results can envision homogeneity and heterogeneity and enables its quantification.

3. It was illustrated how MRA-deduced results for the building/floor height and λ_p can be used in conjuction with suggested morphometric models in the literature in order to derive associated coherent, scale adaptive boundary-layer parameterizations of z_0 and d over different domain area sizes/cells.

4. By using a rigorous scale-adaptive approach of MRA, the level of association of urban energy demands with other urban features such as built packing density, urban ventilation and population was investigated and unveiled. Further, correlations of the energy demands with urban information such as the building packing density, building height, population and urban ventilation were deduced and was presented how sensitive such correlations are to scale/size of the district considered.

Chapter 5

Results of the multi-fractal analysis of the flow dynamics and dispersion in a turbulent atmosphere

---

Chapter 5 studies the multi-scale nature and presents the multi-fractal behaviour of high resolution atmospheric data. In order to investigate the multi-fractal nature of atmospheric flow field, the dispersion field and their possible connection, field measurements of meteorological and air quality variables were used. The measurements that were used in this chapter concern the period extending from 1st January 2013 to 30th September 2015.

5.1 Background motivation for multi-fractal behavior of the atmospheric data

At first, there will be a brief presentation of some evidence suggesting the multi-scale behavior of the atmosphere and then the results of multi-fractal method of atmospheric timeseries will be presented and discussed.

5.1.1 Local scale effect on Air Quality measurements

In order to identify the presence and characteristics of different sources of air pollution, bivariate polar plots were used. These plots are constructed by partitioning

wind speed/direction data with the same values - and their corresponding concentration data - into wind speed/direction bins (boxes). Then (for each bin) the mean concentration value is calculated. For better visualization, and quick directional information of potential sources, adjacent bins with the mean concentration values, are smoothed by using smoothing techniques (see [14] for details).

Plots such as those shown in Fig. 5.1 represent continuous concentration surfaces that use smoothing techniques. Therefore colour bars should not be interpreted as measurement values. The conclusions drawn from Fig. 5.1a-c is that the concentration pattern between the three pollutants is different. In the case of NO_2 high concentrations are observed when winds occur along NW-SE direction and the wind speed is smaller than 2 m/s. Additional contribution on NO_2 concentrations is observed when winds occur along SW sector with wind speed and the wind speed up to 3 m/s. Fig. 5.1b shows that CO high concentrations were observed in almost all directions with either large or small wind speeds.

Table 5.1 summarizes both the anthropogenic and natural processes that exist in the surrounding area and affect PM_{10} concentrations. Apart from traffic, which is the main anthropogenic activity, agriculture processes may also have a contribution to PM_{10} concentrations since the areas in NE and SE regions are agricultural. Fig. 5.1c shows that high PM_{10} concentrations are observed mainly when winds blow along NW sector and the wind speed is larger than 6 m/s at this time. Moreover, high PM_{10} concentrations are measured when winds occur along the East North-East (E-NE) and South South-East (S-SE) sectors, and wind speeds are larger than 6 m/s. As seen in Fig. 5.1, PM_{10} concentrations originating from the E-NE and S-SE sectors appear to be arising from the agricultural processes (e.g. field plowing).

While such a representation of the concentration measurements is very useful and can lead to important conclusions, care should be taken in interpreting such representations as this can be misleading at the same time. For example, bivariate polar plots of Fig. 5.1a-c do not take into account the frequency of observation of each measurement and how these measurements affect the overall mean concentration [13]. Smoothed surfaces in Fig. 5.1d-f are more representative since they provide an indication of the weighted concentration (i.e. multiplied by the frequency of occurrence, bin frequency, divided by the total frequency) in order to give an improved representation of the conditions that dominate the overall mean concentration. The weighted bivariate polar plots are shown as a continuous-smoothed

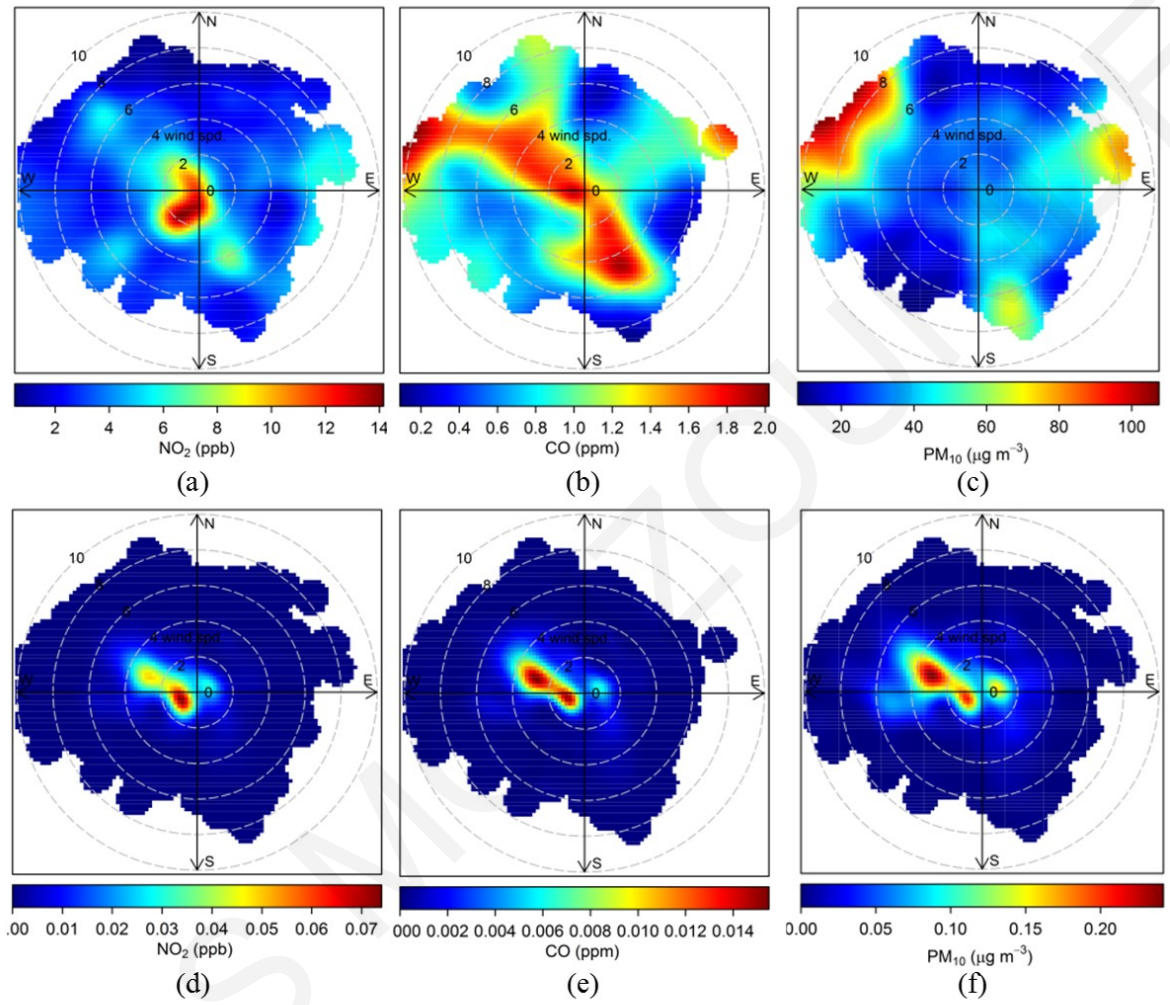

Figure 5.1: Bivariate polar plots for (a) NO_2, (b) CO, (c) PM_{10} (hourly average values were used for all pollutants). These plots present (as smoothed surfaces) how concentrations vary depending on the local wind speed and wind direction. Bivariate-polar-plot surfaces are smoothed in order to provide an indication of the overall pattern. Bivariate polar plots (d) NO_2, (e) CO, (f) PM_{10} represent the same measurements in a different way; all wind speed direction bins were multiplied by frequency of occurrence in order to highlight the main and different sources that dominate the overall mean concentration.

Table 5.1: Anthropogenic and natural processes exist in the surrounding area, and the level of their influence on PM_{10} concentration in region. Symbols ++, + , –, - and 0 denote great gain, gain, great loss, loss and no effect of the corresponding processes on PM_{10} concentration, respectively.

	Processes in the surrounding area	Effect on PM_{10} concentrations
Local anthropogenic process	Exhaust emissions	++
	Emissions from abrasion processes (i.e tyre-wear, break lining)	0
	Road dust resuspension	+
	Building works	+
	Agriculture processes	++
Natural processes	Wind dust resuspension	++
	Regional beckgrounf sources	++
	Sea salt	+
	Dry deposition	-
	Wet deposition	-

surface and present the concentration data in polar coordinates for the purpose of possible source identification. As a result, Fig. 5.1d-f shows that all three pollutants were derived from the same local road traffic sources from the NW sector; in addition, they indicate that the main emissions of PM_{10} are local (small wind speeds), stemming mainly from the NW sector. However, as it was shown in Fig. 5.1a-c, exceedances or large concentration values were observed when dominant winds are coming from NW, E-NE and S-SE sectors with high wind speed. Therefore what is considered necessary is to use both types of plots for understanding the pollutants dispersion in the study area. Quantification of the exact proportion amongst the concentration due to local sources and regional-background concentrations require dedicated detailed studies, which is beyond the scope of current work. The above results allow to conclude that concentrations of NO_2, CO and PM_{10} are primarily due to local road traffic (see Fig. 5.2). The concentrations of NO_2 and CO do not exceed the limit values of EU Directive, whereas PM_{10} concentrations exhibit exceedances. High PM_{10} concentrations values were observed when dominant winds are coming from NW, E-NE and S-SE sectors with wind speed over about 6 m/s.

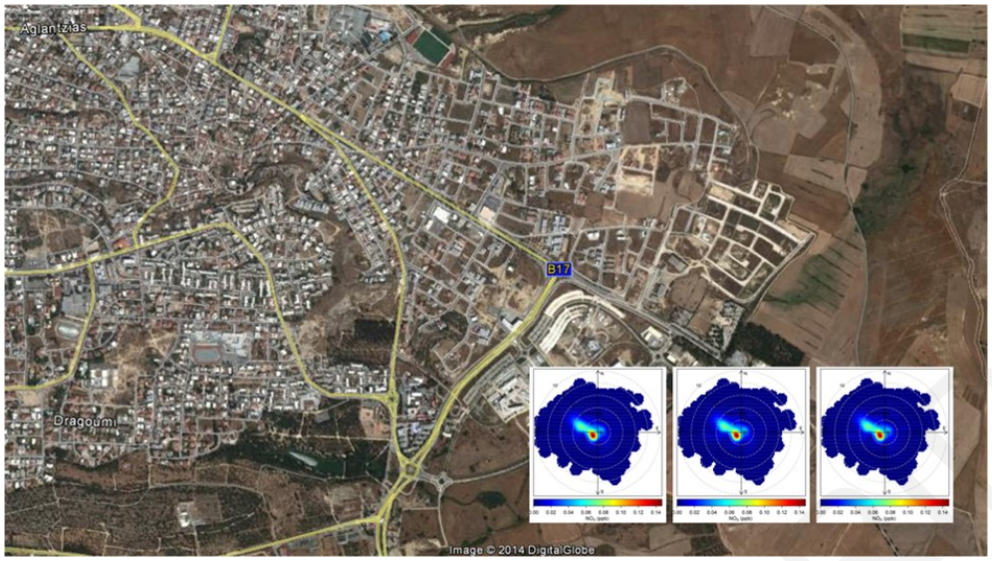

Figure 5.2: The study area with the bivariate polar plots of criteria pollutants (NO_x, CO, PM_{10}) for visualization of emission sources.

5.1.2 Regional scale effect on PM_{10} exceedances

In order to study the regional effect on PM_{10} concentrations, predictions of *BSC/DREAM* model during the dates with exceedences of PM_{10} concentrations were studied. Predictions of *BSC/DREAM* model for the two days with the highest daily average concentration - 24th January 2009 and 18th May 2009, as well as a day that was observed the limit daily mean value of 50 $\mu g/m^3$ (20th June 2012), were chosen to present. In addition, three days between 28th May 2010 until 30th May 2010 were selected to present the temporal evolution of the forecasting of Sahara dust transportation over the atmosphere of Cyprus. The colours on Fig. 5.3 images illustrate the dust load (g/m^2) and the wind vectors at 3000 m over the Mediterranean sea (3000 m above the sea level is the height where the model calculates the dust load); the exact date and time of the prediction is also referenced in the images. The wind vectors indicate the origin of air masses which carried the particulate matter and therefore we can deduce the region of origin of dust transport.

Fig. 5.3 presents the temporal evolution of predicted dust load for three consecutive days starting from 28th May 2010 until 30th May 2010, as a representative example of a comparison between PM_{10} concentration measurements and aerosol load prediction. The average daily value of PM_{10} concentrations were 67.8 $\mu g/m^3$, 55.9 $\mu g/m^3$ and 20.7 $\mu g/m^3$ respectively. On 28th and 29th May 2010 the model prediction for aerosol load is 0.05-0.3 g/m^2 whereas the prediction for 29th May of 2010 is 0.0 - 0.05 g/m^2.

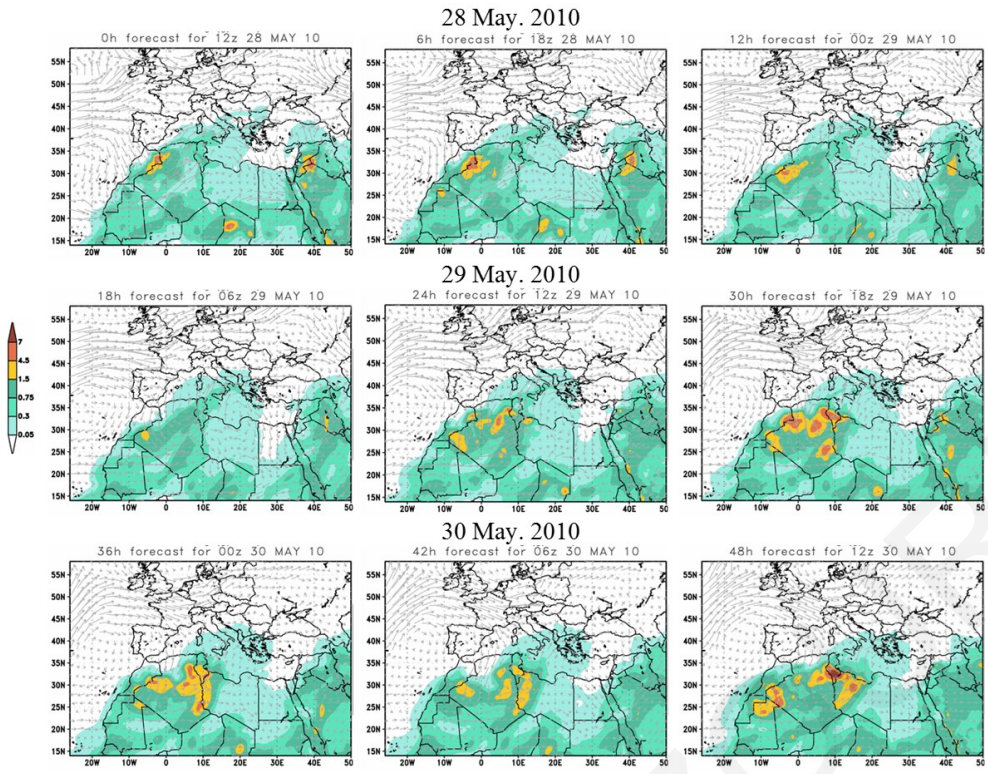

Figure 5.3: Dust load results (g/m^2) from the BSC/DREAM model at 3000 m over the Mediterranean sea as evolution of dust transport phenomena from 28th May 2010 until 30th May 2010; the model yields a prediction every six hours.

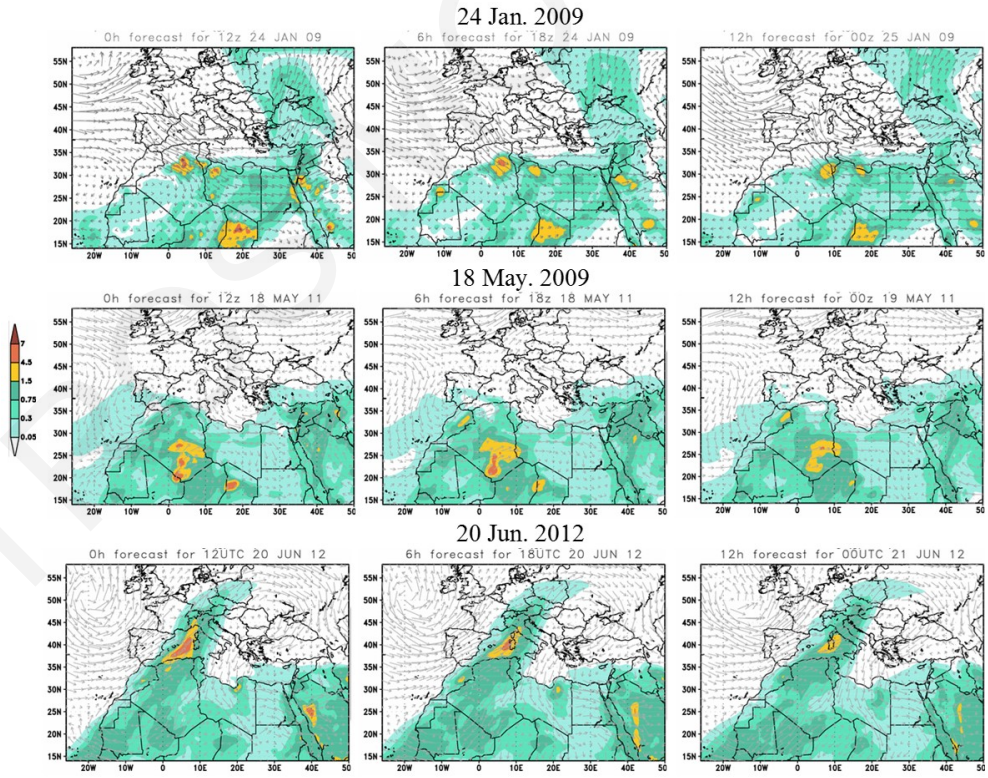

Figure 5.4: Dust load results (g/m^2) from the BSC/DREAM model at 3000 m over the Mediterranean sea as evolution of dust transport phenomena during the days of 24th January 2009 (top row), 18th May 2009 (middle row) and 20th June 2012 (bottom row).

On 24th January 2009 the average daily value was 332.4 μg/m^3 whilst on 18th May 2009 the average value was 259.0 μg/m^3. During these days, model predicts that dust particles transported from the western Saharan region to Cyprus with a high aerosol load (0.75-1.5 g/m^2), whilst on 20th June 2012 the aerosol load was 0.05-0.3 g/m^2 (see Fig. 5.4). Furthermore, wind vectors confirm the transport of air masses from Africa from the W sector. These results are a strong indication of the effect of regional background dust concentrations on PM_{10} exceedences, result that is also found for other locations, such as London by Charron et al. [15] using backward trajectories methods.

5.2 The multi-fractal nature of the dispersion and flow field

The aim of this Chapter, is to investigate the multi-fractal behavior of the meteorological variables of wind speed (WS), ambient temperature (AT) and air quality measurements of concentrations of carbon monoxide (CO) and particulate matter with diameter of $10\mu m$ or less (PM_{10}) compare to L_{MO}, and estimate their h exponent under different atmospheric conditions. Before the results are presented, a brief description of the characteristic length scales and the corresponding Reynolds numbers of the atmosphere in which the measurements were taken, is given.

Atmospheric data collected over a 33-month period in a sub-urban atmospheric boundary layer were used. The Reynolds number (see Eq. 1.1), based on the atmospheric boundary layer height, over the entire period ranged from 0.7×10^6 to 1×10^9, satisfying the pre-requisite of a high Reynolds number flow. The atmospheric boundary layer height, H_a, ranged from 50 to $2018m$, signifies in this analysis the largest scale in the flow L_o (See Table 5.2). The ratio of the largest, L_o , to the smallest, Kolmogorov, scale, n , ranged from 9×10^4 to 3×10^6. The Reynolds number based on the Taylor micro-scale λ, Re_λ , ranged from 280 to 8845, which is considered sufficiently high.

In atmospheric boundary layer apart from wind shear, TKE is generated by buoyant forces as well. Based on the Monin-Obukhov similarity theory, L_{MO} is physically interpreted, as the height at which the buoyant production of TKE is equal to that produced by the shearing action of the wind. Monin-Obukhov length

Table 5.2: Summary of dataset and Atmospheric Boundary Layer properties, of the study area during the period between 1st Jan. 2013-30th Sep. 2015. Also, the table, presents the number of sub-datasets that were used during the study period, using hourly average data and one average value per minute data

Conditions			H [m]			L_{MO} [m]		
Characteristics of the measurement period extending from 1st Jan. 2013-30th Sep. 2015 $Re = 0.7 \times 10^6 - 1 \times 10^9$ $Re_\lambda = 280 - 8845m$		Percentage of data[1] falling in the corresponding stability conditions	Min	Mean	Max	Min	Mean	Max
	Stable ($H/L_{MO}<1$)	41.8%	50	127	953	3	56	833
	Neutral ($-0.3 \leq H/L_{MO}<1$)	2.9%	50	738	2018	-10000	1058	10000
	Unstable ($H/L_{MO}<0.3$)	24.8%	63	715	1948	-5000	-162	-3
Hourly average data		14 sub-datasets						
One average value per minute	Stable	19 sub-datasets						
	Unstable	19 sub-datasets						

is defined as:

$$L_{MO} = \frac{-u_*^3}{\kappa g F_{\theta_o}/\rho c_p T_o} \tag{5.1}$$

where u_* is the friction velocity at the ground surface, $\kappa = 0.4$ is the von Karman constant, g is the acceleration due to gravity, F_{θ_o} the surface heat flux, T_o is the surface temperature and ρ, c_p are the density and specific heat capacity of the air respectively.

Based on the Monin-Obukhov length, the atmospheric stability is divided into the following three broad classes, Stable (S), Neutrally stable (N) and Unstable (US) class defined by:

$$Stable : H/L_{MO} \geq 1, \tag{5.2a}$$

$$Neutral : -0.3 \leq H/L_{MO} < 1, \tag{5.2b}$$

$$Unstable : H/L_{MO} < 0.3 \tag{5.2c}$$

For the collected dataset, it was found that 41.8% of the data falls in the S class, 2.9% of the data falls in the N stable class and the 24.8% falls in the US class (the rest of 30.5% of the data cannot classified because of missing data).

Data processing for multi-fractality

This Chapter, proposes the use of WTMM method to analyse the collected measurements, due to the inherent property of the method to be well-localized in time and therefore its capacity to locate isolated singular events and to characterize more

complex multi-fractal signals having non-isolated singularities. The purpose of this section is to obtain an insight on what are the optimal requirements of the followed methodology in order to calculate the $D_c(h)$ of the stochastic process (hereafter we denote the calculated singularity spectrum with $D_c(h)$) as reliably as possible compare to the theoretical $D(h)$. The derivation of $D_c(h)$ of real monitoring data raises issues on the numerical method which was followed; issues stemming from the discretization of the real signal and by applying the method to that discrete signal.

Despite the fact that simulation data can be obtained by-design to adhere or conform to various data analysis requirements, laboratory and particularly field data have some inherent restrictions: either, due to the limited and finite feasible time duration of data acquisition affecting the ratio of the largest to smallest time scales present in the signal for a given sampling frequency, or due to the variability of the natural conditions in the field hence restricting further the length of a signal. Additional practical unexpected problems hindering data acquisition may arise such as the forced or accidental interruption of power supply and thereby acquisition. Such practical restrictions bring up theoretical signal-processing issues which unavoidably have to be treated appropriately to ensure that any deductions are unaffected by such practical restrictions.

Here, we explore the performance of the multi-fractal method as a function of different implementation parameters in order to avoid spurious deductions relating to physical insights. The implementation parameters that were investigated are: (i) the duration of timeseries; (ii) the number of intermediate scales that should be used in order to calculate the wavelet coefficients (since the calculation of wavelet coefficients for an infinite number of scales is computationally impossible) and (iii) the length of neighborhood size where $|Wf(u, s_0)|$ is locally maximum and the range of q that the analysis is valid. A stochastic signal of fractional Brownian Motion (fBm) with pre-selected $h = 0.8$ exponent (Fig. 5.5), was selected in order to investigate optimum configuration of the method.

The fBm signal is the only signal to our knowledge which is computationally feasible to reproduce a stochastic signal with capacity to be of mono- or multi-fractal nature [34].

The results of analysis of the artificial constructed signal fBm with $h = 0.8$ as a function of the aforementioned parameters are presented in singularity spectra of Fig. 5.6. The left branch of $D(h)$ is obtained for positive values of q's and characterizes the

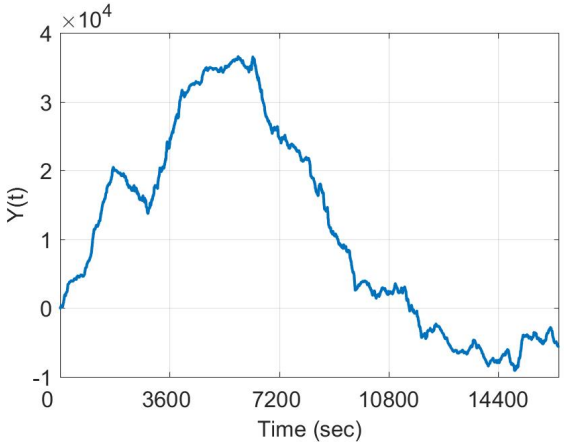

Figure 5.5: A realization of stochastic signal of fractional Brownian motion (fBm) with pre-selected $h = 0.8$ exponent and signal length = 2^{14}.

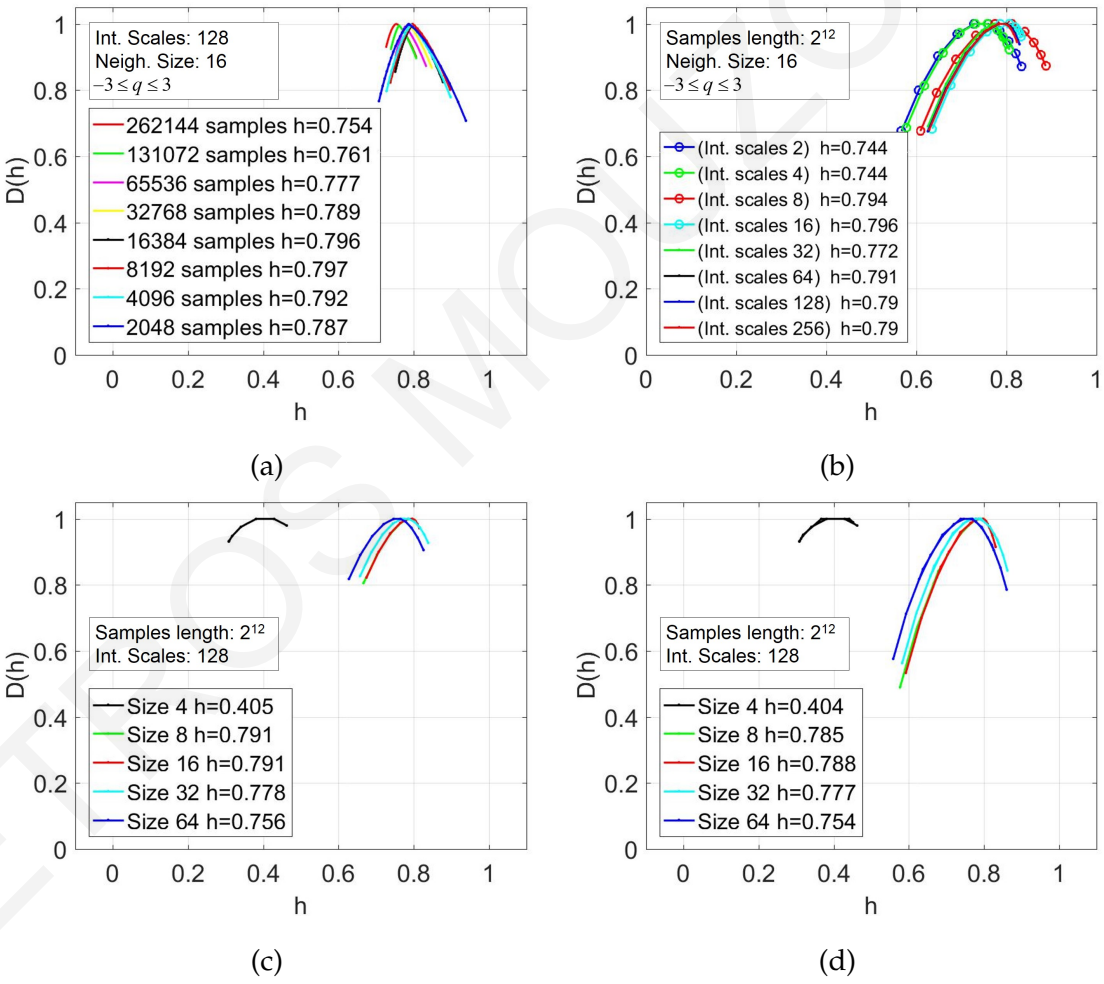

Figure 5.6: Singularity spectra $D_c(h)$ of artificial signal fBm as a function of the dataset samples length (a), the number of intermediate scales (b), as a function of q parameter (c) and the size of neighborhood that $|Wf(u, s_0)|$ is locally maximum (d).

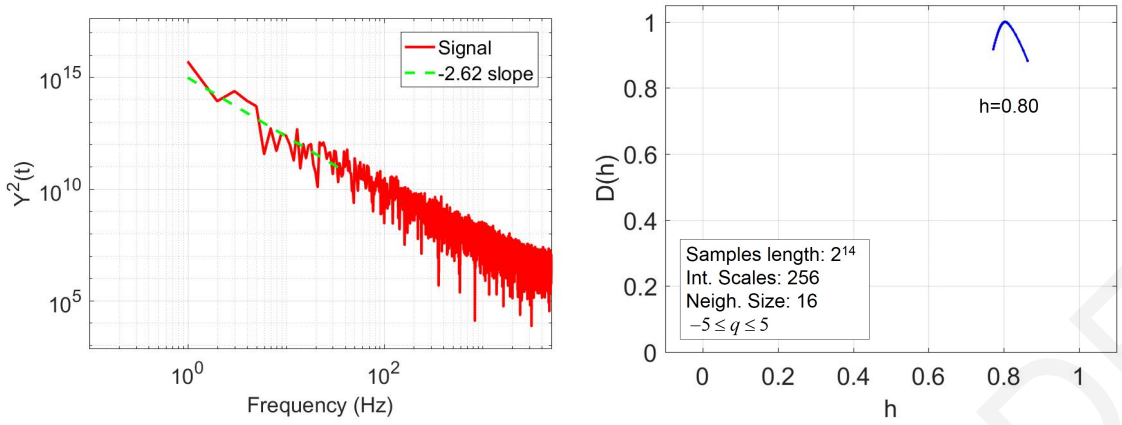

(a) (b)

Figure 5.7: An example of power spectrum (a) and singularity spectrum (b) of a realization of fBm with $h = 0.8$ (Fig. 5.5) in order to verify the satisfaction of Eq.5.3.

strongest singularities, whilst the right branch is associated with the weakest local singularities in time series [81] and is obtained for negative parameter q. Therefore the length of each branch of $D(h)$, implies the kind of singularities that are dominant in the signal.

Fig. 5.7b presents the optimal requirements of the method in order to achieve numerical convergence of calculated h to the prescribed $h = 0.8$. According to the results of Fig. 5.7b, the minimum number of samples needed were 2^{11}, the size of intermediate scales to be at least 256 and the selection of q parameter should be in the range $-3 \leq q \leq 3$. Furthermore, the optimum length of neighborhood size where $|Wf(u, s_0)|$ is locally maximum is recommended to be equal to 16 samples. Moreover, to confirm the validity of WTMM results, the power spectrum of all sub-datasets was computed to verify the linear connection between the asymptotic decay β of power spectrum and the dominant h exponent according to the equation [97]:

$$\beta = 2h + 1 \tag{5.3}$$

For sake of demonstration of the methodology, Fig. 5.7 presents the power (5.7a) and singularity (5.7b) spectrum of realization of fBm with $h = 0.8$ of Fig.5.5.

5.2.1 Multifractal analysis

In this section we will investigate the multi-fractal behavior of the fluid dynamics and dispersion field. We apply the WTMM method in 14 sub-datasets of hourly average measurements of the meteorological variables of WS, AT and air quality

measurements of concentrations of CO and PM_{10}, to unveil the underlying scaling laws of their timeseries. It is important to mention that most of the sub-datasets that were analysed in this Chapter, could not met the minimum criterion of the optimum number of samples either due to physical restriction in atmospheric conditions (e.g atmospheric stability), either due to practical problems in data acquisition.

The application of WTMM in the above-mentioned datasets leads to the calculation of the corresponding singularity spectrum $D_c(h)$. Results show that all four (4) variables exhibit a multi-fractal behavior. In each case there is a range of the dominant h which occurs for each variable. For example in the case where hourly average collected data of wind speed (consecutive measurements for a period between 3 or 4 weeks) is studied, the $D_c(h)$ of the flow field exhibits a range of dominant h between 0.18 and 0.44, where the statistically prevalent observed value is $h = 0.33$. This value is equal to the value of h under the second hypothesis of Kolmogorov for the homogeneous velocity field of fluid. As already mentioned, the analysis showed that there are some cases where the dominant observed value of $D_c(h)$ differs from the second hypothesis of Kolmogorov. This diversity indicates that there is no universal scaling law which describes the flow field of the atmosphere. Also, diversity of dominant h was observed to the rest studied variables, since the $D(h)$ of AT has a range of dominant h between 0.76 and 1.02, the dominant h for chemically inert pollutant PM_{10} varies between -0.19 and 0.41, and the dominant h for chemically reacting pollutant CO varies between 0.38 and 0.7.

Fig. 5.8 shows the spectrum of $D_c(h)$ of hourly average measurements of (a) WS and (b) PM_{10} (c) AT and (d) CO. For clarity, Fig. 5.8 does not depict all results, but 4 out of a total of 14 sub-datasets. Curves with the same color-line in 5.8a and 5.8b correspond to the same measurement period.

5.2.2 Multi-fractal behavior in the light of different stability conditions

To study the influence of atmospheric stability in the observed self-similarity (h), 19 sub-datasets obtained under stable conditions and 19 sub-datasets obtained under unstable conditions were studied, using recorded field data with sampling rate one-average value per minute. The use of such data will show whether "deeper observation" in scales (i.e smaller scales), different scalling laws can be deduced for

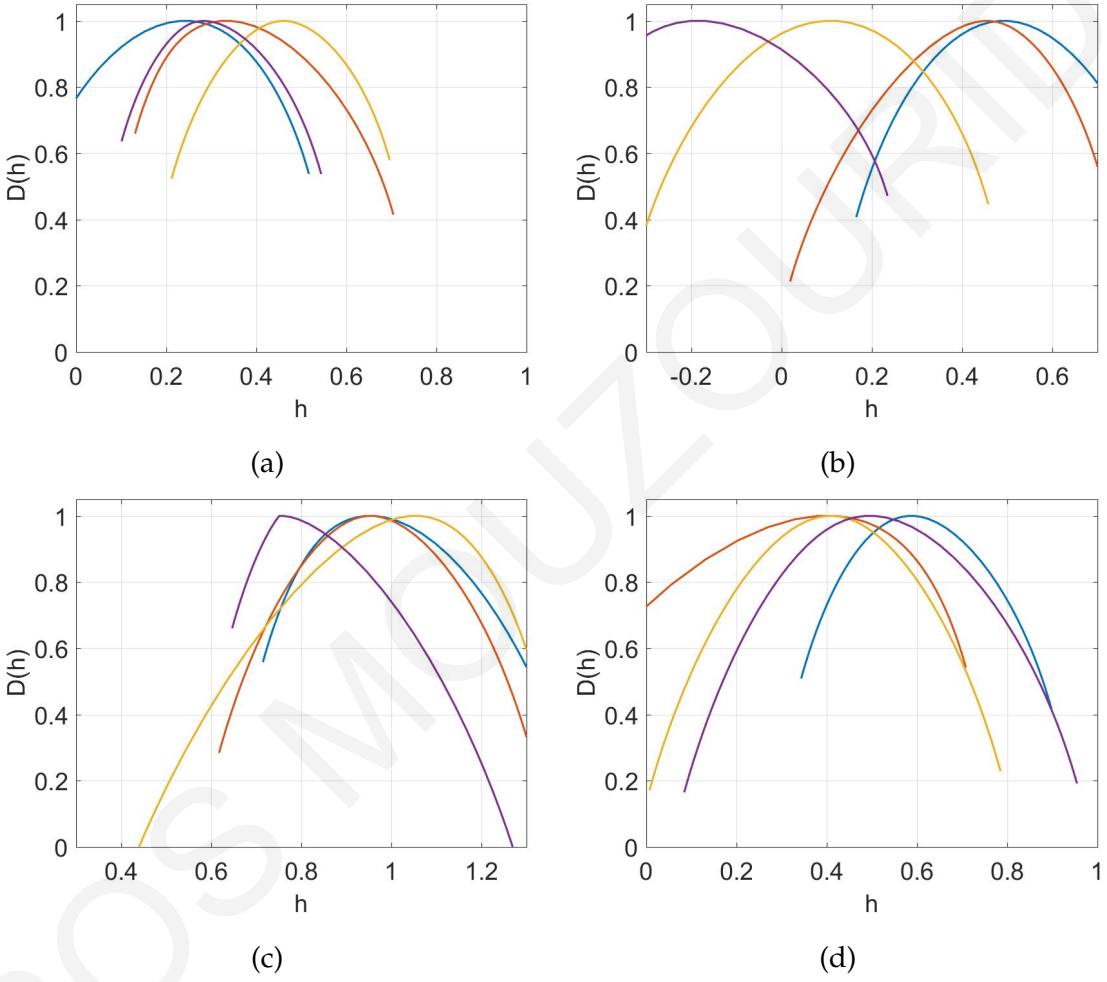

Figure 5.8: The singularity spectra $D_c(h)$ of 4 out of total 14 sub-datasets of hourly average measurements of (a) *WS* and (b) PM_{10} (c) *AT* and (d) *CO*. Curves with the same color-line correspond to the same measurement period.

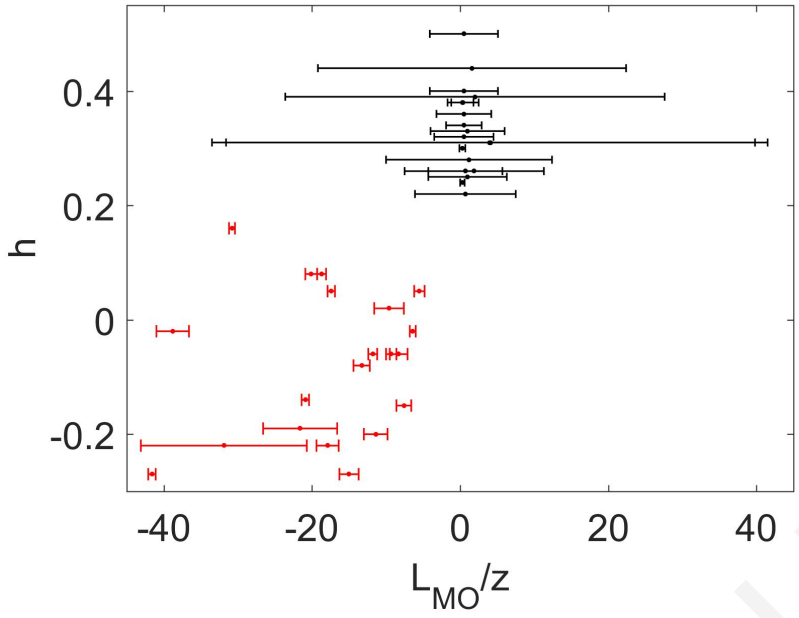

Figure 5.9: The dominant Hurst exponent of the 38 different sub-datasets versus the ration of Monin-Obukhov length over the height above ground of the wind measurements z_0 under stable (black) and unstable (red) conditions

the investigated stochastic processes.

Fig. 5.9 shows that when the atmosphere is stable (i.e the mean value of the ratio $H/L_{MO} \geq 1$) and at the same time the mean value of L_{MO} over the height above ground of the wind measurements,z_0, is $z_0/L_{MO} \leq 1$, (with standard deviation less than 1), the statistically dominant scaling law of the flow field corresponds to Kolmogorov's $-5/3$ law, in agreement with Kolmogorov's hypothesis for statistical independence of large and small scales. So in our measurements under the aforementioned stability conditions in the atmosphere there is a local isotropy on the smallest scales of turbulence and the flow field is homogeneous.

In addition, Fig. 5.9 shows that under unstable conditions, the flow dynamics exhibit different behavior than under stable conditions (black-color results). Specifically, when the atmosphere is unstable (red-color results), the dominant h of flow field was found to be negative. Suggesting that under unstable conditions, there are continued and very fast changes in the flow field (i.e sharp velocity gradients), which has also been reported in previous studies [2]. Therefore we can state that there is a local heterogeneity in the smallest scales of turbulence and the flow field is anisotropic.

The dataset analysis for the dispersion field reveals the same qualitative results

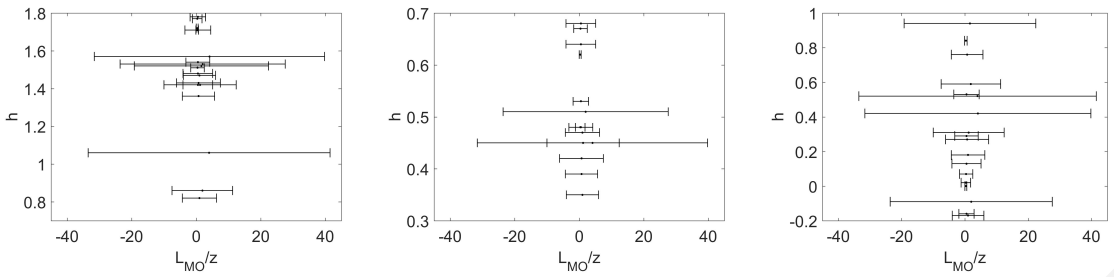

Figure 5.10: Maximum Hurst exponent of the 19 different sub datasets versus the ratio of Monin-Obukhov length over the height above ground of the wind measurements, z_0, for (a) the chemically inert pollutant PM_{10}, (b) chemically reacting pollutant CO and (c) ambient temperature AT under stable conditions in the atmosphere.

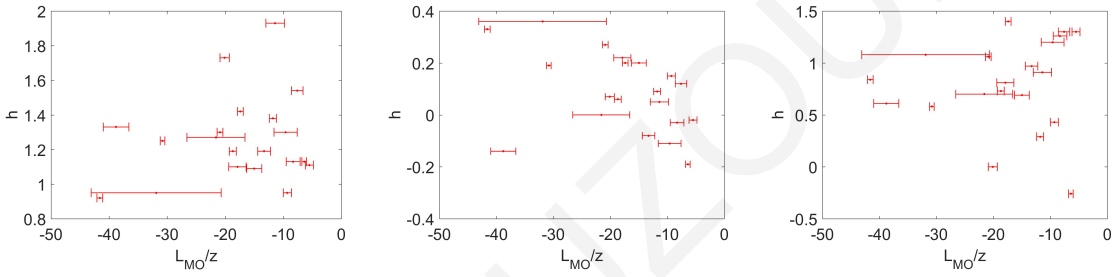

Figure 5.11: Maximum Hurst exponent of the 19 different sub datasets versus the ratio of Monin-Obukhov length over the height above ground of the wind measurements, z_0, for (a) the chemically inert pollutant PM_{10} and (b) chemically reacting pollutant CO and (c) ambient temperature AT under unstable conditions in the atmosphere.

under stable and unstable conditions, i.e multi-fractal behavior of the concentrations, long-range correlation of the chemically inert pollutant PM_{10} and short-range dependence of the chemically reacting pollutant CO.

The analysis showed that under stable conditions, the dominant h for a chemically inert pollutant such as PM_{10} varies between 0.82 and 1.78 whilst the dominant h for a chemically-reacting pollutant such as CO varies between 0.35 and 0.68 (Fig. 5.10). Further, it was found that under unstable conditions, the dominant h for the chemically inert pollutant PM_{10} varies between 0.92 and 1.93 whilst the dominant h for the chemically reacting pollutant CO varies between -0.11 and 0.36 (Fig. 5.11). This wide range of exhibited dominant h concentration fields, verify that the physiochemical processes which take place in the atmosphere occur over a wide range of spatial and temporal scales.

In the case of the ambient temperature data, it was found that the atmospheric stability affects the results as well. Under stable conditions the dominant h of ambient temperature varies between -0.09 and 0.94, whilst under unstable conditions the dominant h of ambient temperature varies between 0.29 and 1.40. Therefore, the ambient temperature exhibits a multi-fractal structure; with a wide range of values of h according to their atmospheric stability conditions during the data acquisition. In order to deeply understand this difference over the season, there is still work needed to be done. For example the study should be done by using more selection criteria, like diurnal/nocturnal variability of measurements.

5.2.3 Relating multi-fractality with long-range correlation

The goal of this section is to interpret the physical meaning of the results on the multi-fractal behavior of the measured field data. As described in Section 1.1.3, the long- or short-term correlation in timeseries fluctuation is associated with h when the stochastic process has stationary increments.

Two different stationarity tests, the Augmented Dicky - Fuller (ADF) and Kwiatkowski - Phillips - Schmidt - Shin (KPSS) test, were used in order to test the hypothesis that an observable time series is a stationary trend or whether a timeseries has stationary increments. The difference between the two methods is that the null hypothesis of the ADF-test is the unit root hypothesis (the alternative hypothesis corresponds to a no unit root process), whilst the null hypothesis of KPSS-test corresponds to a trend-stationary process and the alternative corresponds to a unit root process. By using both tests; the unit root and the stationarity test, one can distinguish whether the timeseries is stationary or non-stationary at a certain confidence level or whether the timeseries data (or the test) is not sufficiently informative to be sure whether the timeseries is stationary or not.

The analysis indicates that the datasets of the chemically inert pollutant (PM_{10}) and chemically reacting pollutant (CO) timeseries have unit root regardless of the stability of the atmosphere, which means that any abrupt change in the concentration of these pollutants, will have an increasingly large influence on the atmosphere through the time. For example high values of h ($h > 0.5$) for chemically inert pollutant PM_{10} indicate long-range correlation of data fluctuation which in turn is likely indication of trans-boundary pollution transport. On the other hand, the traffic-

Table 5.3: Results of the stationarity tests for wind speed (*WS*), ambient temperature (*AT*) data, the chemically inert pollutant (PM_{10}) and chemically reacting pollutant (*CO*)

	ADF-test	KPSS-test
Stable Conditions		
WS	Stat. with linear drift	Non-Stationary
AT	Stat. with linear drift	Non-Stationary
PM_{10}	Unit root	Non-Stationary
CO	Unit root	Non-Stationary
Unstable Conditions		
WS	Stat. with linear drift	Non-Stationary
AT	Stat. with linear drift	Non-Stationary
PM_{10}	Unit root	Non-Stationary
CO	Unit root	Non-Stationary

related chemically reacting pollutant *CO* also exhibit a multi-fractal behavior, but the low observed values of h confirm the short range correlation of data fluctuation and thereby a rapid change in *CO* emission rate, associated with load, has a significant impact on the *CO* concentration.

In the cases where we analysed the wind speed (*WS*) and ambient temperature (*AT*) timeseries, the results are not sufficiently informative to be sure whether the process is stationary or not. For example, the ADF test presents the timeseries of both variables to be stationary with linear drift, whilst the KPSS test estimates the timeseries of both variables to be non-stationary. This conclusion is independent of the atmospheric stability. Table 5.3 summarizes the results of the corresponding test where each test was conducted for p-value equal to 0.05.

5.3 Chapter concluding remarks

The key conclusions drawn from this Chapter are summarised below:

1. Numerical simulations using the Dust REgional Atmospheric Model (DREAM) give a strong indication that the high PM_{10} concentrations and the PM_{10} exceedances are strongly associated with high regional background dust concentrations transported during westerly winds e related to Saharan episodes.

2. The multi-fractal behavior of meteorological and air quality field measurements is revealed. Also the results of this study are in agreement with results of other studies and verify the multi-fractal behavior of fluid dynamics and dispersion in a turbulent atmosphere

3. Based on the analysis of atmospheric measurements, the statistically dominant scaling law of the flow field, varies according to the sample rate or the stability conditions of the atmosphere during the data acquisition. Also, important results were obtained by analysing recorded field data with sampling rate per-minute- average value. For example, when the stability of the atmosphere satisfies the condition $H/L_{MO} \geq 1$ (i.e stable conditions) and at the same time the mean value of L_{MO} over the height above ground of the wind measurements, z_0, is $z_0/L_{MO} \leq 1$ (with standard deviation less than 1) then the $D(h)$ of the flow field exhibit the statistically dominant scaling law of $-5/3$ which corresponds to Kolmogorovs $-5/3$ law. This result leads to the conclusion that Kolmogorovs hypothesis for statistical independence of large and small scales is valid

4. Finally, stationarity test on pollutants concentration shows that the time-series of the chemically inert pollutant (PM_{10}) and chemically reacting pollutant (CO) are non-stationary regardless of the stability of the atmosphere. This implies that any sudden change in the concentration of pollutants, this change will have a permanent impact on the statistics of their time-series.

Chapter 6

Conclusions and Future Work

Chapter 6 summarizes the conclusions drawn from the overall results obtained in Chapters 4 and 5. Moreover, Chapter 6 provides suggestions for future work.

6.1 Summary and Conclusions

In this thesis, it has been illustrated how schemes of WT can be used as a rigorous method to deduce scale-adaptive or scale-aware conclusions and extract scaling laws for different types of atmospheric dynamic problems.

The conclusions of this thesis concerning the 2D urban morphology or building-related data are summarised as follows:

1. This thesis illustrates how the MRA can be applied on a number of urban building databases, in order to obtain scale-adaptive, spatially-varying representations of the urban building information. For models, the MRA provides gridded and scaled attributes as well as sub-grid information for a hierarchy of grid sizes. The MRA can, in principle, provide a powerful means to explore and utilize information at the sub-grid scale to inform the mesoscale analyses, a very powerful resource for multi-scale modeling studies. Specifically, by analysing the urban signal into an *approximation* and a *detail*, different representations of the urban building database can be obtained with respect to different scales or resolutions, namely levels of analysis. Moreover, the spatial or structured representation of the MRA results envisions homogeneity and

heterogeneity and enables its quantification. This provides a sound basis for rigorous inter-comparisons between different urban datasets as well as for appropriate representations - suitably adapted to the referenced resolution for meso-scale models.

2. In addition, the use of MRA as a methodology for conducting the multi-scale analysis of the energy demand data, has enabled a rigorous structural connection to be made between physics at local-scale and larger scales (including neighborhood or city or other scales), thereby achieving a much-clearer understanding of the role of different parameters in the behavior of an urban-scale complex system. MRA methodology enables a more reliable decision-making to be made (e.g. motivated to implement strategies for reduction of building-energy-demands at specific scale) due to its capability to represent efficiently high-resolution data at coarser-resolution without losing the local (high-resolution) information. More specifically, MRA analysis enables identification of spatial and temporal structures within the dataset.

3. MRA has been shown to enable useful methods of determining scale-adaptive and spatially-varying descriptions of aerodynamic urban canopy parameters as a given example of determination of z_0 and d. Finally, through a discussion of examples it was shown that MRA can provide an innovative means to distinguish between urban databases and cities, and in the light of the presented results it can be said that MRA encodes the unique information of an urban morphology database the same way as the DNA encodes the genetic information of all living organisms of the same species - in essence providing a DNA-like description of a city.

Within the framework of WTMM method, the multi-scale nature of the flow and dispersion field was studied, exposing the existence of scaling laws in atmospheric processes. In terms of 1D atmospheric timeseries data the conclusions are summarised as follows:

1. The main outcome obtained from the study of field measurements of meteorological and air quality variables is that their multi-fractal structure was confirmed, exhibiting a wide range of values of Hurst exponents h, over a spectrum, $D(h)$, according to the season that the data was collected. Overall, the

findings about the multi-fractality of atmospheric flow field are in agreement with these of other studies [35, 54, 56, 61].

2. It has been found that based on the analysis of atmospheric measurements, the statistically dominant scaling law of the flow field, varies according to the sample rate or the measuring period of data. For example, in the case hourly average collected data of wind speed of consecutive measurements (for a period between 3 or 4 weeks) is studied, the statistically dominant observed value is $h = 0.33$, which is equal to the value of h under the second hypothesis of Kolmogorov for the homogeneous velocity field of fluid.

3. At the same time, the analysis showed that there are some cases where the dominant observed value of $D(h)$ differs from the second hypothesis of Kolmogorov. This diversity indicates that there is not a universal scaling law which describes the flow field of the atmosphere. The stability of atmosphere appears to play a significant role in the behavior of the atmospheric flow, so it determines the observed scaling laws.

4. Also, novel results were obtained by analysing recorded field data with sampling rate per-minute-average value. The analysis of such data showed that the stability of the atmosphere appears to play a significant role in the behavior of the atmospheric flow, which stability determines the observed scaling laws in the data.

Based on the results of this thesis, it is concluded that applications of Wavelet Transform can be used in order to understand and model multi-scale phenomena in the urban atmosphere.

6.2 Suggestions for future work

The subject and area of research offer a good scope for future work to to deeply understand the different multi-scale nature and behavior of atmospheric processes. There are some recommendations that should be considered for future work:

1. An extension of the application of MRA methodology to additional urban related attributes in order to provide an objective and automated link with urban classification such as the Local Climate Zone as defined in Stewart and

Oke [101], would help current global initiatives such as WUDAPT. Specifically, additional thermal parameters such as the albedo, sky view factor, surface admittance, previous surface fraction would be extremely useful since they are still sensitive parameters in of meso-scale models (e.g. WRF/urban modeling system). Moreover, the creation and the enrichment with more data of global databases such as WUDAPT, will strengthen the efforts of the scientific community for more accurate prediction of the dynamic behavior of the atmosphere.

2. The application of CWT and OWT to the existing dataset by using different Wavelet Toolboxes or different programming environments (e.g Python, Java) as an attempt to understand and overcome computational issues, such as those mentioned in Chapter 5. In addition the wavelet coefficients of this new analysis will be presented in a different way such as Mallat's representation, in order to understand and gain new insight in multi-scale modeling of multi-scale problems in the atmosphere.

3. Finally, the study towards investigating the multi-fractal behavior of flow and dispersion field should be continued. For example the study of multi-fractal behavior of atmospheric processes should be done by using more selection criteria, like diurnal/nocturnal variability of measurements over different type of the urban built settings, climate regions and seasons, so that the various numerical models to be provided with reliable physical insights in order to be able to simulate all possible dynamic conditions in the urban atmosphere.

Bibliography

[1] Y. Ashkenazy and H. Gildor, "Long-range temporal correlations of ocean surface currents," *Journal of Geophysical Research: Oceans*, vol. 114, no. C9, 2009.

[2] E. Bacry, A. Arneodo, U. Frisch, Y. Gagne, and E. Hopfinger, "Wavelet analysis of fully developed turbulence data and measurement of scaling exponents," in *Turbulence and Coherent Structures*. Springer, 1991, pp. 203–215.

[3] K. E. Bassler, G. H. Gunaratne, and J. L. McCauley, "Markov processes, hurst exponents, and nonlinear diffusion equations," *Physica A: Statistical Mechanics and its Applications*, 2006.

[4] J. A. Benediktsson, M. Pesaresi, and K. Amason, "Classification and feature extraction for remote sensing images from urban areas based on morphological transformations," *IEEE Transactions on Geoscience and Remote Sensing*, vol. 41, no. 9, pp. 1940–1949, 2003.

[5] R. Bobbink, M. Hornung, and J. G. Roelofs, "The effects of air-borne nitrogen pollutants on species diversity in natural and semi-natural european vegetation," *Journal of Ecology*, vol. 86, no. 5, pp. 717–738, 1998.

[6] M. Bottema, "Urban roughness modelling in relation to pollutant dispersion," *Atmospheric Environment*, vol. 31, no. 18, pp. 3059–3075, 1997.

[7] E. Bou-Zeid, M. B. Parlange, and C. Meneveau, "On the parameterization of surface roughness at regional scales," *Journal of the Atmospheric Sciences*, vol. 64, no. 1, pp. 216–227, 2007.

[8] R. Britter and S. Hanna, "Flow and dispersion in urban areas," *Annual Review of Fluid Mechanics*, vol. 35, no. 1, pp. 469–496, 2003.

[9] M. Brown, "Urban parameterizations for mesoscale meteorological models," *Mesoscale atmospheric dispersion*, pp. 193–255, 2000.

[10] S. J. Burian, W. S. Han, and M. J. Brown, "Morphological analyses using 3d building databases: Oklahoma city, oklahoma," *LA-UR, Los Alamos National Laboratory, Los Alamos*, 2003.

[11] ——, "Morphological analyses using 3d building databases: Seattle, washington," *Los Alamos National Laboratory: LA-UR-05-1822*, 2005.

[12] S. J. Burian, S. P. Velugubantla, and M. J. Brown, "Morphological analyses using 3d building databases: Phoenix, arizona," *Los Alamos National Laboratory: LA-UR-02-6726*, 2002.

[13] D. C. Carslaw and S. D. Beevers, "Characterising and understanding emission sources using bivariate polar plots and k-means clustering," *Environmental modelling & software*, vol. 40, pp. 325–329, 2013.

[14] D. C. Carslaw and K. Ropkins, "Openairan r package for air quality data analysis," *Environmental Modelling & Software*, vol. 27, pp. 52–61, 2012.

[15] A. Charron, R. M. Harrison, and P. Quincey, "What are the sources and conditions responsible for exceedences of the 24h pm 10 limit value (50μgm- 3) at a heavily trafficked london site?" *Atmospheric Environment*, vol. 41, no. 9, pp. 1960–1975, 2007.

[16] F. Chen, H. Kusaka, R. Bornstein, J. Ching, C. Grimmond, S. Grossman-Clarke, T. Loridan, K. W. Manning, A. Martilli, S. Miao *et al.*, "The integrated wrf/urban modelling system: development, evaluation, and applications to urban environmental problems," *International Journal of Climatology*, vol. 31, no. 2, pp. 273–288, 2011.

[17] Z. Chen, P. C. Ivanov, K. Hu, and H. E. Stanley, "Effect of nonstationarities on detrended fluctuation analysis," *Physical Review E*, vol. 65, no. 4, p. 041107, 2002.

[18] H. Cheng and I. P. Castro, "Near-wall flow development after a step change in surface roughness," *Boundary-Layer Meteorology*, vol. 105, no. 3, pp. 411–432, 2002.

[19] J. Ching, "Wudapt: conceptual framework for an international community urban morphology database to support meso-urban and climate models. newsletters iauc," *Urban Clim. News*, vol. 45, pp. 6–17, 2012.

[20] R. Choudhary and W. Tian, "Influence of district features on energy consumption in non-domestic buildings," *Building Research & Information*, vol. 42, no. 1, pp. 32–46, 2014.

[21] I. Couloigner and T. Ranchin, "Mapping of urban areas: A multiresolution modeling approach for semi-automatic extraction of streets," *Photogrammetric engineering and remote sensing*, vol. 66, no. 7, pp. 867–874, 2000.

[22] I. Daubechies, *Ten lectures on wavelets*. SIAM, 1992.

[23] C. C. Davila, C. F. Reinhart, and J. L. Bemis, "Modeling boston: A workflow for the efficient generation and maintenance of urban building energy models from existing geospatial datasets," *Energy*, vol. 117, pp. 237–250, 2016.

[24] S. Di Sabatino, L. S. Leo, R. Cataldo, C. Ratti, and R. E. Britter, "Construction of digital elevation models for a southern european city and a comparative morphological analysis with respect to northern european and north american cities," *Journal of Applied Meteorology and Climatology*, vol. 49, no. 7, pp. 1377–1396, 2010.

[25] H. A. T. DIRECTIVE, "Directive 2008/56/ec of the european parliament and of the council," *Journal). Council Decision of*, 2008.

[26] M. O. Domingues, O. Mendes, and A. M. da Costa, "On wavelet techniques in atmospheric sciences," *Advances in Space Research*, vol. 35, no. 5, pp. 831–842, 2005.

[27] F. Esposti, M. Ferrario, and M. G. Signorini, "A blind method for the estimation of the hurst exponent in time series: theory and application," *Chaos: An Interdisciplinary Journal of Nonlinear Science*, vol. 18, no. 3, p. 033126, 2008.

[28] M. Farge and G. Rabreau, "Wavelet transform to detect and analyze coherent structures in two-dimensional turbulent flows," *Comptes Rendus De L Academie Des Sciences Serie Ii*, vol. 307, no. 13, pp. 1479–1486, 1988.

[29] M. Farge and K. Schneider, "Wavelets: application to turbulence," *Encyclopedia of Mathematical Physics*, pp. 408–420, 2006.

[30] M. Farge, "Wavelet transforms and their applications to turbulence," *Annual review of fluid mechanics*, vol. 24, no. 1, pp. 395–458, 1992.

[31] M. Farge and E. Guyon, "A philosophical and historical journey through mixing and fully-developed turbulence," in *Mixing*. Springer, 1999, pp. 11–36.

[32] T. Feng, Z. Fu, X. Deng, and J. Mao, "A brief description to different multifractal behaviors of daily wind speed records over china," *Physics Letters A*, vol. 373, no. 45, pp. 4134–4141, 2009.

[33] U. Frisch and R. J. Donnelly, *Turbulence: the legacy of AN Kolmogorov*. AIP, 1996.

[34] P. Goncalves and R. Riedi, "Wavelet analysis of fractional brownian motion in multifractal time," in *17 Colloque sur le traitement du signal et des images, FRA, 1999*. GRETSI, Groupe dEtudes du Traitement du Signal et des Images, 1999.

[35] R. Govindan and H. Kantz, "Long-term correlations and multifractality in surface wind speed," *EPL (Europhysics Letters)*, vol. 68, no. 2, p. 184, 2004.

[36] C. Grimmond, "Aerodynamic roughness of urban areas derived from wind observations," *Boundary-Layer Meteorology*, vol. 89, no. 1, pp. 1–24, 1998.

[37] C. Grimmond and T. R. Oke, "Aerodynamic properties of urban areas derived from analysis of surface form," *Journal of applied meteorology*, vol. 38, no. 9, pp. 1262–1292, 1999.

[38] A. Hagishima, J. Tanimoto, K. Nagayama, and S. Meno, "Aerodynamic parameters of regular arrays of rectangular blocks with various geometries," *Boundary-Layer Meteorology*, vol. 132, no. 2, pp. 315–337, 2009.

[39] D. Hamlyn, T. Hilderman, and R. Britter, "A simple network approach to modelling dispersion among large groups of obstacles," *Atmospheric Environment*, vol. 41, no. 28, pp. 5848–5862, 2007.

[40] K. Harikrishnan, R. Misra, G. Ambika, and R. Amritkar, "Computing the multifractal spectrum from time series: an algorithmic approach," *Chaos: An Interdisciplinary Journal of Nonlinear Science*, vol. 19, no. 4, p. 043129, 2009.

[41] D. E. Holland, J. A. Berglund, J. P. Spruce, and R. D. McKellip, "Derivation of effective aerodynamic surface roughness in urban areas from airborne lidar terrain data," *Journal of Applied Meteorology and Climatology*, vol. 47, no. 10, pp. 2614–2626, 2008.

[42] M. W. Horner, "A multi-scale analysis of urban form and commuting change in a small metropolitan area (1990–2000)," *The Annals of Regional Science*, vol. 41, no. 2, pp. 315–332, 2007.

[43] I. Hosokawa and K. Yamamoto, "Evidence against the kolmogorov refined similarity hypothesis," *Physics of Fluids A: Fluid Dynamics*, vol. 4, no. 3, pp. 457–459, 1992.

[44] W. Huang, J. Tan, H. Kan, N. Zhao, W. Song, G. Song, G. Chen, L. Jiang, C. Jiang, R. Chen *et al.*, "Visibility, air quality and daily mortality in shanghai, china," *Science of the Total Environment*, vol. 407, no. 10, pp. 3295–3300, 2009.

[45] L. Hudgins, C. A. Friehe, and M. E. Mayer, "Wavelet transforms and atmopsheric turbulence," *Physical Review Letters*, vol. 71, no. 20, p. 3279, 1993.

[46] D. Hurst and J. Vassilicos, "Scalings and decay of fractal-generated turbulence," *Physics of Fluids*, vol. 19, no. 3, p. 035103, 2007.

[47] Y. Jia, B. Sill, and T. Reinhold, "Effects of surface roughness element spacing on boundary-layer velocity profile parameters," *Journal of wind engineering and industrial aerodynamics*, vol. 73, no. 3, pp. 215–230, 1998.

[48] B. Josso, D. R. Burton, and M. J. Lalor, "Wavelet strategy for surface roughness analysis and characterisation," *Computer methods in applied mechanics and engineering*, vol. 191, no. 8, pp. 829–842, 2001.

[49] G. Kaiser, *A friendly guide to wavelets*. Springer Science & Business Media, 2010.

[50] M. Kanakidou, N. Mihalopoulos, T. Kindap, U. Im, M. Vrekoussis, E. Gerasopoulos, E. Dermitzaki, A. Unal, M. Koçak, K. Markakis *et al.*, "Megacities as hot spots of air pollution in the east mediterranean," *Atmospheric Environment*, vol. 45, no. 6, pp. 1223–1235, 2011.

[51] J. W. Kantelhardt, S. A. Zschiegner, E. Koscielny-Bunde, S. Havlin, A. Bunde, and H. E. Stanley, "Multifractal detrended fluctuation analysis of nonstationary time series," *Physica A: Statistical Mechanics and its Applications*, vol. 316, no. 1, pp. 87–114, 2002.

[52] P. Kastner-Klein and M. W. Rotach, "Mean flow and turbulence characteristics in an urban roughness sublayer," *Boundary-Layer Meteorology*, vol. 111, no. 1, pp. 55–84, 2004.

[53] ——, "Mean flow and turbulence characteristics in an urban roughness sublayer," *Boundary-Layer Meteorology*, vol. 111, no. 1, pp. 55–84, 2004.

[54] R. G. Kavasseri and R. Nagarajan, "A multifractal description of wind speed records," *Chaos, Solitons & Fractals*, vol. 24, no. 1, pp. 165–173, 2005.

[55] N. Kitova, K. Ivanova, M. Ausloos, T. Ackerman, and M. Mikhalev, "Time dependent correlations in marine stratocumulus cloud base height records," *International Journal of Modern Physics C*, vol. 13, no. 02, pp. 217–227, 2002.

[56] E. Koscielny-Bunde, A. Bunde, S. Havlin, and Y. Goldreich, "Analysis of daily temperature fluctuations," *Physica A: Statistical Mechanics and its Applications*, vol. 231, no. 4, pp. 393–396, 1996.

[57] E. Koscielny-Bunde, A. Bunde, S. Havlin, H. E. Roman, Y. Goldreich, and H.-J. Schellnhuber, "Indication of a universal persistence law governing atmospheric variability," *Physical Review Letters*, vol. 81, no. 3, p. 729, 1998.

[58] P. Kumar and B. Imam, "Footprints of air pollution and changing environment on the sustainability of built infrastructure," *Science of the Total Environment*, vol. 444, pp. 85–101, 2013.

[59] P. Kumar and L. Morawska, "Recycling concrete: an undiscovered source of ultrafine particles," *Atmospheric environment*, vol. 90, pp. 51–58, 2014.

[60] D. S. Lemons and P. Langevin, *An introduction to stochastic processes in physics*. JHU Press, 2002.

[61] G. Lin and Z. Fu, "A universal model to characterize different multi-fractal behaviors of daily temperature records over china," *Physica A: Statistical Mechanics and its Applications*, vol. 387, no. 2, pp. 573–579, 2008.

[62] J. L. López and J. G. Contreras, "Performance of multifractal detrended fluctuation analysis on short time series," *Physical Review E*, vol. 87, no. 2, p. 022918, 2013.

[63] R. Macdonald, R. Griffiths, and D. Hall, "An improved method for the estimation of surface roughness of obstacle arrays," *Atmospheric environment*, vol. 32, no. 11, pp. 1857–1864, 1998.

[64] S. Mallat, *A wavelet tour of signal processing: the sparse way*. Academic press, 2008.

[65] S. Mallat and W. L. Hwang, "Singularity detection and processing with wavelets," *IEEE transactions on information theory*, vol. 38, no. 2, pp. 617–643, 1992.

[66] B. B. Mandelbrot, "Intermittent turbulence in self-similar cascades: divergence of high moments and dimension of the carrier," in *Multifractals and 1/ Noise*. Springer, 1999, pp. 317–357.

[67] A. Martilli and J. L. Santiago, "Cfd simulation of airflow over a regular array of cubes. part ii: analysis of spatial average properties," *Boundary-layer meteorology*, vol. 122, no. 3, pp. 635–654, 2007.

[68] MATLAB, *version 8.3 (R2014a)*. Natick, Massachusetts: The MathWorks Inc., 2014.

[69] C. Meneveau and K. Sreenivasan, "The multifractal spectrum of the dissipation field in turbulent flows," *Nuclear Physics B-Proceedings Supplements*, vol. 2, pp. 49–76, 1987.

[70] Y. Meyer, *Wavelets and operators*. Cambridge University Press, 1995, vol. 1.

[71] J. Millward-Hopkins, A. Tomlin, L. Ma, D. Ingham, and M. Pourkashanian, "Aerodynamic parameters of a uk city derived from morphological data," *Boundary-layer meteorology*, pp. 1–22, 2013.

[72] ——, "Aerodynamic parameters of a uk city derived from morphological data," *Boundary-layer meteorology*, pp. 1–22, 2013.

[73] A. Monin and A. Obukhov, "Basic laws of turbulent mixing in the surface layer of the atmosphere," *Contrib. Geophys. Inst. Acad. Sci. USSR*, vol. 151, no. 163, p. e187, 1954.

[74] P. Mouzourides, A. Kyprianou, and M.-A. Neophytou, "A scale-adaptive approach for spatially-varying urban morphology characterization in boundary layer parametrization using multi-resolution analysis," *Boundary-layer meteorology*, vol. 149, no. 3, pp. 455–481, 2013.

[75] J.-F. Muzy, E. Bacry, and A. Arneodo, "Wavelets and multifractal formalism for singular signals: Application to turbulence data," *Physical review letters*, vol. 67, no. 25, p. 3515, 1991.

[76] M. Neophytou, P. Fokaides, I. Panagiotou, I. Ioannou, M. Petrou, M. Sandberg, H. Wigo, E. Linden, E. Batchvarova, P. Videnov *et al.*, "Towards optimization of urban planning and architectural parameters for energy use minimization in mediterranean cities," in *World Renewable Energy Congress-Sweden; 8-13 May; 2011; Linköping; Sweden*, no. 057. Linköping University Electronic Press, 2011, pp. 3372–3379.

[77] M. K. Neophytou and R. E. Britter, "Modelling the wind flow in complex urban topographies: a computational-fluid-dynamics simulation of the central london area," in *Proceedings of the Fifth GRACM International Congress on Computational Mechanics, Limassol, Cyprus*, vol. 29, 2005.

[78] M. Neophytou, D. Goussis, M. Van Loon, and E. Mastorakos, "Reduced chemical mechanisms for atmospheric pollution using computational singular perturbation analysis," *Atmospheric Environment*, vol. 38, no. 22, pp. 3661–3673, 2004.

[79] M.-A. Neophytou, C. Markides, and P. Fokaides, "An experimental study of the flow through and over two dimensional rectangular roughness elements: Deductions for urban boundary layer parameterizations and exchange processes," *Physics of Fluids*, vol. 26, no. 8, p. 086603, 2014.

[80] M. Neophytou1&2, D. Goussis, E. Mastorakos, and R. Britter, "The development of a scale-adaptive reactive pollutant dispersion model," 2005.

[81] M. Nicollet, A. Lemarchand, and N. Cavaciuti, "Detection of atmospheric turbulence by multifractal analysis using wavelets," *Fractals*, vol. 12, no. 02, pp. 211–221, 2004.

[82] Y. Nievergelt and Y. Nievergelt, *Wavelets made easy*. Springer, 1999, vol. 174.

[83] T. R. Oke, "Street design and urban canopy layer climate," *Energy and buildings*, vol. 11, no. 1, pp. 103–113, 1988.

[84] I. Orlanski, "A rational subdivision of scales for atmospheric processes," *Bulletin of the American Meteorological Society*, vol. 56, pp. 527–530, 1975.

[85] P. Oświęcimka, J. Kwapień, and S. Drożdż, "Wavelet versus detrended fluctuation analysis of multifractal structures," *Physical Review E*, vol. 74, no. 1, p. 016103, 2006.

[86] I. Panagiotou, M. K.-A. Neophytou, D. Hamlyn, and R. E. Britter, "City breathability as quantified by the exchange velocity and its spatial variation in real inhomogeneous urban geometries: An example from central london urban area," *Science of the Total Environment*, vol. 442, pp. 466–477, 2013.

[87] C. A. Pope III and D. W. Dockery, "Health effects of fine particulate air pollution: lines that connect," *Journal of the air & waste management association*, vol. 56, no. 6, pp. 709–742, 2006.

[88] R Core Team, *R: A Language and Environment for Statistical Computing*, R Foundation for Statistical Computing, Vienna, Austria, 2013. [Online]. Available: http://www.R-project.org/

[89] C. Ratti, S. Di Sabatino, R. Britter, M. Brown, F. Caton, and S. Burian, "Analysis of 3-d urban databases with respect to pollution dispersion for a number of european and american cities," *Water, Air and Soil Pollution: Focus*, vol. 2, no. 5-6, pp. 459–469, 2002.

[90] M. Raupach, "Drag and drag partition on rough surfaces," *Boundary-Layer Meteorology*, vol. 60, no. 4, pp. 375–395, 1992.

[91] ——, "Simplified expressions for vegetation roughness length and zero-plane displacement as functions of canopy height and area index," *Boundary-Layer Meteorology*, vol. 71, no. 1, pp. 211–216, 1994.

[92] A. Saffari, N. Daher, C. Samara, D. Voutsa, A. Kouras, E. Manoli, O. Karagkiozidou, C. Vlachokostas, N. Moussiopoulos, M. M. Shafer *et al.*, "Increased biomass burning due to the economic crisis in greece and its adverse impact on wintertime air quality in thessaloniki," *Environmental science & technology*, vol. 47, no. 23, pp. 13 313–13 320, 2013.

[93] F. Salamanca, A. Martilli, M. Tewari, and F. Chen, "A study of the urban boundary layer using different urban parameterizations and high-resolution urban canopy parameters with wrf," *Journal of Applied Meteorology and Climatology*, vol. 50, no. 5, pp. 1107–1128, 2011.

[94] H. Schmid, "Source areas for scalars and scalar fluxes," *Boundary-Layer Meteorology*, vol. 67, no. 3, pp. 293–318, 1994.

[95] H. Schmid and T. Oke, "A model to estimate the source area contributing to turbulent exchange in the surface layer over patchy terrain," *Quarterly Journal of the Royal Meteorological Society*, vol. 116, no. 494, pp. 965–988, 1990.

[96] K. Schneider and M. Farge, "Wavelets: Mathematical theory," *Encyclopedia of Mathematics Physics*, pp. 426–438, 2006.

[97] M. R. Schroeder, *Fractals, chaos, power laws: Minutes from an infinite paradise*. Courier Corporation, 2012.

[98] J. H. Seinfeld, S. N. Pandis, and K. Noone, *Atmospheric chemistry and physics: from air pollution to climate change*. AIP, 1998.

[99] Y. Shao and Y. Yang, "A scheme for drag partition over rough surfaces," *Atmospheric Environment*, vol. 39, no. 38, pp. 7351–7361, 2005.

[100] E. Solazzo, S. Di Sabatino, N. Aquilina, A. Dudek, and R. Britter, "Coupling mesoscale modelling with a simple urban model: the lisbon case study," *Boundary-layer meteorology*, vol. 137, no. 3, pp. 441–457, 2010.

[101] I. D. Stewart and T. R. Oke, "Local climate zones for urban temperature studies," *Bulletin of the American Meteorological Society*, vol. 93, no. 12, pp. 1879–1900, 2012.

[102] R. B. Stull, *An introduction to boundary layer meteorology*. Springer Science & Business Media, 2012, vol. 13.

[103] P. Talkner and R. O. Weber, "Power spectrum and detrended fluctuation analysis: Application to daily temperatures," *Physical Review E*, vol. 62, no. 1, p. 150, 2000.

[104] G. I. Taylor, "Statistical theory of turbulence," in *Proceedings of the Royal Society of London A: Mathematical, Physical and Engineering Sciences*, vol. 151, no. 873. The Royal Society, 1935, pp. 421–444.

[105] H. Tennekes and J. L. Lumley, *A first course in turbulence*. MIT press, 1972.

[106] S. Thoroddsen and C. Van Atta, "Experimental evidence supporting kolmogorovs refined similarity hypothesis," *Physics of Fluids A: Fluid Dynamics*, vol. 4, no. 12, pp. 2592–2594, 1992.

[107] W. Tian, A. Rysanek, R. Choudhary, and Y. Heo, "High resolution energy simulations at city scale," in *14th International Conference of IBPSA-Building Simulation 2015, BS 2015, Conference Proceedings*, 2015, pp. 239–246.

[108] A. Tiwary and P. Kumar, "Impact evaluation of green–grey infrastructure interaction on built-space integrity: an emerging perspective to urban ecosystem service," *Science of the Total Environment*, vol. 487, pp. 350–360, 2014.

[109] C. Torrence and G. P. Compo, "A practical guide to wavelet analysis," *Bulletin of the American Meteorological society*, vol. 79, no. 1, pp. 61–78, 1998.

[110] E. Vannier, A. Gademer, and V. Ciarletti, "A new approach for roughness analysis of soil surfaces," in *Signal Processing Conference, 2006 14th European*. IEEE, 2006, pp. 1–4.

[111] C. A. Varotsos, I. Melnikova, M. N. Efstathiou, and C. Tzanis, "1/f noise in the uv solar spectral irradiance," *Theoretical and applied climatology*, vol. 111, no. 3-4, pp. 641–648, 2013.

[112] W. W. Wu-Shyong, *Time series analysis: univariate and multivariate methods*. USA, Pearson Addison Wesley, Second edition, 2006.

[113] Y. Xue, W. Pan, W.-Z. Lu, and H.-D. He, "Multifractal nature of particulate matters (pms) in hong kong urban air," *Science of the Total Environment*, vol. 532, pp. 744–751, 2015.

[114] S. A. Zaki, A. Hagishima, J. Tanimoto, and N. Ikegaya, "Aerodynamic parameters of urban building arrays with random geometries," *Boundary-layer meteorology*, vol. 138, no. 1, pp. 99–120, 2011.

Appendix A

MRA deduced results of urban building datasets

A.1 Building attributes

For completeness of the presentation of results, Appendix A presents the MRA deduced results of urban building datasets of European cities (London, Marseille) and North-American cities (New York City, Oklahoma, Phoenix and Seattle).

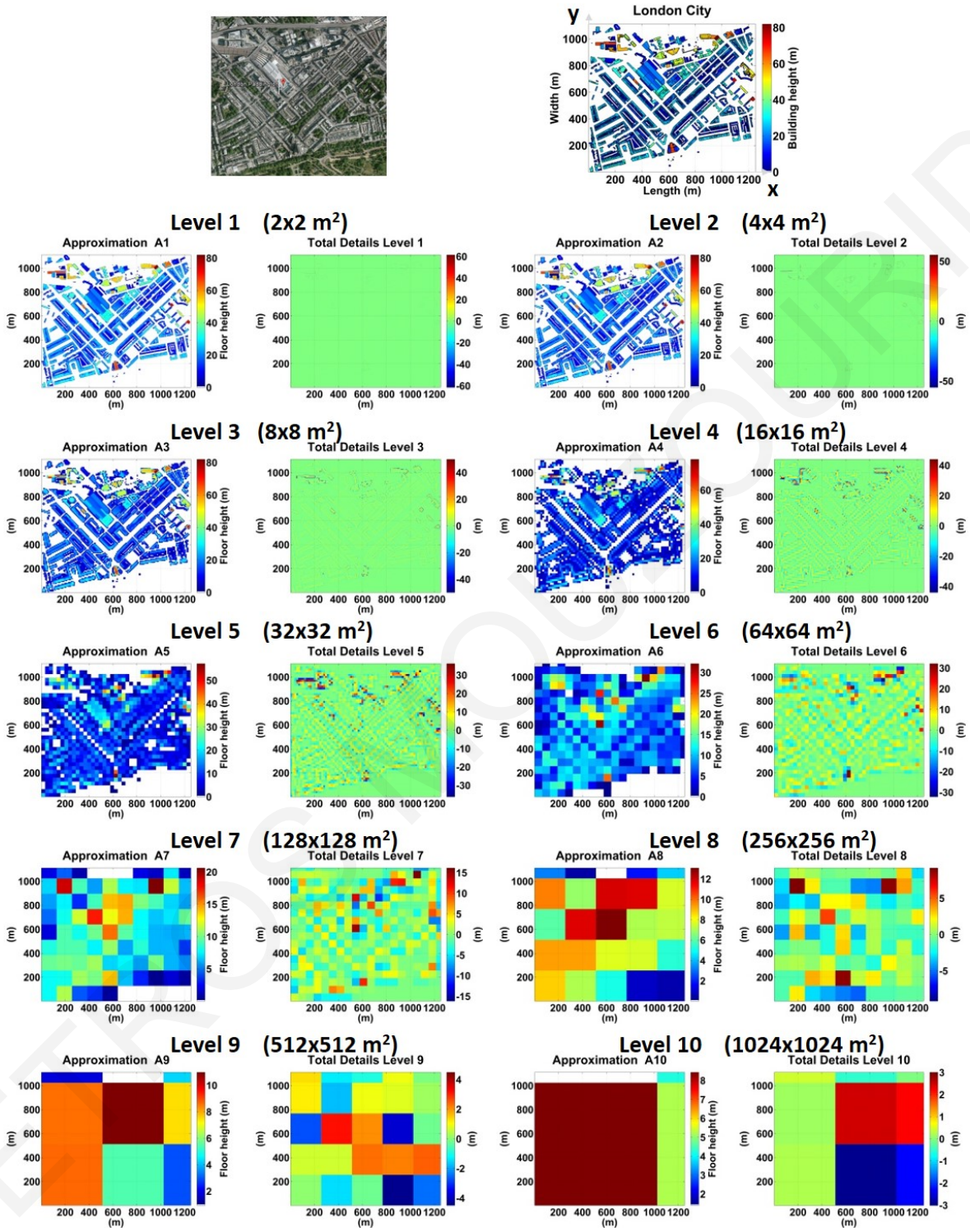

Figure A.1: MRA results of analysis of the 2-D urban building database of London.

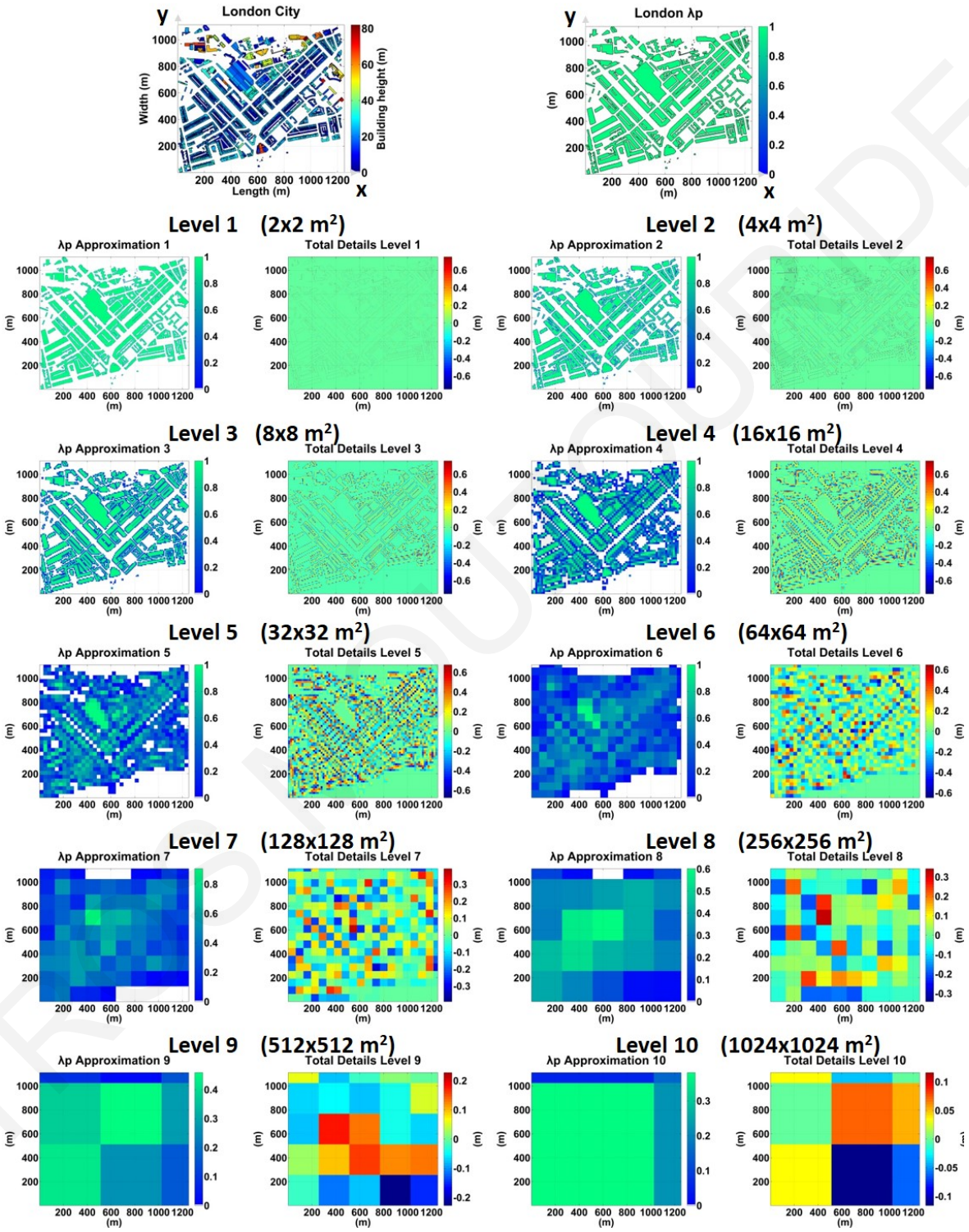

Figure A.2: MRA deduced results of the planar packing density λ_p parameter for the database of London.

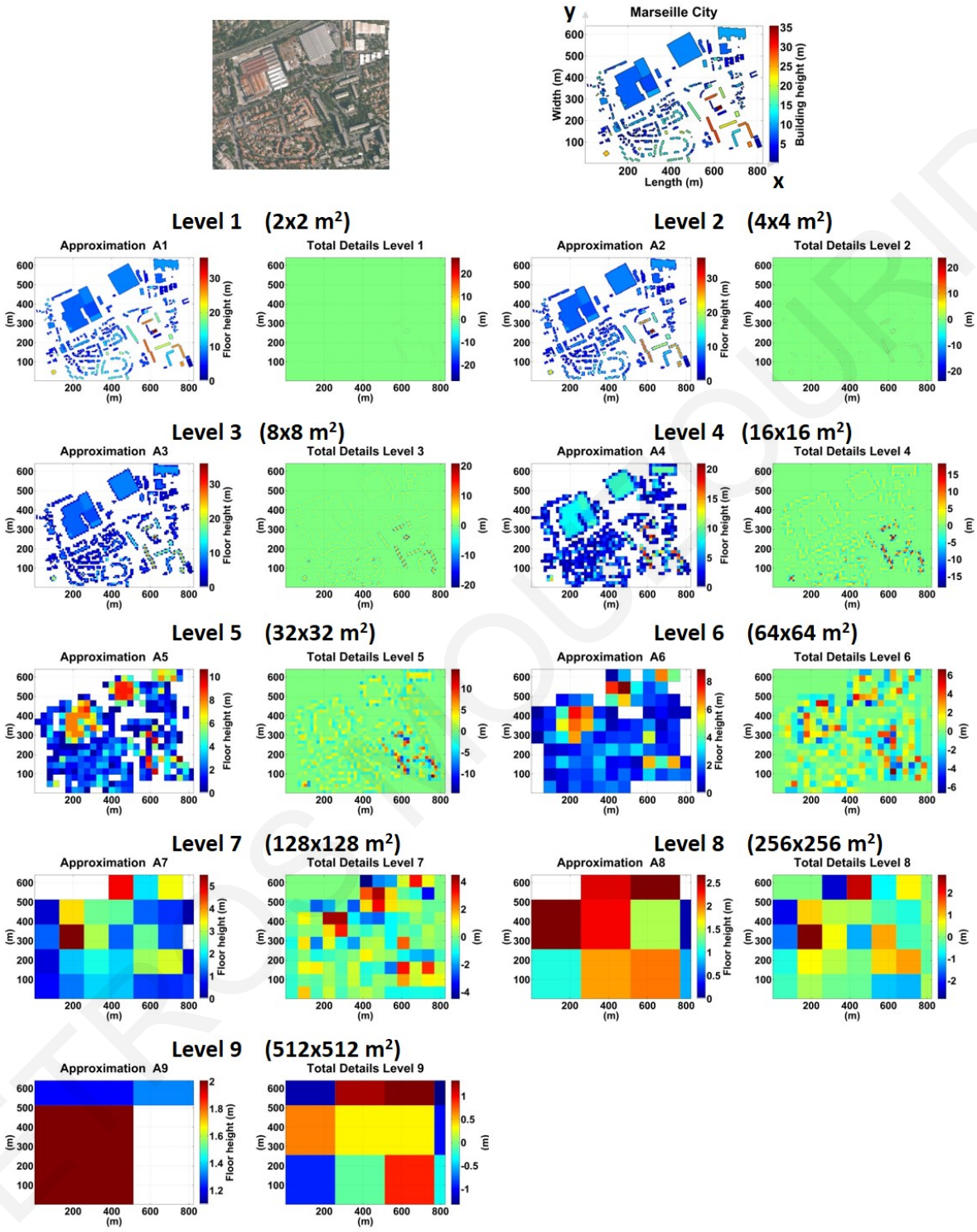

Figure A.3: MRA results of analysis of the 2-D urban building database of Marseille.

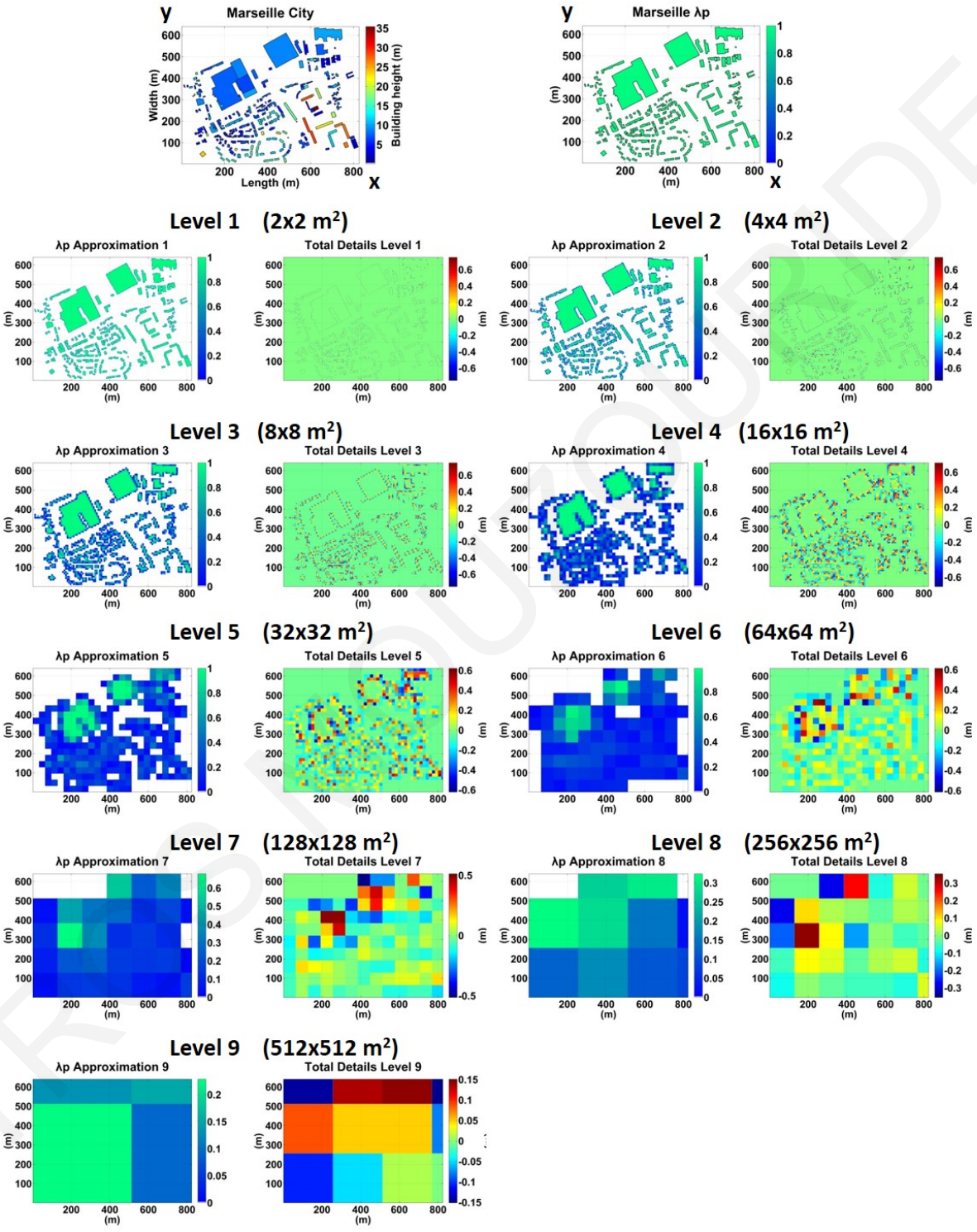

Figure A.4: MRA deduced results of the planar packing density λ_p parameter for the database of Marseille.

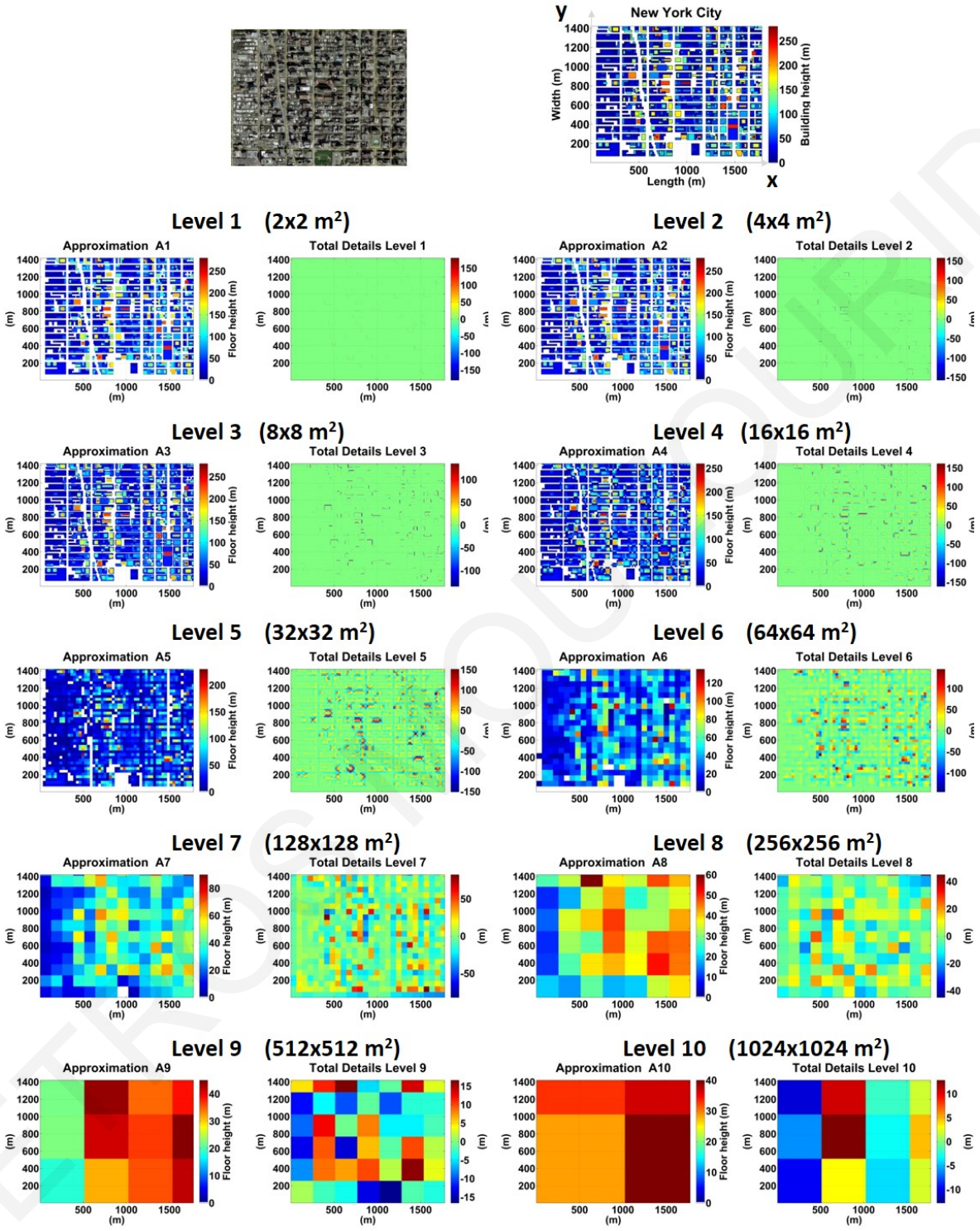

Figure A.5: MRA results of analysis of the 2-D urban building database of New York City.

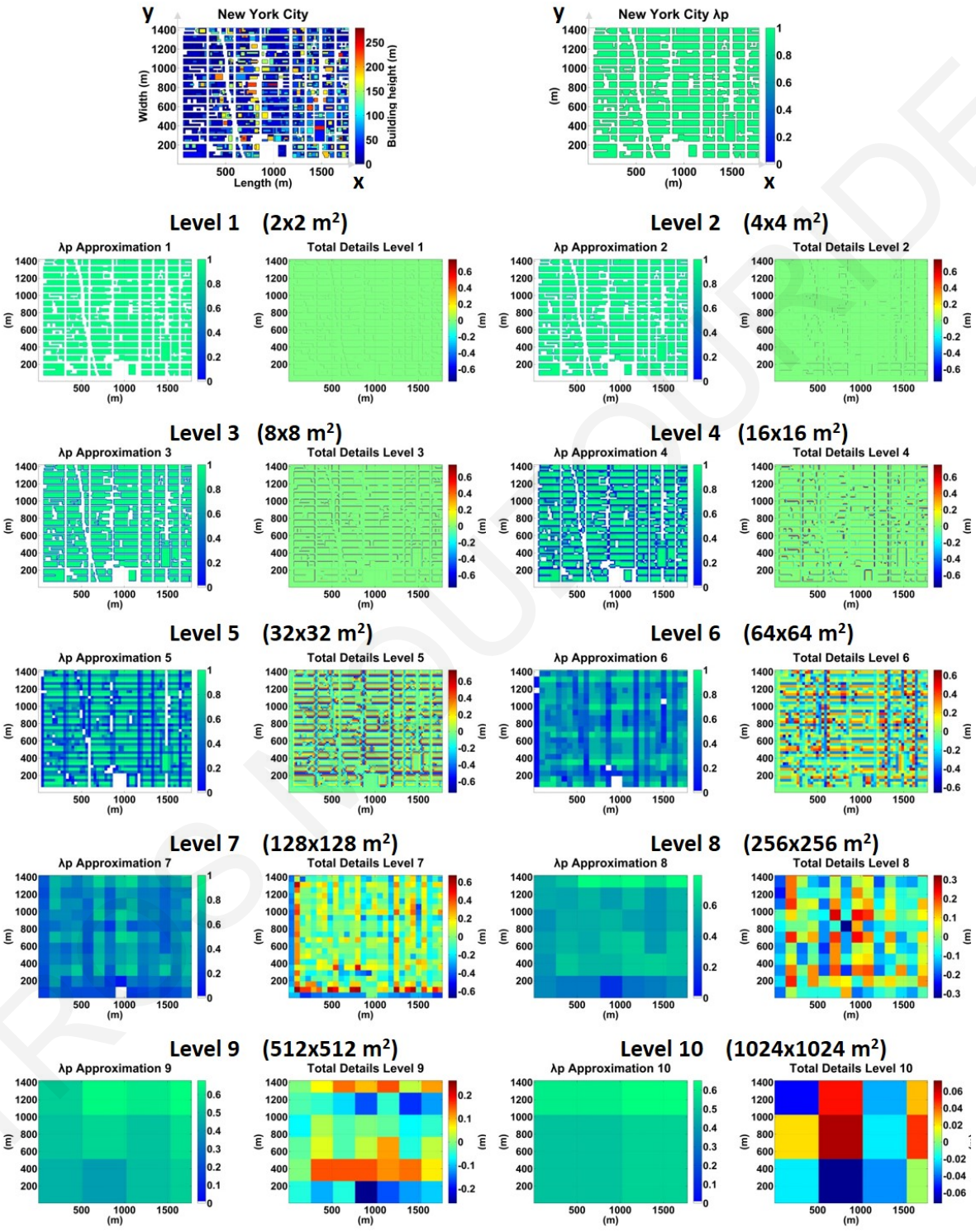

Figure A.6: MRA deduced results of the planar packing density λ_p parameter for the database of New York City.

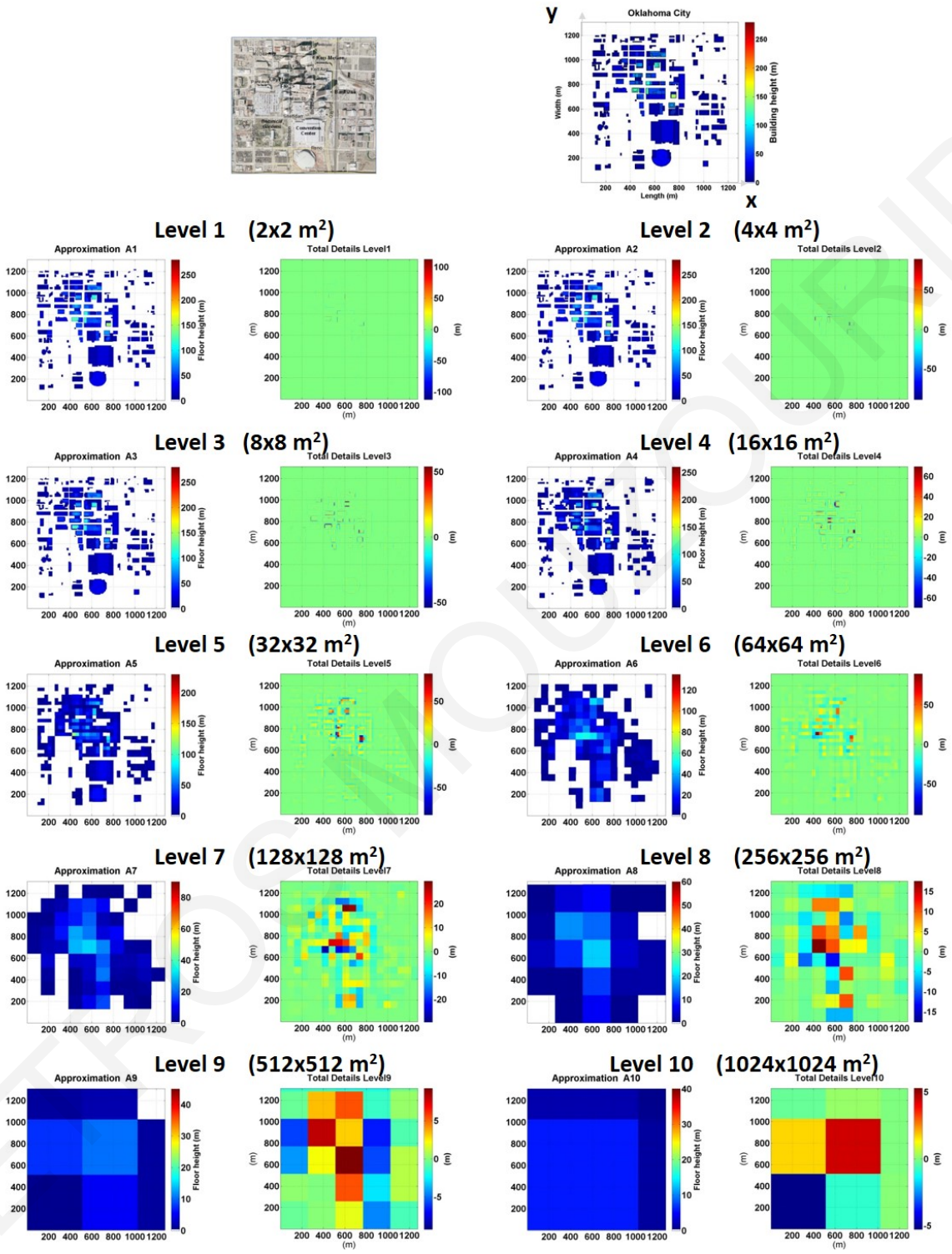

Figure A.7: MRA results of analysis of the 2-D urban building database of Oklahoma.

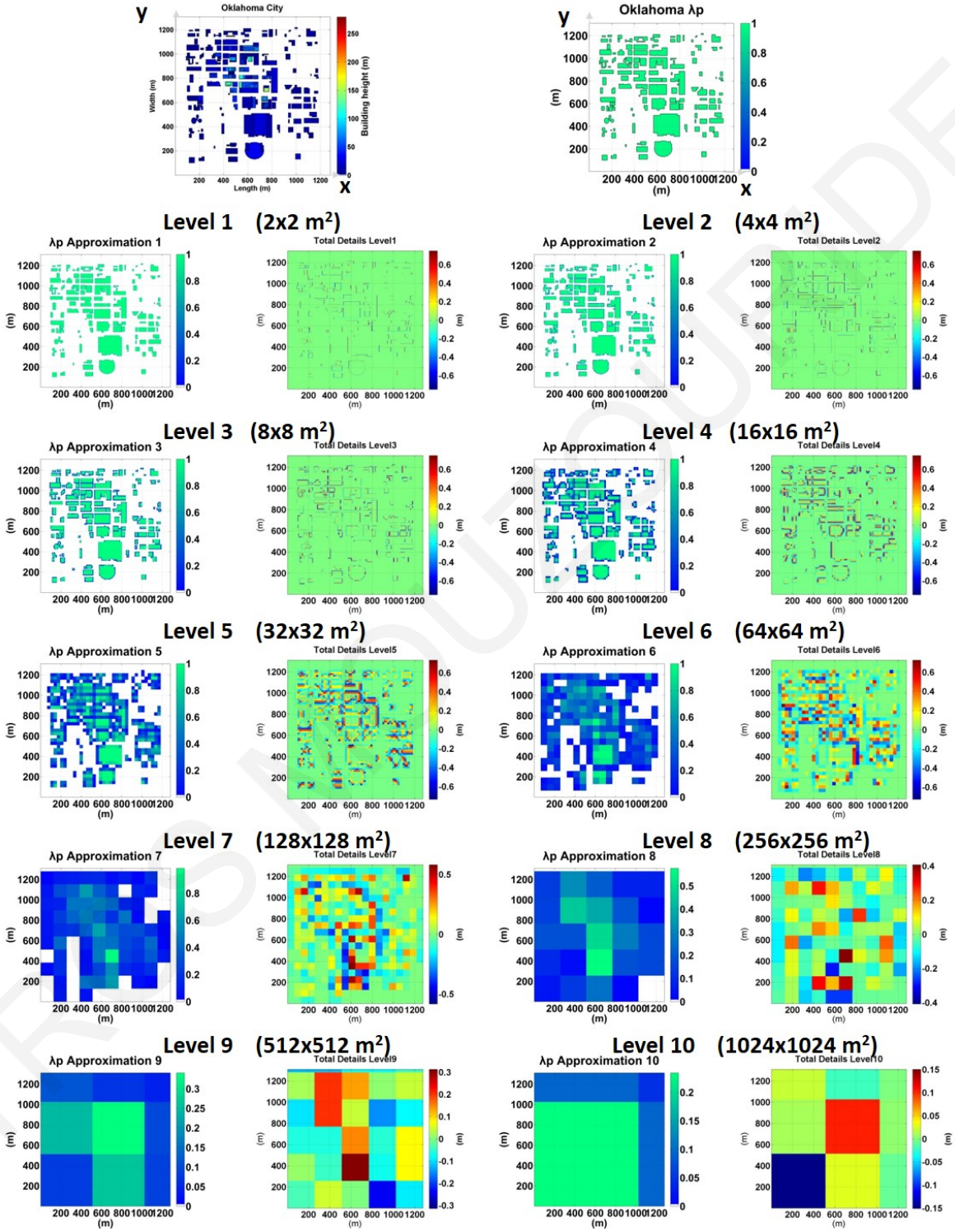

Figure A.8: MRA deduced results of the planar packing density λ_p parameter for the database of Oklahoma.

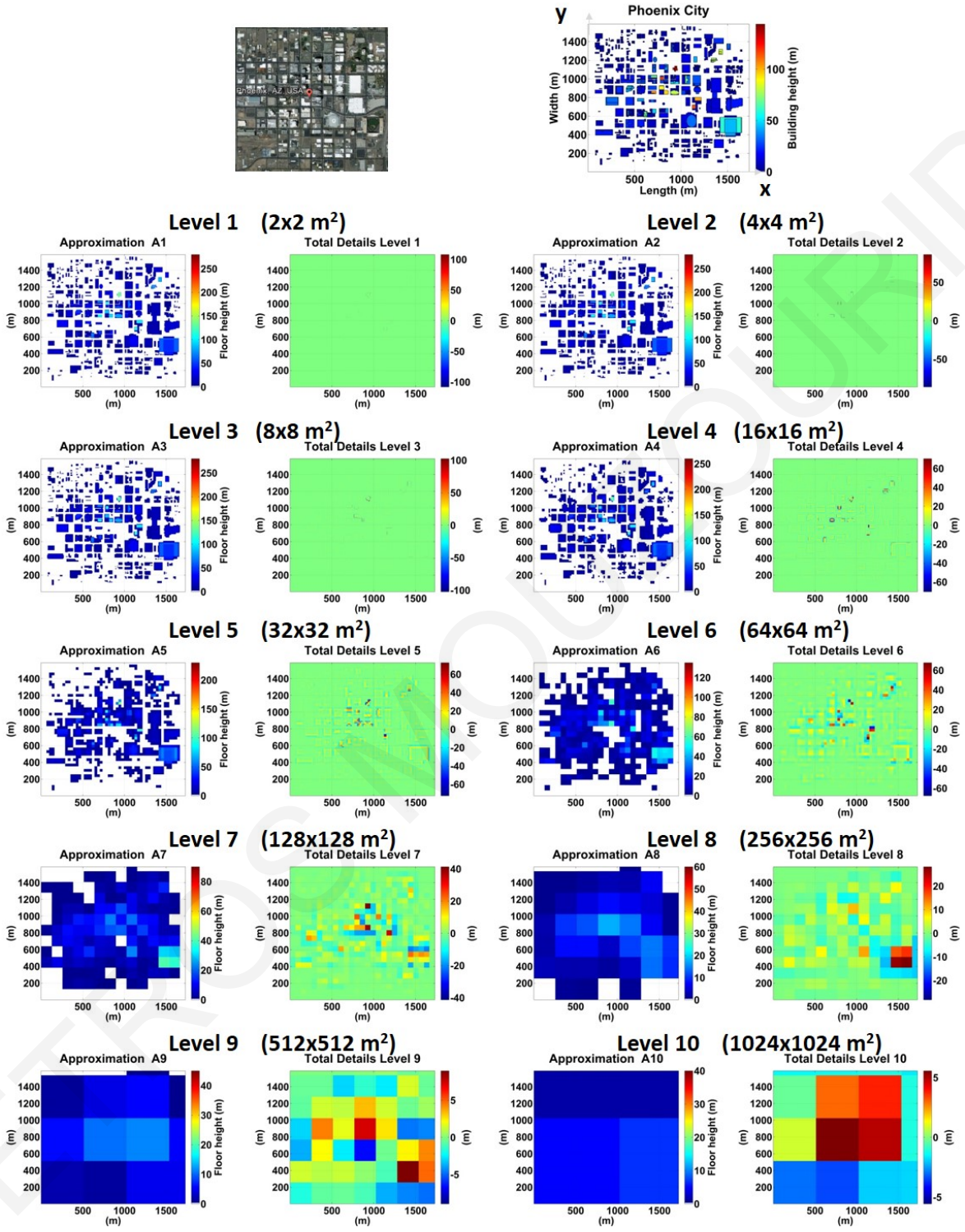

Figure A.9: MRA results of analysis of the 2-D urban building database of Phoenix.

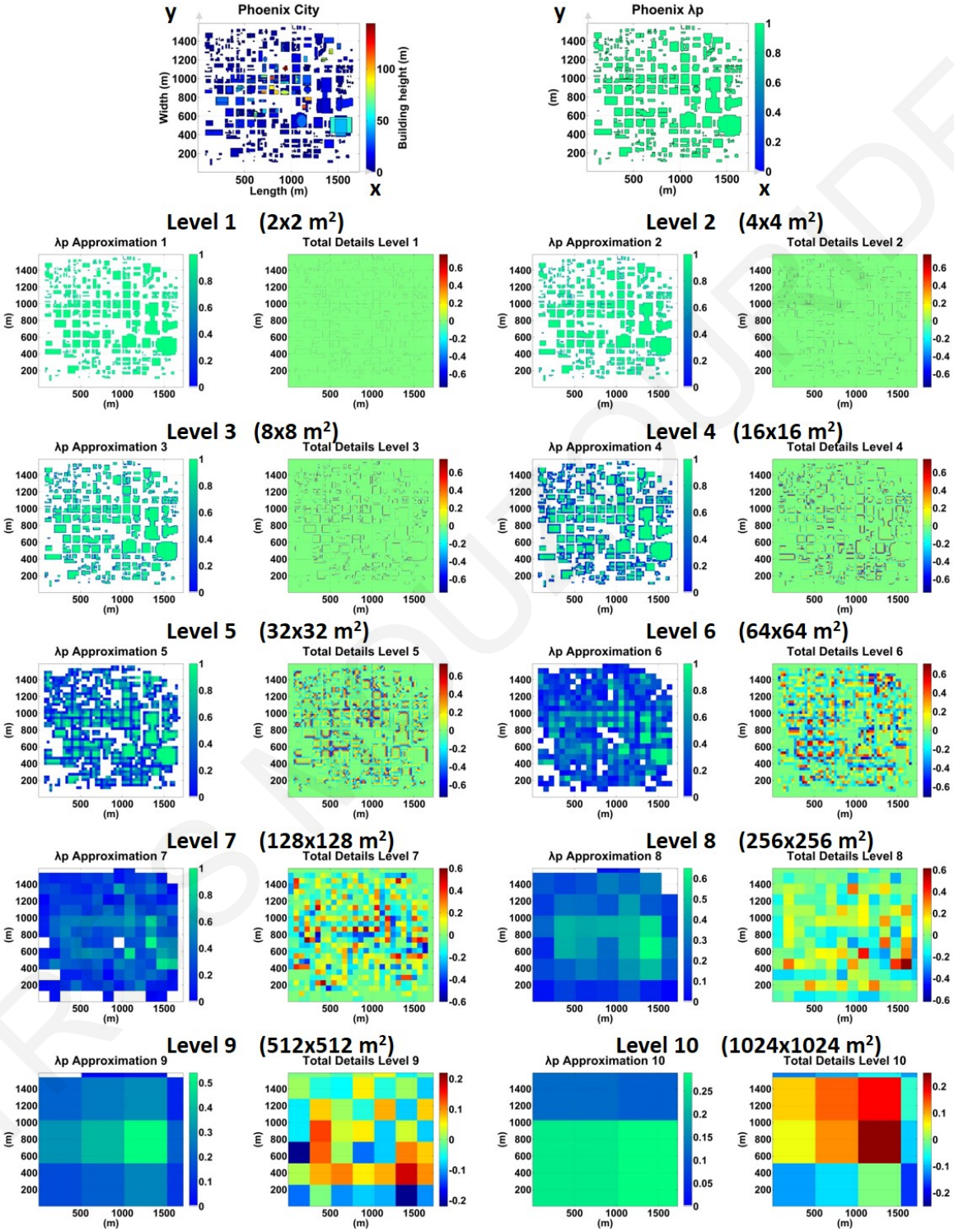

Figure A.10: MRA deduced results of the planar packing density λ_p parameter for the database of Phoenix.

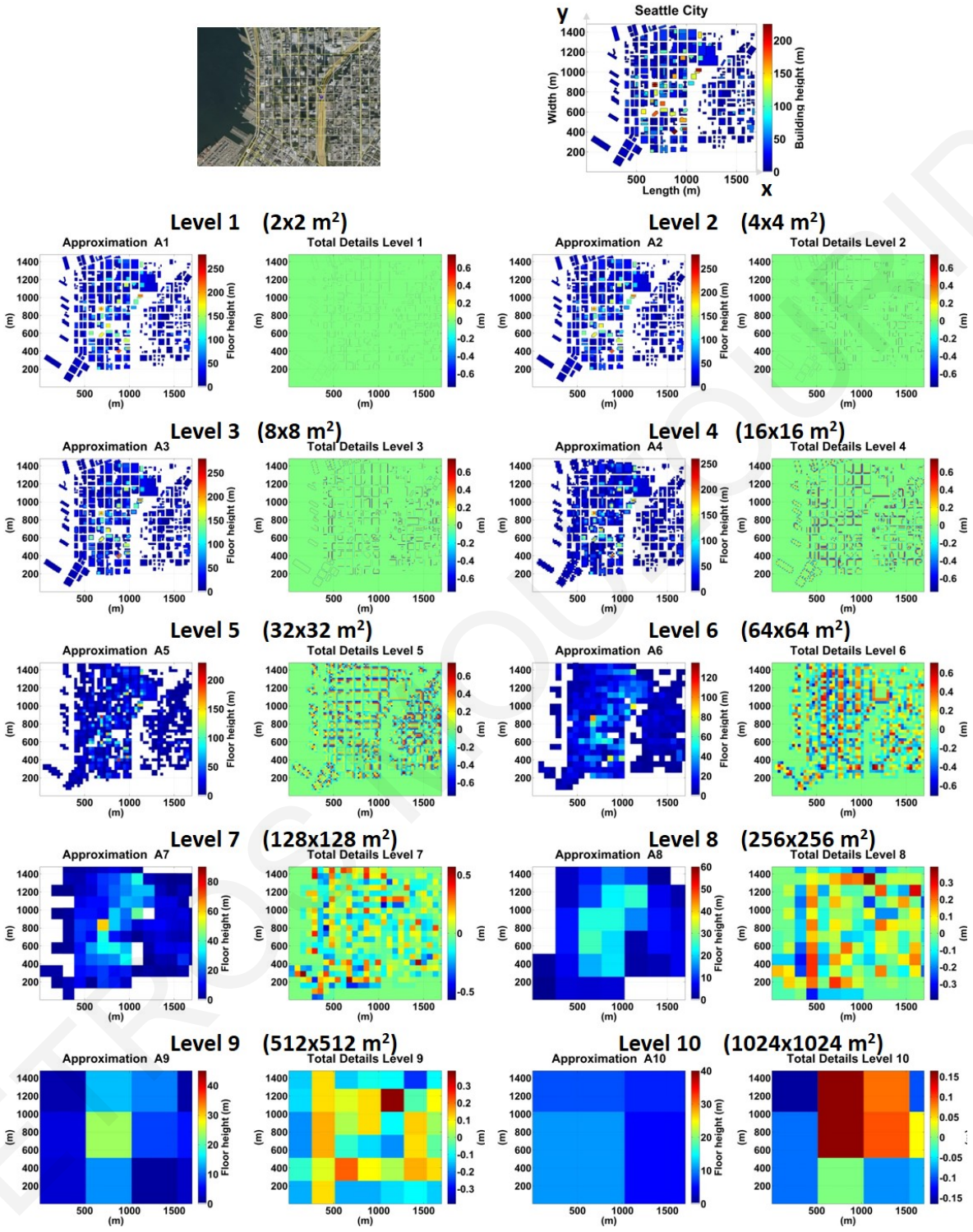

Figure A.11: MRA results of analysis of the 2-D urban building database of Seattle.

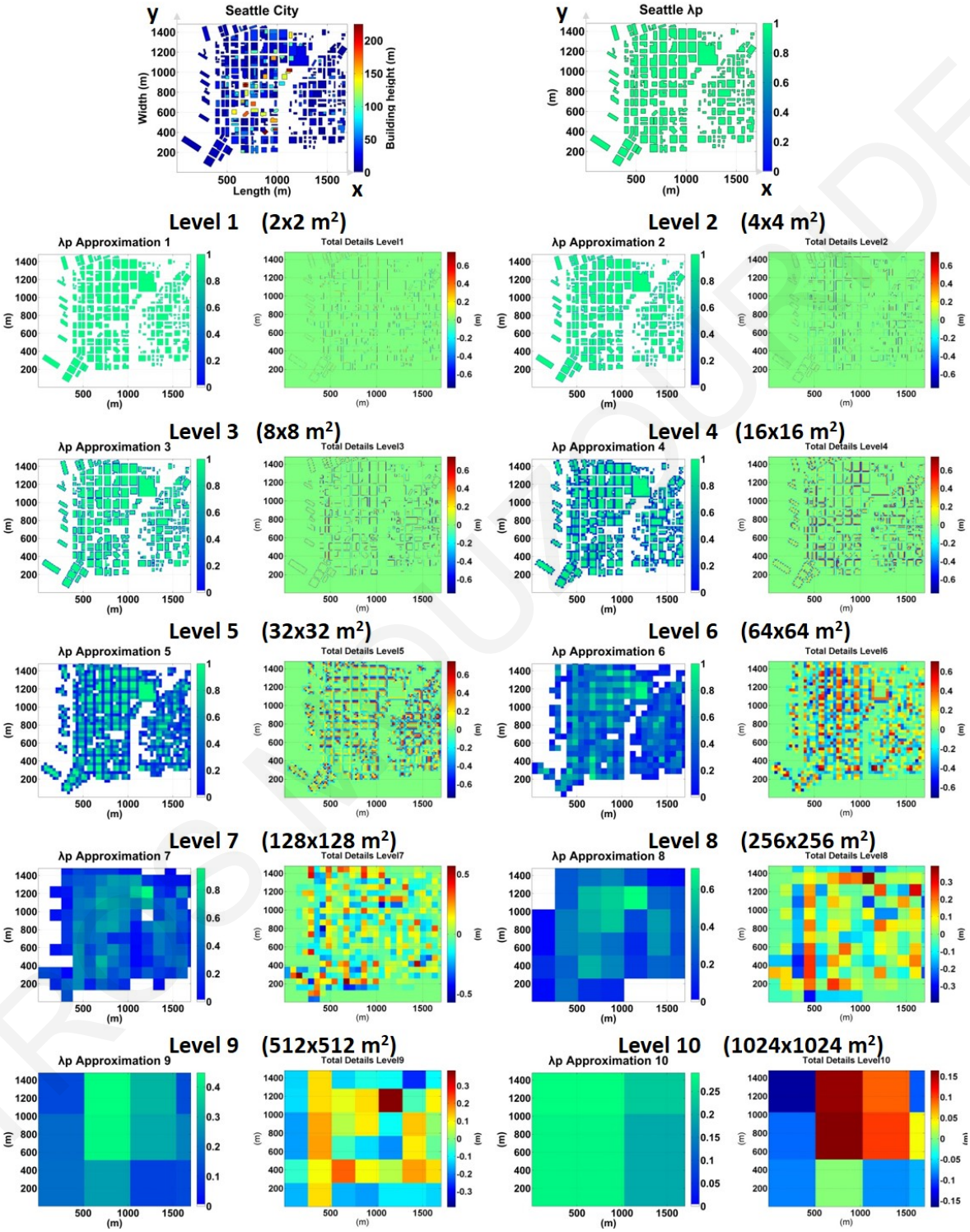

Figure A.12: MRA deduced results of the planar packing density λ_p parameter for the database of Seattle.

Appendix B

Scaler: A standalone GUI for MRA analysis

Appendix B describes the use of the *Scaler*, a user-friendly Graphical User Interface (GUI) tool, which was developed to calculate easily and quickly scale-adaptive and spatially-varying representations of urban information datasets using the MRA.

B.1 General Information

Scaler© is a GUI tool developed to produce rigorously scale-adaptive and spatially-varying representations of urban information datasets using the MRA. *Scaler*© resolves spatial data aggregated at different scales to yield "Approximations" and the subgrid residuals at each and every such scale is retained as "Details". It is freely available tool in WUDAPT Portal for non-profit research purposes. The standalone executable version allows the user to run *Scaler*© without a MATLAB© license and without purchasing extra toolboxes. *Scaler*© is designed to run under Windows 7/10 (32 & 64bit) operating system. Before running the program, it is necessary to install the MATLAB Runtime for R2012a - 32bit (7.17) (`https://www.mathworks.com/products/compiler/mcr/`). The MATLAB Compiler Runtime (MCR) does not require a MATLAB license and can be used to run any MATLAB compiled program on computers which do not have MATLAB installed.

A detailed presentation and discussion of the underlying theory of the Multi-Resolution Analysis (MRA) are given in Chapter 2 and results of MRA in a number of applications are presented in Chapter 5. Further applications of MRA are envisaged through the use and the further tailored development of *Scaler* for the WUDAPT initiative [19].

B.2 Calculation steps

Urban morphology may be in LCZ maps, Google image, CAD or any other "image format" which includes a 3-D information of an urban area. However, urban information data input for *Scaler* is required in the form of a pixilated image (2-D matrix), where the value of each pixel refers to the value of the parameter of interest (e.g. energy demand, building height, packing density etc).

The application menu hosts the following selections:

- Click File > Open and select your file domain based on the MAT-files (*.mat) type.

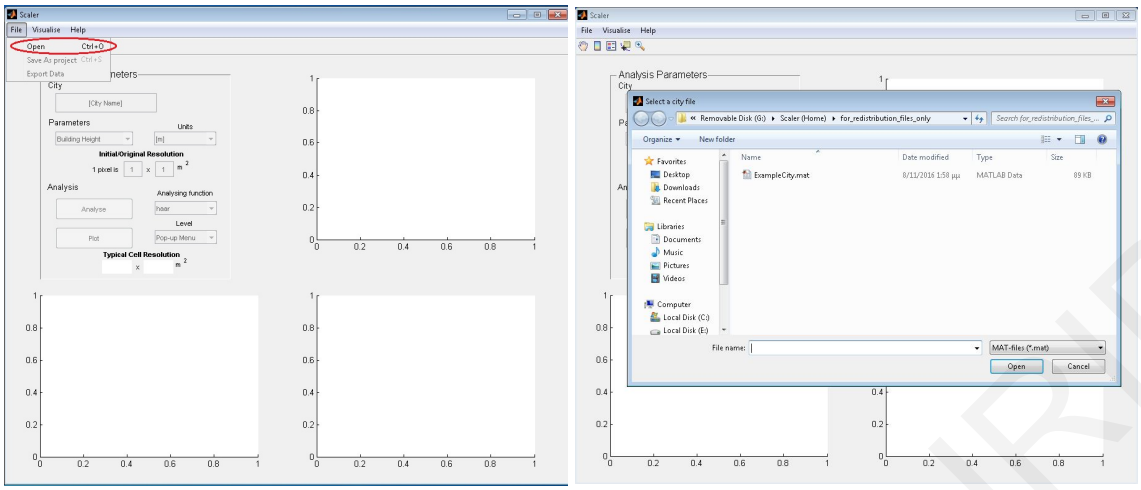

(a) (b)

Figure B.1

- Type the name of the analysing urban dataset on the text field ”[City Name]”.

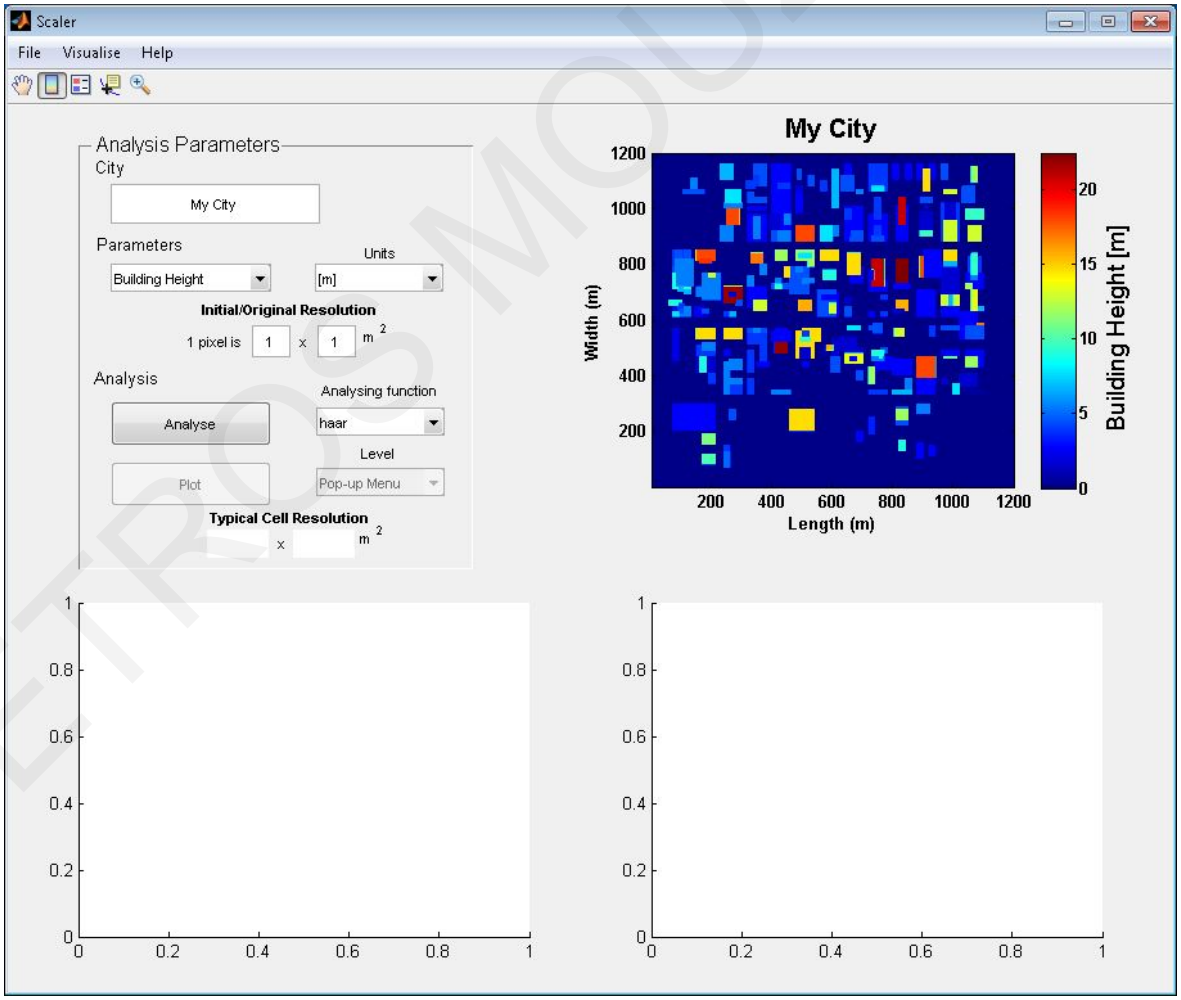

Figure B.2

- Select the analysing parameter. If your analysing parameter is not listed, choose the option and set the new name of your analysing parameter.

- Select the units of your analysing parameter. If the units of your analysing parameter are not listed, choose the option and set the new units of your analysing parameter.

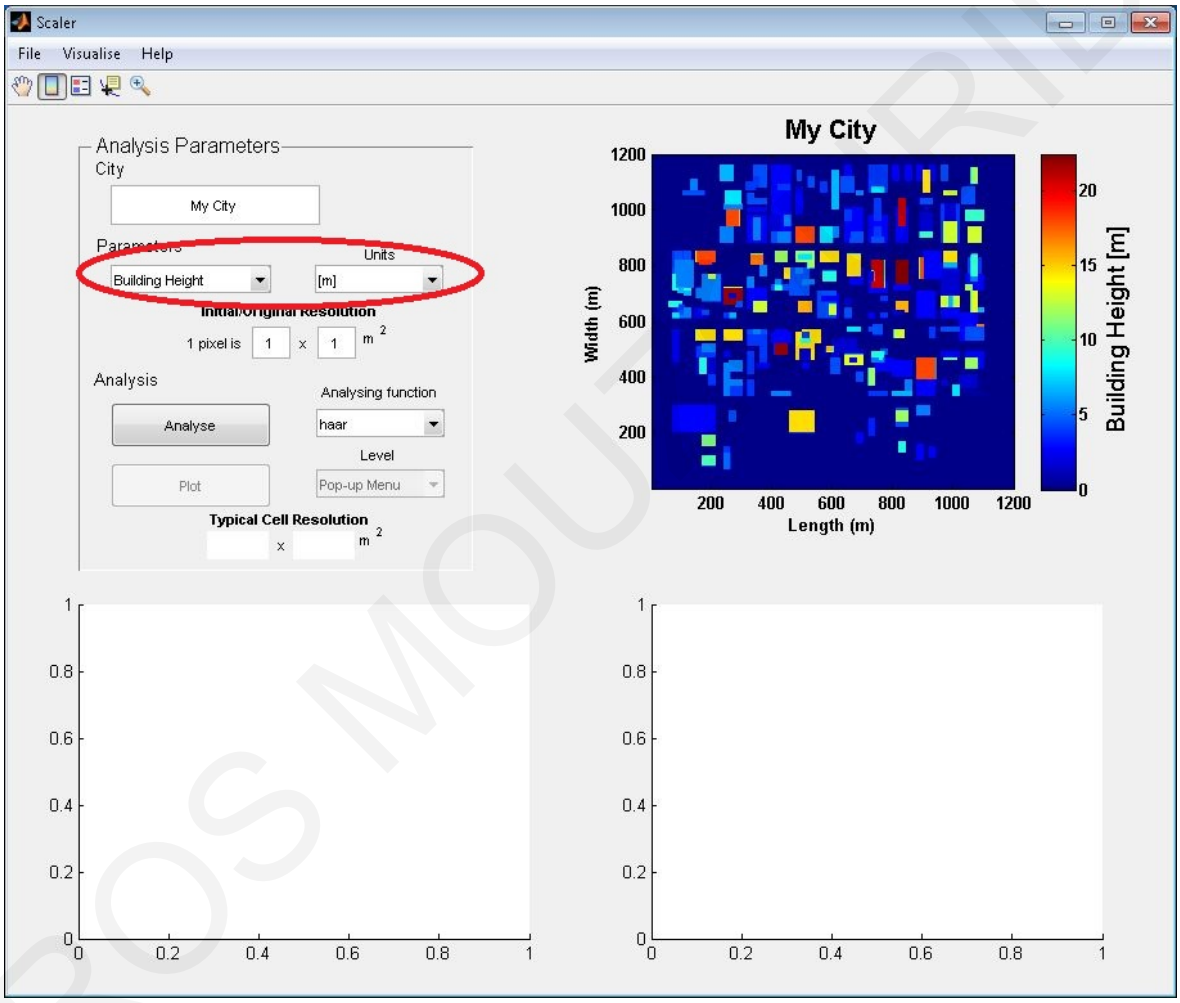

Figure B.3

- Set the accuracy/resolution of the original dataset, namely what is the corresponding physical area of each pixel/cell of dataset. By default, the accuracy/resolution of the dataset is given 1 pixel to $1m \times 1m$ of physical area.

- Select the analysing function to perform the MRA analysis

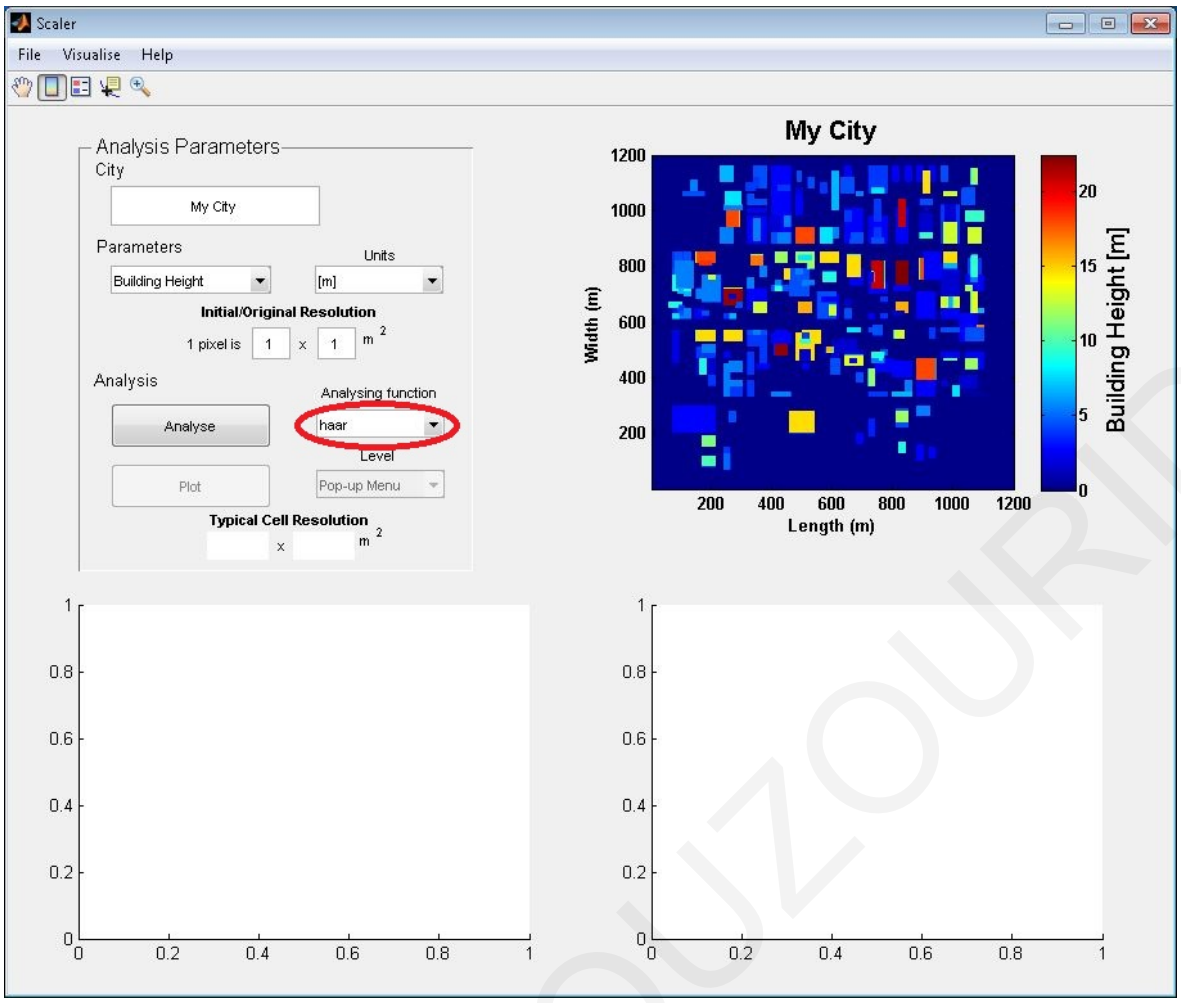

Figure B.4

- Press the ”Analyse” button in order to execute the calculations.

- By default, the lower left image is the Approximation MRA result at the last Level of analysis and the lower right image is the Total Details MRA result at the corresponding Level.

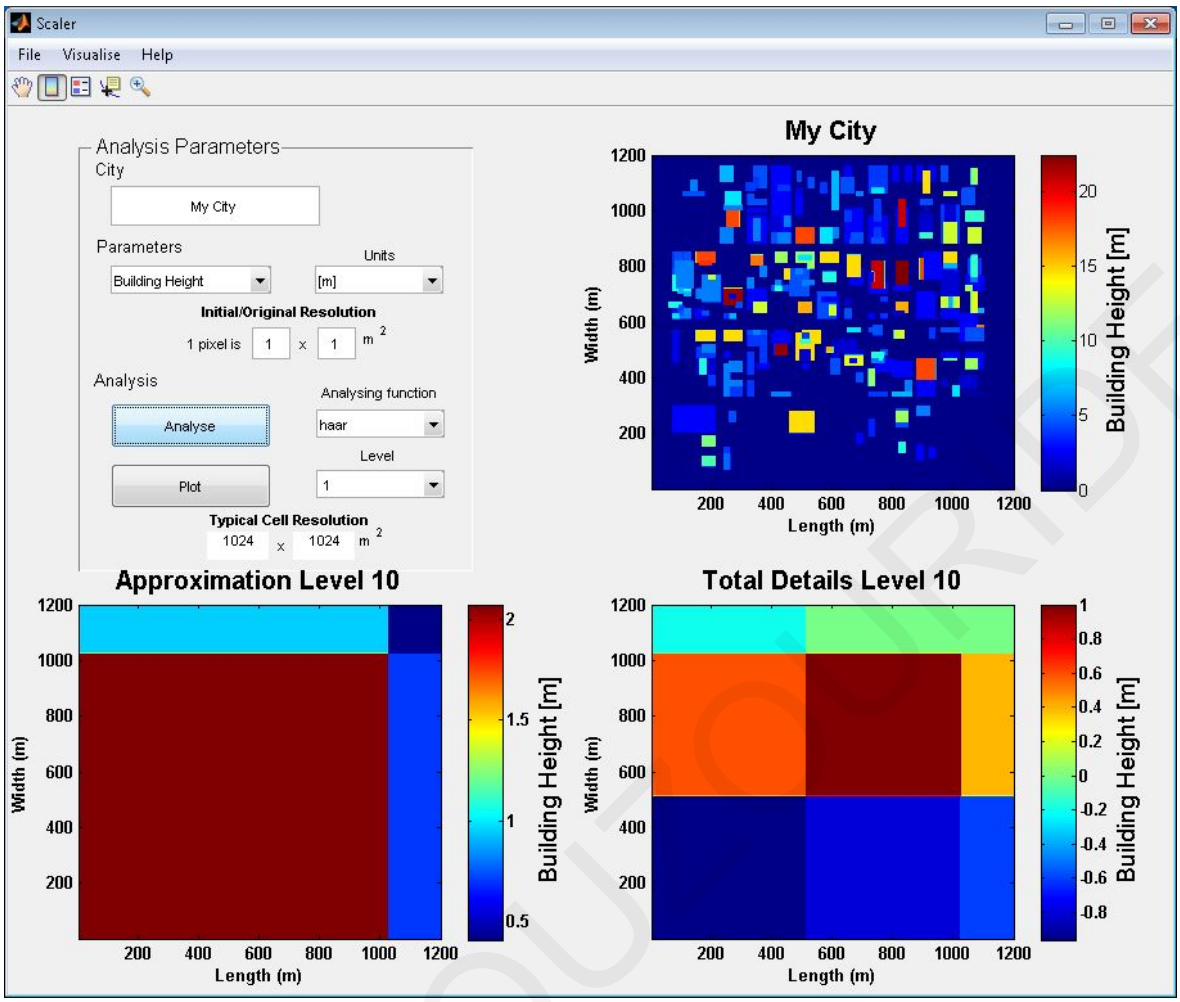

Figure B.5

- Select a number from the Level popup button, to visualise the Approximation and Total Details result at the corresponding Level of analysis.

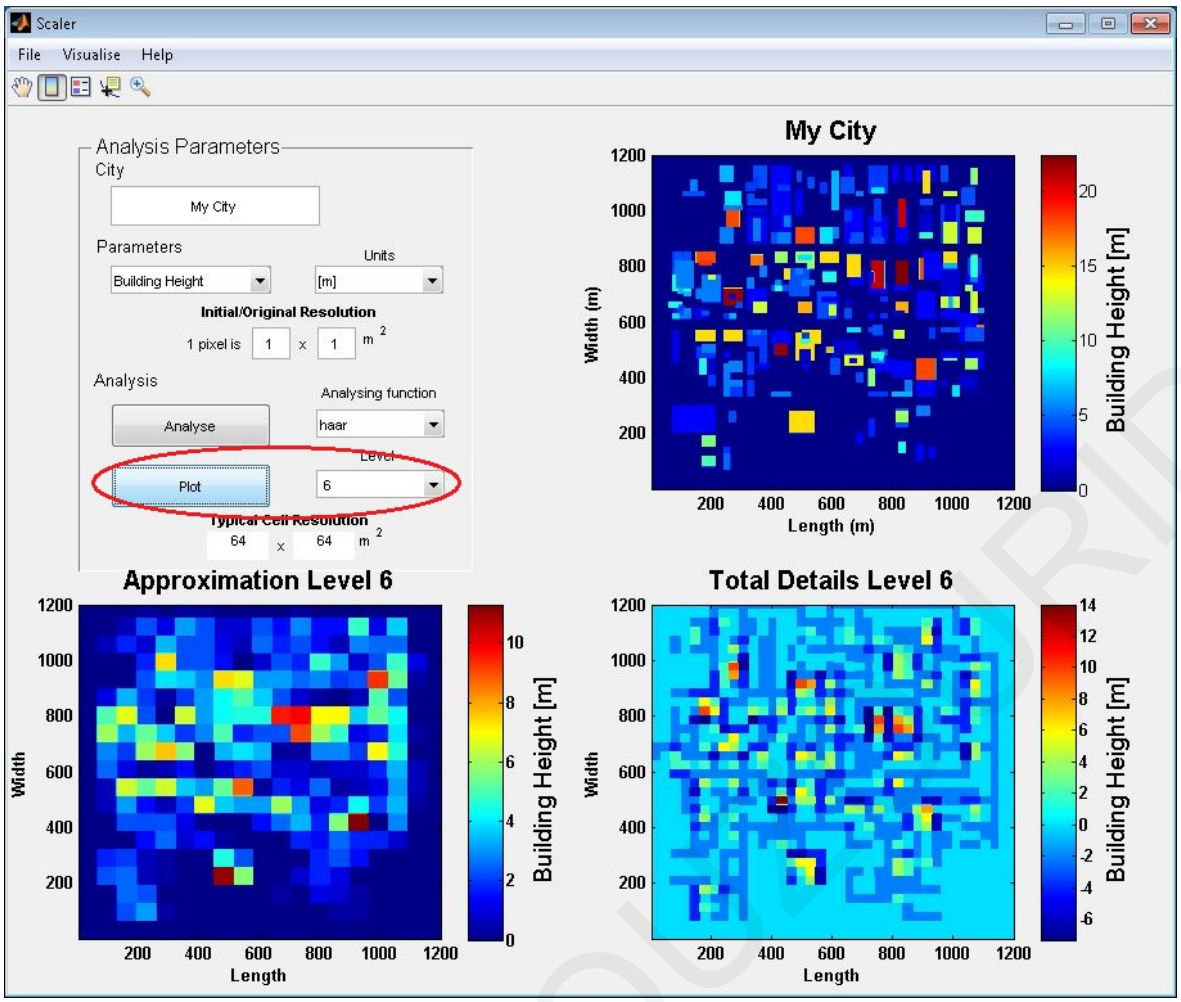

Figure B.6

Click Visualise > Approximation. The application plots (visualises) Approximations up to the last level of analysis.

Click Visualise > Total Details (Single Level). The application plots (visualises) Total Details up to the last level of analysis.

Click Visualise > Cumulative Total Details (All Levels). The application plots (visualises) the cumulative Total Details up to the last level of analysis.

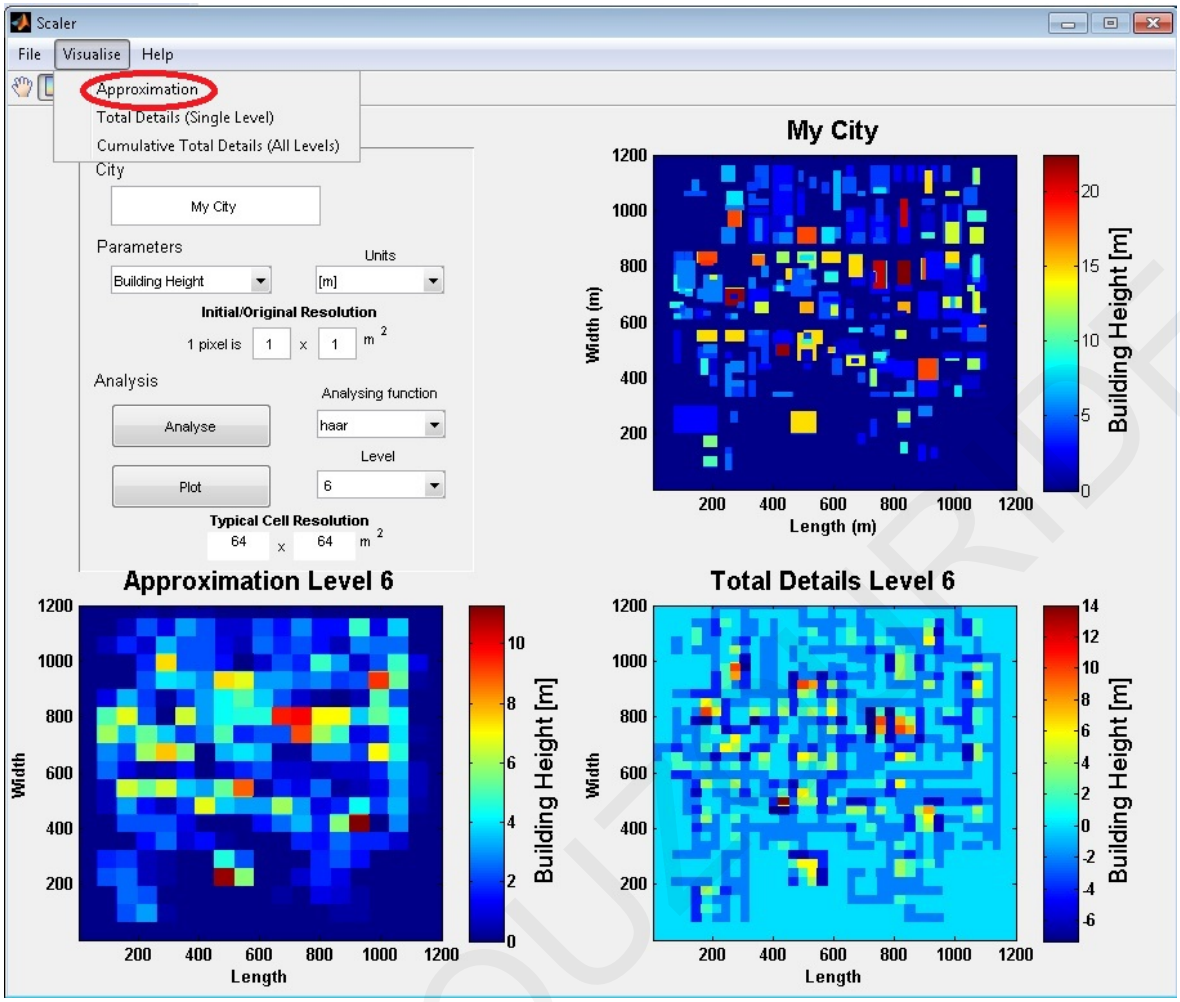

Figure B.7

Click File > Open and select ”Export Data”. *Scaler* automatically exports the numerical results of Approximations, Horizontal, Vertical, Diagonal, Total and Cumulative Total Details into a MATLAB array file (.m).